Interactions Between Sodium Carbonate Aerosols and Iodine Fission-Products

A DISSERTATION SUBMITTED TO THE UNIVERSITÉ DE LILLE BY

Ankita Jadon

IN ACCORDANCE WITH THE REQUIREMENTS OF THE DEGREE OF

DOCTOR OF PHILOSOPHY

DOCTORAL SCHOOL:

SCIENCES DE LA MATIÈRE, DU RAYONNEMENT ET DE L'ENVIRONNEMENT

FIELD:
OPTIQUE ET LASERS, PHYSICO-CHIMIE, ATMOSPHÈRE

DEFENDED ON JULY 20TH 2018 IN FRONT OF JURY MEMBERS:

Dr. Sophie Sobanska	Université de Bordeaux	Reviewer
Dr. Monica Calatayud	Université Pierre et Marie Curie, Paris	Reviewer
Pr. Gérard Cote	Ecole Nationale Supérieure de Chimie, Paris	External Examiner
Pr. Laurent Gasnot	Université de Lille	External Examiner
Pr. Denis Petitprez	Université de Lille	Director of Thesis
Dr. Sidi Souvi	IRSN-PSN-RES/SAG/LETR	Principle Advisor
Mr. Christian Latge	International Expert, CEA	Invited Member
Dr. Nathalie Girault	IRSN, Cadarache	Invited Member

Abstract

The safety assessment of sodium-cooled fast rector requires a risk-informed approach. The interactions between sodium combustion aerosols, post-fire, and radionuclides contribute significantly to the chemical as well as radiological source term. The work in this thesis concerns the investigations of the interactions between sodium carbonate aerosols and iodine based gaseous fission-products (I_2 and HI). A combined theoretical chemistry and experimental approach is adopted to have insights on both atomic and macroscopic level. An analytical ab-initio based expression of the adsorption isotherm has been developed. Ab-initio calculations using the Density Functional Theory (DFT) are performed to study the relative stabilities of the surfaces of sodium carbonate; iodine reactivity was then studied on the most stable surfaces and the adsorption isotherms were evaluated. Experimentally, iodine vapors were generated and their uptake efficiencies by sodium carbonate sorbent were investigated within various boundary conditions. Associated kinetics of the reaction was modelled using a pseudo first-order kinetics law.

The average I_2 uptake efficiency thus calculated from the experiments, 2-3 molecules per nm^{-2}, was found to be in a good agreement with the uptake efficiencies predicted by ab-initio DFT predictions, for one of the considered surfaces. The results imply that at the average gas temperatures expected in the containment in case of a SFR severe accident with primary sodium ejection outside the primary circuit, (i.e., between 373 and 423K), the most favorable carbonate surfaces will be predominantly bare or doubly occupied depending on the iodine partial pressure. Within the boundary conditions expected in the containment during a severe accident (i.e. with a high molar ratio of sodium carbonate aerosols), the study suggests that, at equilibrium, the residual partial pressure of iodine will be lower than 2×10^{-4} bar at 373 K.

Résumé

L'analyse de sûreté des réacteurs à neutrons rapides refroidis au sodium de Génération IV nécessite l'étude des conséquences d'un accident grave en cas de rejet dans l'environnement du sodium et des radionucléides qu'il transporte (terme source chimique et radiologique). Le terme source global dépend donc à la fois de la spéciation chimique des aérosols de sodium, issus de la combustion du sodium dans l'enceinte, et de leurs interactions avec les radionucléides. Au cours de cette thèse, les interactions entre le carbonate de sodium et les produits de fission gazeux iodés (I_2 et HI) ont été étudiées aux échelles atomique et macroscopique, via une double approche théorique et expérimentale. Une expression analytique de l'isotherme d'adsorption a été développée. La stabilité relative des surfaces du carbonate de sodium a été déterminée par des calculs ab initio utilisant la théorie de la densité fonctionnelle. La réactivité de l'iode a été étudiée pour les surfaces les plus stables et les isothermes d'adsorption évaluées.

En parallèle, la cinétique de capture de l'iode moléculaire par le carbonate de sodium a été déterminée expérimentalement pour différentes conditions. L'ensemble des résultats montrent une capture efficace de l'iode moléculaire par le carbonate de sodium à 373 K, variant selon la pression partielle d'iode et la surface du carbonate. Pour les conditions représentatives d'un accident grave, les sites d'adsorption de la surface de carbonate de sodium la plus favorable seront majoritairement vides ou doublement occupés selon la pression partielle d'iode moléculaire, conduisant à une pression d'équilibre inférieure à 2×10^{-4} bar à 373 K.

Acknowledgements

Undertaking this PhD has been a truly life-changing experience for me, and it would not have been possible without the support and guidance that I received from many people. My acknowledgments go to many beyond those listed here, but, especially to those listed here - for making the past three years of life and work, a time I have enjoyed, I am eternally grateful for, and, will fondly remember going forward.

I would like to start with my daily supervisors at the IRSN, Nathalie Girault and Sidi Souvi, who first gave me the opportunity for a master internship and then trusted me to continue the PhD work despite limited knowledge I had in theoretical chemistry. I have benefited greatly by having three supervisors who complemented each other academically and personally.

Nathalie, for helping me understand the bigger picture. Her depth of knowledge in fast reactors still amazes me. She continuously set an example of perseverance and of hard work. She taught me the importance of details, different ways to interpret data and embed them in a scientific story. She has also engraved into my mind the importance of using precise language. Something beautiful and exceptional about her, I have always felt a sense of being in her care.

Sidi, who guided my first steps in quantum chemistry and passed his knowledge in DFT and the valuable ideas about the multiscale approach followed in this work. I want to thank him for his critical point of view, especially, while teaching me that the whole of nature is always merely an approximation to the complete truth, or the complete truth so far as we know it. Therefore, things must be learned only to be unlearned again or, more likely, to be corrected. He knows how to motivate people without being a micromanager, and how to reassure when a paper gets rejected from three journals.

Denis, thank you for hosting me warmly in Lille. I owe a special thanks to him, for being a patient teacher, the director of thesis, and a mentor throughout my PhD. His ideas are all over this thesis, and it's so much the better for that. I will always value his perspective on challenges in science and academia. I would also like to thank him for his constant availability via emails or Skype. I always knew that I could count on an answer within 48 hours at the latest, regardless of his GPS location. Most of all, I am thankful that he gives his students space and freedom to find their direction as researchers.

I would like to thank Joëlle Fleurot, who gave me the opportunity to work on an exciting thesis subject, as well as Christian Mun for hosting me at L2EC and later in LETR.

I am grateful for the other members of my thesis committee for the discussions during the thesis defense and their suggestions to improve the quality of the manuscript.

I'd like to thank Anne-Cécile Grégoire for teaching me everything I know about experimental iodine chemistry and other lab tricks. She also did many of the foundational experiments which motivated my experimental research. Thank you very much! The research team at L2EC is a vibrant group of people, and it was a real privilege to work

with such friendly colleagues. Any problem you might have, from instrumentation to installation to writing, there is someone who can guide you.
I'd like to acknowledge and thank my colleagues from the LETR. Katia, for being my first officemate. Thanks for walking me through administration and making me feel home! Thank you, Bruno, Caroline, Leatitia, Karine, Bénédicte, Loïc, Luke, Tim, Marc, François, Fred, the two Roro, Cathy. As well as the members of the SAG, Marie-Claire, Isabelle, Patrick, and Lionel for having welcomed me with remarkable kindness and attention, sharing pleasant moments around meals and coffee breaks.
These three years of the thesis were also an opportunity for me to make many friends. Thank you so much JAZ for organizing and motivating 'others' for hiking; Miloud for your humor; Nacho, your unconventional jokes (and endless questions) will be missed; Alex, I am sure you're eating vegetables while hiking in a parallel universe; Shambhavi, for motivating me not to do Zumba and a post-doc; Ali, for unknowingly teaching me the philosophies of stoicism which helped me to stay calm under pressure; and my two in-house counsellors: dr. Spaghetti and Ashkan for their immense support especially during the last leg of my PhD journey. Mathilde, Miriam, Mirco, and Kasi, I wish you all the best for your future.
I was lucky to be able to share the office with my friends and partners in crime: Faoulat, Laura, and Anh. Faoulat, thank you for your moral support but also for your sense of humor; you've become a close friend over the years. Anh, I don't even remember how we started getting along; probably first by laughing together at something utterly random and retard in the corridors. You've lent a shoulder for me to cry on, but also made sure that we could crack up about anything ranging from science to 'so dumb'. Laura, on a professional note, thank you for your helpful inputs on writing and presentations. I wish the best for you!
During my second year, I was lucky enough to spend a year as a visiting student at PC2A in Lille. I am also thankful to the colleagues of PC2A: Lucia, Jinane, and Lila for the enriching experiences, especially, the morning coffee at Lilliad and long walks in the university campus which took me through the struggles with experiments, so thanks! I would like to thank Nicolas, who gave me various opportunities to revise my perspective on life and on science. Beatrice, Sylvie, Olivier, thank you for standing by my side in the course of my experimental work. Thank you, Tanu, Dev, and Dorel for being my google of surface characterization.
Apart from my lab-mates, so many other people made this PhD journey a real treat. Thank you, Rong and Ingvild for being the best room-mates and the right daily ratio of laughing and relaxing at home. Thanks Rong, my first contact in Aix, for all our late night WeChat video calls, no matter in which part of the world we are. Ingvild, thank you for the movie nights and your thoughtfully crafted letters for every important occasion. I hope to see you very soon in Norway!

My master studies advisors Prof. N.K. Joshi and Vikram Rathore have remained outstanding mentors, always offering helpful guidance on my career.
An exceptional thanks goes to my friends in India, Nivedita and Meghna, for years and years of unwavering support. The completion of this thesis would have been a long and windy road if not for their continuous encouragement. Thank you for *everything*!
Finally, I'd like to express love and gratitude to my parents, mummy and papa, for having faith in me. I couldn't have gotten to this point without their constant reassurance and helpful advice throughout my PhD.

Contents

List of Figures

List of Tables

Chapter 1 Introduction

1.1 General introduction

The Generation IV International Forum (GIF) initiative, launched in the year 2000, selected six different technological concepts for Generation-IV nuclear reactors. Amongst the chosen concepts, the sodium-cooled fast reactor (SFR) was chosen by France as one of the most promising nuclear system for the future (
Figure 1-1). One of the significant advantages of SFR over other Generation-IV reactors is the extensive operation and research experience of about fifty years that can benefit to a great extent. In France for instance, several research, prototype, and demonstration and industrial SFR units have been built and operated since the 1960s (Rapsodie, 40 MWth; Phenix, 250 MWe; Superphenix 1200 MWe). Nonetheless, nowadays new criteria have to be taken in the development of Gen IV reactors in order to comply with safety, sustainability, reliability, proliferation-resistance, and economic profitability. Especially, the safety objectives for Gen-IV reactors should take into account the improved safety objectives of the so-called Generation III reactor technology (EPR) as compared to the past Gen-II reactors. In addition to this, the harmonized safety objectives defined in 2010 by Western Europe Nuclear Regulator's Association (WENRA)[1] for the new nuclear systems shall also be considered. Furthermore, lessons learnt from the Fukushima-Daiichi nuclear power plant accident in 2011 shall be implemented [2].
The Gen IV reactors, notably, the SFRs are under development in various countries, in particular, China, India, and Russia. In France, the Advanced Sodium Technological Reactor for Industrial Demonstration (ASTRID) project[1] was launched in 2010. ASTRID is intended to be a precursor for a future potential development of SFR technology in France.

[1] A consortium gathering Research Institutes and French industries, CEA, EDF, and AREVA with a high involvement of Japanese companies (JAEA, MNI).

Introduction

As shown in Figure 1-1, at an international level, the GIF has selected six concepts for the future generation of nuclear reactors in 2001. At European level, the selection included mainly fast nuclear reactors, namely the sodium-cooled fast reactor (SFR), the gas-cooled fast reactor (GFR), the lead-cooled fast reactor and the very high thermal power reactor (VHTR). This selection was made by the European Sustainable Nuclear Industrial Initiative (ESNII) in 2009. At national level (France), finally, SFR and GFR were shortlisted. It was chosen in agreement with the general objectives outlined in the national energetic strategy for fuel cycle closure, which requires more efficient use of the uranium resources and reduction of long-lived wastes [3]. In France, a research program was then initiated since 2010 in support of research and development of the ASTRID prototype which is based on the very general principles for SFR concepts and designs, but, at the same time, meets the criteria of innovation and improved safety [4],[5].
As a part of the safety analysis due for the commissioning of the ASTRID prototype, safety provisions for the prevention and mitigation of severe accidents (SA) were implemented at the reactor design stage itself that should decrease the probability of a severe accident occurrence and reduce its consequences. Nevertheless, as the probability of occurrence of a SA could not be eliminated entirely, the risk and associated high chemical and radiological consequences of a contaminated sodium-fire taking place in the reactor containment following the primary sodium ejection through the reactor cover still has to be investigated.
The consequences and associated risks of a postulated sodium-fire in a SFR containment are of two kinds:

- Thermodynamic consequences, such as increase in temperature and pressure; in this case, the integrity of the containment structures can be compromised.

- Production and chemical evolution of generated contaminated sodium-aerosols; in this case some of the aerosols are likely to be released outside the containment building and dispersed in the reactor surrounding ecosystem.

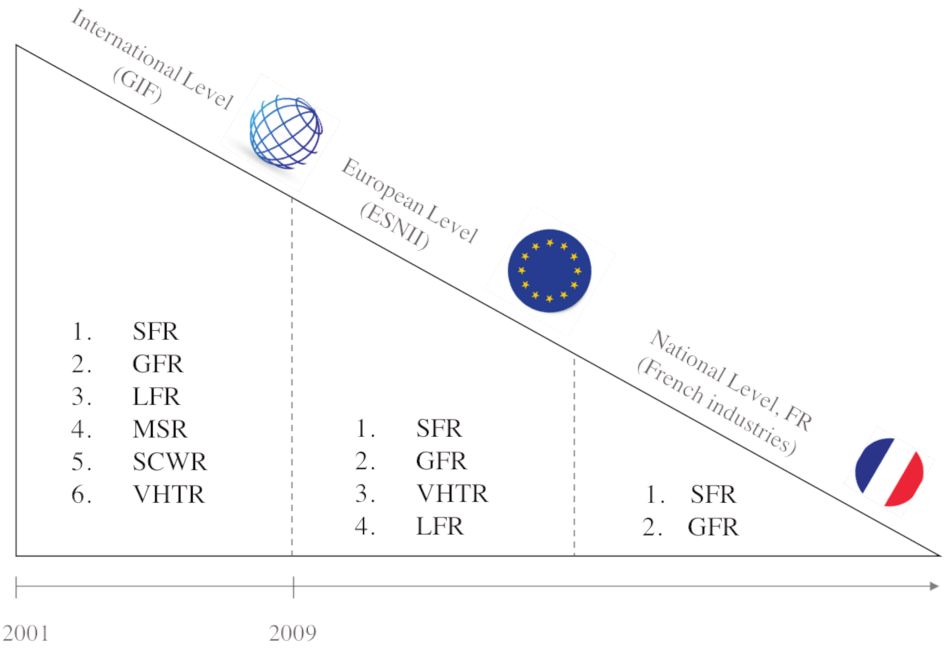

Figure 1-1 Selection of Generation IV reactor designs by various organizations. *GIF* Generation IV Forum; *ESNII* European Sustainable Nuclear Industrial Initiative; *SFR* Sodium-cooled Fast Reactor; *GFR* Gas-Cooled Rector; *LFR* Lead-Cooled Fast Reactor; *MSR* Molten Salt Reactor; *SCWR* Super-Critical Water Reactor; *VHTR* Very High-Temperature Rector.

The knowledge of the physico-chemical composition and behaviour of the generated sodium-based aerosols, potentially acting as a vector for fission-products (FP) transport, is of prime importance for the evaluation of the toxicological and radiological impact of the accidental releases into the environment. For instance, the efficient adsorption of volatile FP (such as iodine) onto these aerosols could contribute in drastically reducing their radiological impact in case of a SA.
Aerosols formed during the accidental release of primary sodium, Na (l), coolant into the containment and its combustion, firstly consist of oxides of sodium (Na_2O, Na_2O_2 and NaO_2), which are particularly toxic and corrosive. These species can in turn interact with water vapour (H_2O) to form a comparatively less corrosive aerosol of sodium hydroxide (NaOH), which can further hydrate and form fine droplets due to its very hygroscopic nature. Furthermore, these NaOH species can react with atmospheric carbon di-oxide (CO_2) to form sodium carbonates (Na_2CO_3). Finally, the reaction with CO_2 and H_2O to form sodium bicarbonate ($NaHCO_3$) would leave these aerosols stable[2] and harmless.

[2] Stable at temperatures below 150°C.

Introduction

The studies on the chemical evolution of sodium aerosols have been previously reported in the literature [6], [7]. However, as far as we know, interactions between sodium aerosols and FPs have never been investigated yet. Indeed, most of the past safety studies considered that FPs released from the degraded fuel during a SA would be efficiently trapped in the primary coolant because of their high chemical affinity for Na (l). Furthermore, in most of the Core Disruptive Accident (CDA) studies, it was also assumed that the concentration of fission products in the Na (l) ejected into the containment, corresponding to the top of primary hot pool was low. Recently, new explorations on SFR safety indicate that, even if the current level of reliable information with respect to FP behaviour in a SFR coolant circuit is relatively satisfactory, many key phenomena would require more research for a reliable estimation of the source term [8], [9], [10]. Especially, regarding the source term, the behaviour of key radionuclides (RN) such as iodine in the containment has to be understood well [8]. Indeed, far less has been done on the release and partitioning of iodine during sodium combustion and chemical reactions of iodine vapours with sodium combustion aerosols [8]–[10]. The latter phenomenon is the motivation of this research.

1.2 Motivation

As previously mentioned, the safety objectives for the Gen-IV SFR reactors to be built in the future in Europe will have to be considerably upgraded as compared to the past generation of SFRs built in the 1980-90s. Particularly, in addition to the radiological safety objectives laid out for the Gen-III, EPR reactors, the SFRs will have to ensure the safety criteria, which are:

- No protection action for the population should be taken under accidental scenarios, except in case of a SA;
- In case of a generalized core melt-down scenario, the actions to be taken have to be limited in space and time.

Furthermore, SFRs shall comply with the set of recommendations issued by WENRA where one of the primary objectives is to develop an harmonized approach to nuclear safety and radiation protection issues along with their regulation [1]. Compared to the current operating nuclear power plants, WENRA expects new nuclear power plants to be designed, sited, constructed, commissioned, and operated with the objectives of:

- Improved confinement features that should be designed as far as possible to cope with core melt accidents, even in the long term;
- An extended safety demonstration for new plants, in consistency with the reinforcement of the defence in depth concept. It implies that some situations that are considered as "beyond-design" for existing plants, such as multiple failures conditions and core melt accidents, shall be considered in the design of new plants.

Feedbacks from the Fukushima-Daiichi event, beyond-design accident where the earthquake and tsunami virtually disabled all back-up and safety systems of the nuclear power plant must be also taken into account in the design of new plants. This shall result in a better account of external stresses on the robustness of the main reactor components important for safety resulting in an improved long-term management of the loss of support functions and an increased grace time for SA management. Finally, in addition to the aforementioned improved safety measures, the specificity of SFRs which relies on the use of Na (l) as a primary coolant, has also to be addressed. Especially, as already mentioned, the risk of producing toxic and contaminated sodium combustion aerosol in the containment that would be further released into the environment and the evaluation of their associated consequences would have to be taken into account.

1.2.1 Severe accidents and associated chemical risks

Liquid sodium coolant was a natural choice for fast reactors owing to its intrinsic capabilities of low neutron moderation and absorption. Sodium is stable when exposed to neutron flux. However, it produces two radioactive isotopes, Na^{22} and Na^{24} which have half-lives of 2.6 years and 15 hours, respectively.

$$Na_{11}^{23} + n_0^1 \rightarrow Na_{11}^{24} + e^- + \overline{v}_e$$

$$Na_{11}^{23} \rightarrow Na_{11}^{22} + e^+ + v_e$$

The concentration of Na^{24} produced during the operation is much lower compared to Na^{22}, making the environment in the primary circuit suitable to work after a few days, post-shutdown. However, there is an inherent risk of using liquid metal sodium as a coolant in SFR. Like all alkali metals, sodium has indeed a very high affinity for oxygen and water that leads to highly exothermic chemical reactions. For source term studies, the primary reaction occurring in case of a CDA is the sodium-air interactions where the liquid sodium ignites and burns spontaneously even in contact with low oxygen concentrations ($O_2 \geq 5\%$ v/v). The oxidation of sodium is intensive

and releases much energy in the form of heat and light. The sodium combustion also produces a significant amount of sodium aerosols that can, in turn, prevent the human intervention in the plant, because of their toxicity and visibility reducing effect. Some of them being corrosive they can also damage electric, electronic components and can lead to the loss of safety functions. Depending on the degree of oxidation of sodium, its combustion also leads to a rapid increase in pressure and temperature in the containment and surrounding areas. Therefore, the design of the reactor must prevent as much as possible the risk of sodium leaks as well as also facilitate their early detection.

1.2.2 Background on sodium-cooled fast reactor source terms

As explained in the previous section, difficulty in handling Na(l) and its associated risks have received much attention in the past. Indeed, there have been a variety of studies of sodium spray fires, sodium pool fires, sodium interactions with concrete and molten fuel. The interactions between molten fuel and liquid sodium, potentially associated with a significant releases of mechanical energy, and crucial for the primary vessel dimensioning were especially investigated within the frame of safety analyses. Also past experimental investigations of combustion aerosol physics in reactor containments were instrumental in the development of highly sophisticated aerosol behaviour models that were implemented in computer codes such as MAEROS [11] and CONTAIN-LMR [12].

Meanwhile, the issues of RN behaviour (releases from the fuel, transport within Na (l), vaporization from Na (l) in the case of sodium fires) during SA sequences as well as physicochemical behaviour of Na combustion aerosols were often less studied.
Thus, previous and more recent experimental and modelling work available in the literature mainly addresses the following issues:

- A few experimental results and upgraded models were recently reported [6], [7], [13], [14] in the literature on the physio-chemical behavior of Na-aerosols in the reactor containment building.
- The release of radionuclides from hot, boiling and, to a less extent, burning Na pool[15], [16], [17].

The few experimental investigations of RN retention in sodium coolant were reasonably integral in nature and exploratory in intent [18]. These investigations did show some retention of RN in liquid sodium depending on the experimental conditions, RN volatility and their chemical affinity with sodium coolant. However, they also showed, in specific conditions, there would be significant releases from

sodium pools, especially for the more volatile RN such as isotopes of cesium, and tellurium. The case of iodine which exhibits a higher affinity with sodium coolant in specific conditions as compared to others volatiles deserve more attention and will be detailed later on.
A few empirical correlations were developed in the past to model RN release from hot or evaporating sodium pools; recently for burning sodium pools [19]–[22]. For a proper source term evaluation, however, all in-vessel and in-containment phenomena shall be considered along with the different possible routes during the progress of SA.
Analytical work investigating the gaps in knowledge for source term studies have been performed recently indicating that this area now receives a little more attention in Europe and overseas. It greatly helped to identify where the modelling effort shall to be focused [8], [23]. This work explores one of these gaps and attempts to provide better insights on the chemical and radiological source-term for SFR. The outcomes of this work should profit the in-containment phenomena modelling in the integral code ASTEC-Na which is currently under development at IRSN for SFR safety analyses [24]. This new integral calculation tool is intended, at medium term, to evaluate the consequences and predict the source term of unprotected accidents.

1.3 The layout of the thesis

In this thesis, the heterogeneous interactions between Na_2CO_3 (s) and iodine-based gaseous FPs (I_2, HI), as well as with H2O (i.e. bicarbonate formation) is studied. The extent of the adsorption/desorption of gas phase FP species on the surface of Na_2CO_3 aerosols highly depends on the SA sequence. Otherwise speaking, both the chemical forms of FP and their concentrations will be scenario-dependant. The different potential SA scenarios and their associated sequences of events are described in detail in Chapter 2 where a review of past source term analysis is also given. Then the theoretical and experimental work performed during this thesis is presented.
This thesis is thus divided into four major parts:

1) Introduction - background and state of the art
2) Methodology - theoretical and experimental
3) Results - theoretical chemistry predictions and experimental measurements
4) Summary and conclusions

Introduction

A brief description of the outline of the thesis is given below:

- The first part of the thesis includes the explanation of SA phenomenology including FP release and in-containment generation and speciation evolution of sodium aerosols. A brief review of the aerosol generation models developed in the literature is also discussed. Furthermore, the in-containment iodine behaviour is presented. Finally, after having identified the gaps in knowledge, the problem statements have been defined and the methodology to address them is laid out.

- The second part discusses the methodology used in this work. A combined, multi-scale theoretical and experimental approach was adopted to have insights both on an atomic level and macroscopic level. Chapter 3 is devoted to describing the theoretical chemistry tools and theories used to solve the problem. Chapter 4 deals with the experimental approach and measurement techniques.

- The results and discussions from both approaches are presented in Chapter 5 and Chapter 6. Chapter 5 discusses the results obtained using theoretical chemistry approach. A generic methodology to relate surface coverage as a function of partial pressure of a gas and temperature is developed and applied on the system under study. The calculations at a given temperature give the equilibrium residual partial pressure of iodine based gas-phase species. This way of calculation is compatible with experimental measurements. Chapter 6 presents the experimental results obtained on the kinetics study of the reaction between Na_2CO_3 and molecular iodine. The simplified kinetic model built to analyse the results is also reported.

- Finally, in section four, the results from both approaches are summarised and compared. Their limitations and strengths are reported. An integrated methodology is then presented which can be used to study the interactions between other aerosols and FP.

Chapter 2 State of the art in severe accident studies in SFR

Considerable research related to SA and source term studies were carried out in the 1980-90s when designing and commissioning the French Superphénix reactor. The aim of this chapter is no to go into details about all the French SFR programs and the researches performed at that time but rather to highlight and discuss the technicalities of short-comings, the remaining research needs, and the main challenges for the future SFRs regarding safety studies and source term evaluation. First, several cases of SA phenomenology in SFR are discussed in Section 2.2; a measure to study the consequences of a SA is then outlined. The requirements and strategies to have a better description of the realistic source term are then presented in Section 2.5. Main phenomena leading to sodium carbonates generation and molecular iodine releases inside the containment as well as past associated R&D studies and modelling work are respectively reported in Section 2.4 and 2.5. Finally, the gaps in knowledge, R&D requirements, and the objectives of the thesis are presented in Section 2.6.

2.1 Background

Fast reactors (FR) were developed before light water reactors (LWR) mainly because of the breeding capabilities that make them attractive from a sustainability point of view. The safety of FR was always a central issue, and they were even initially the driver for LWR safety.

A considerable attention was primarily given to SA, because those reactors were not initially in their more reactive configuration. Indeed, core material rearrangement can lead to fast positive reactivity additions and to a significant mechanical energy release. That is why the Core Disruptive Accident (CDA) has permanently haunted the FR development. Amongst FR, the safety of SFR and accident evaluations started early in the 1950-60s where the greatest concerns focused on the potential of the reactor core to re-compact after a CDA and on the associated consequences (explained in the coming sections). At that time however, CDA analyses were associated with major

uncertainties and questions about their role and importance (i.e., their occurrence probability). It includes whether or not the CDA should be considered as a Design Basis Accident (DBA) or Beyond Design Basis Accident (BDBA). In the 1980s, where considerable improvements in scram[3] and decay heat removal systems have been performed, CDAs were considered as BDBAs but for which substantial mitigation of consequences must be verified. The efficiency of specific mitigating measures implemented by the design engineers at that time was justified by ensuring that these measures were based on an adequate understanding of CDAs as well as on their consequences.

The implemented mitigating provisions sometimes encompassed the impact on reactor building cost and the normal reactor operations and maintenance. This was especially the case in Superphénix where a "dome" structure, acting as an intermediate barrier between the primary vessel and the containment building, was implemented. More elaborate and modern concepts are now developed where safety provisions for CDA prevention and their consequence mitigation are taken Into account in the reactor design [5].

However, despite all the vast amount of work done on SA phenomena, compared to PWR safety studies, source term in SFR did not yet reach a similar level of analyses yet.

2.2 Severe accident phenomenology and source term in SFRs

Different sequences of events leading to various consequences (i.e., source term) can occur in SFR. Whatever the initiating event is, two main accident routes are generally considered:

- An energetic disassembly path leading to reactor-cover damaging and ejection of sodium in the containment[4]. This route is often characterized by an energetic re-criticality event with dynamic molten fuel sloshing motions.
- A timely fuel discharge and melt-down (less energetic route) leading to a gradual fuel heating/damaging and FP release in the liquid sodium.

A detailed sequence of events and possible pathways leading to a SA in SFR is shown in Figure 2-1.

[3] Emergency shut-down of a nuclear reactor.

[4] Consequences of energetic events are primarily considered in this work.

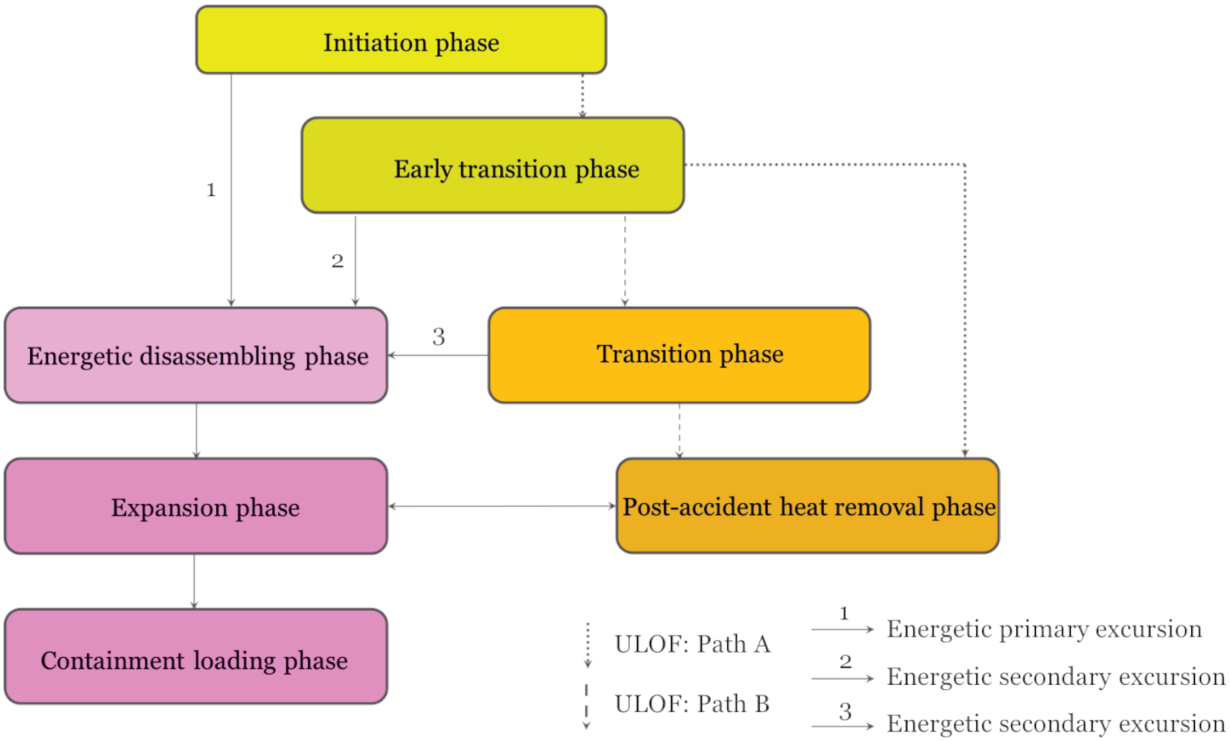

Figure 2-1 Main accident phases and scenario routes considered in a Unprotected Loss of Flow accident [25].

During SA, various gases and vapors (noble, halogen, and volatile FP) can escape the overheated fuel assemblies and be in the fuel pin gas plenum where they contribute to the pin over-pressurization. After their release form the fuel pin their becoming mainly depends on their physicochemical properties and on the boundaries conditions within the primary vessel. Thus, after their releases, these FPs can be:

- Dissolved or bonded with Na (l) in the coolant pool.
- Deposited on primary vessel surfaces.
- Released/vaporized into the cover gas region above the coolant pool.

Considering the two main scenario routes displayed in Figure 2-1, the transfer of FPs from the fuel assemblies to the containment region can then occur either through a 1) bubble or 2) liquid pathways, respectively for the energetic and non-energetic path as shown in Figure 2-2.

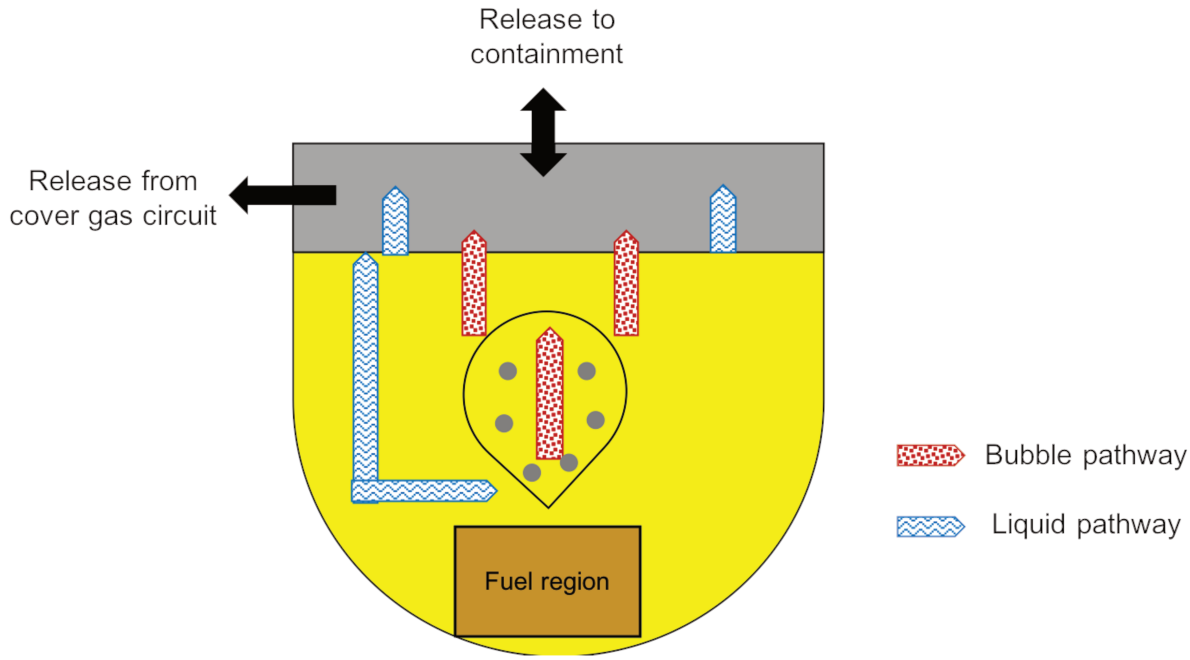

Figure 2-2 Schematic diagram to show mitigation of volatile FP to the cover gas region through the bubble and liquid pathways. *Aerosol transport*: the bubble pathway. *Evaporation*: the liquid pathway.

Due to the subject of this thesis, considering phenomena occurring in the containment only energetic events are of interest. During such events, with sodium boiling phases, the FP transfer to the liquid sodium by bubble-scrubbing is increased which promotes the subsequent evaporation of dissolved species and their release into the containment in case of primary sodium ejection out of the primary vessel. Out of all the scenarios listed above, in this work, it has been assumed that the first and the second barrier (Figure 2-3) have failed so that the volatile FP can escape into the containment. To give the reader an overview about the SA phenomenology, the two following sub section will respectively describe the 1) in-vessel 2) in-containment[5] main phenomena.

2.2.1 In-vessel

Several kinds of transients and accidents (protected or unprotected[6]) potentially leading to a core melt-down are generally considered for safety analyses depending on their initiating events (i.e., loss of flow (LOF), reactivity insertion (TOP), loss of heat sink (LOHS), and external events). Most of them are global transients affecting the whole core either on a short (LOF, TOP) or long time-scale (LOHS). Local initiating events (i.e., Total Instantaneous Blockage, TIB, of a sub-assembly) were also

[5] Alternatively called as ex-vessel.

[6] Unprotected transients are determined by a failure of shutdown systems.

considered as their early detection might not be rapid enough for the prevention of escalation into a complete core accident.

The main SA scenario usually considered in safety analyses is the ULOF accident as it represents the enveloping case for the consequence of postulated SA in SFR and covers the most important accident phenomena [25]. The accident starts with a generalized LOF (either initiated by primary pump coast down or breaking of a primary coolant pipe) without activation of the reactor shutdown systems (ULOF accident). The time for core undercooling and for sodium boiling will depend on the coolant flow decrease rate that plays an important role in further progression of the accident. However, as the reduction on power generation generally develops much slower than the decrease in coolant flow, the power-to-flow ratio mismatch results in a rapid single phase coolant heat-up which may quickly lead to coolant boiling, pin clad dry-out, clad melting and relocation, and subsequent fuel pin break-up followed by core material relocation. Moreover, the increase in coolant temperature induces associated reactivity feedbacks which considerably determine the course of the ULOF transient. The coolant temperature increase induces positive reactivity potentials due to sodium positive void worth that in turn, depending on the core configuration and design, may potentially lead to a high reactivity insertion in the reactor core and core disruption.

Depending on the sodium void effects in the central core regions, a more progressive fuel discharge and melting can also occur after a LOF event. This leads to the formation of medium scale and later large scale molten pools and eventually relocation phenomena where the FP can be transported to the cover gas by progressive vaporization from the hot/boiling sodium.

In the most penalizing cases, all these phenomena can potentially generate a secondary power excursion (re-criticality events). The outcomes of re-criticality events and of the following expansion phase initiated by fuel and/or sodium vapor bubbles are generally dramatic due to significant mechanical energy release to the reactor vessel structures.

Whatever the SA initiating event is, FP will be released from the large-scale overheated and failed fuel pins altering the coolant activity. After fuel clad failure indeed, Releases of FP vapors and eventually molten fuel ejection in the liquid sodium can occur where further fuel-coolant interaction, fuel relocation (freezing slumping) and eventual fuel debris bed formation will impact on further FP releases inside Na (l). In SA then, the coolant activity will continuously change against time and with core disruption which, in turn, strongly depends on the fuel and local coolant conditions[7]. This complex and case-dependent phenomenon increases the complications in prediction of a realistic, mechanistic source term. Furthermore, the

[7] Core inventory, FP chemical and physical properties.

two-phase sodium conditions during the CDA dramatically obscures the localized aerosol physics where the primary system phases and the flow conditions both impact the removal and re-suspension of these aerosols throughout the transient.

The reactor coolant activity will be the product of FP, fuel releases and their subsequent relocation throughout the reactor coolant system. This occurs in addition to sodium coolant activation during reactor operation. During the early phase of a SA and fuel melt progression, most of the noble fission gases will be released from the fuel. A significant fraction of the volatiles (Cs, I, and Te) and some part of semi or low volatiles (i.e., Ru, Mo, and so forth) will also be released. This release will depend on the dissolution and vaporization of the corresponding FP chemical species within the fuel matrix (see Figure 2-3).

Fuel and clad chemical interactions as well as coolant physical and chemical interactions that can produce additional FP chemical forms (i.e., iodine reacting with liquid sodium forming sodium iodide) can further play a vital role on their behavior. Once released, the behavior of FP in the primary vessel will depend on others factors, such as, their initial physio-chemical forms affinity with the coolant (volatility, solubility in sodium) and the accidental scenario (i.e., sodium voiding, energetic fuel-coolant interactions, and so forth).

The potential failure of the reactor vessel following a CDA would allow the release of a fraction of the coolant and its inventory inside the containment. Ex-vessel releases only consider the vessel upper part failure because of the guard vessel preventing any other ex-vessel releases in case of the vessel heating and melt-through. The upper head breach following mechanical energy deposition during a CDA (i.e., from over-pressurization due to fuel-coolant interactions, positive void coefficient effects or re-criticality of the debris bed) lead, as already mentioned, to a release of sodium in the containment and its subsequent burning.

Table 2-1 Principal characteristic states of FP and their location in liquid sodium [27].

Element	**Characteristics in Na (l)**	**State**	**Main location(s)**
Noble gases Xe, Kr	Inert, almost zero solubility	Elemental state	Gas phase
Halogens I, Br	Highly volatile but react with Na → low volatility	NaI, NaBr	Primarily in Na(l) Some in gas phase
Alkali metals Cs, Rb	Soluble, high volatility	Cs, Rb	Some in Na(l) Primarily in gas phase
Alkali earth metals Sr, Ba	Low volatility either as metals or oxides	SrO, BaO in suspension; Sr, Ba soluble in Na(l)	In Na(l)
Noble metals Ru, Pd, Rh, Ag	Very low solubility (except Ag), very low volatility	Metallic in suspension	In Na(l)
Other metals Mo, Tc	Very low volatility	Metallic and/or oxide in suspension	In Na(l)
Actinides U, Pu	Very low volatility	$M(O_2)$ in suspension	In Na(l)
Others Te	React with Na, producing telluride of low volatility	Na_2Te (s) in suspension	In Na(l)

2.2.2 In-containment

Failure of the reactor vessel slab allows ex-vessel release of a fraction of liquid sodium and its associated inventory. The ejected primary sodium will be spontaneously oxidized and burn by interacting with the present, gaseous, O_2, H_20, and CO_2. Being exothermic, the chemical reactions will generate heat and over-pressurize the

containment (see Section 2.4). Moreover, sodium aerosols will be produced that could serve as a transport vector for FPs. As the different chemical aerosol species produced during the sodium combustion (oxides, peroxides, hydroxides, carbonates, and bi-carbonates) are more or less toxic and corrosive, the chemical source term will depend on the physico-chemical behavior of these aerosols.

With a large mass of sodium ejected into the containment, the sodium-aerosol concentration will be high, leading to particle agglomeration and sedimentation. A significant fraction of the generated aerosols then settle on the containment floor, in the sodium pool and/or deposit on the containment walls. Nevertheless, a fraction of the suspended aerosols could be released through into the environment in case of an early containment leak tightness loss.

The radiological source term will depend on the FPs transportation and behavior inside the containment. Of primary concern, at the short term, is the behavior of iodine because of the radiological impact of its short-lived isotopes (i.e. I-131). As known previously, the behavior of FPs transported by the released liquid sodium is not yet well known. In particular, the repartition of the released inventory, between liquid, aerosol, and vapor or gas phases is poorly studied in the literature. One of the strongest concerns is the chemical evolution of iodine. Indeed, it is likely that NaI initially dissolved in the liquid sodium would be thermally decomposed during the sodium combustion producing volatile iodine species (i.e. I_2 - see Section 2.5). The subsequent evolution of these species (interactions with sodium aerosols, deposition on containment surfaces and/or on organic materials) could then greatly impact the radiological source term.

Apart from the FPs released through the primary sodium ejection, the transportation of FPs to the cover gas, when relevant for the considered reactor design, have also to be taken into account for accidents involving release of the cover gas inventory inside the containment.

To quantify and characterize the containment source term, it is then required to have a better understanding of the following phenomenon:

- The physico-chemical behavior of sodium aerosols.
- The repartition of FPs between the liquid, aerosol and vapor/gas phases.
- The interaction of the FP vapors with the aerosols where the most important identified research needs concerns the study of the interactions between volatile iodine and the sodium combustion aerosols [8].

The next two sections will focus on a) the combustion of sodium and the physio-chemical behavior of its combustion products and b) the iodine FP transportation and its chemical evolution inside the containment.

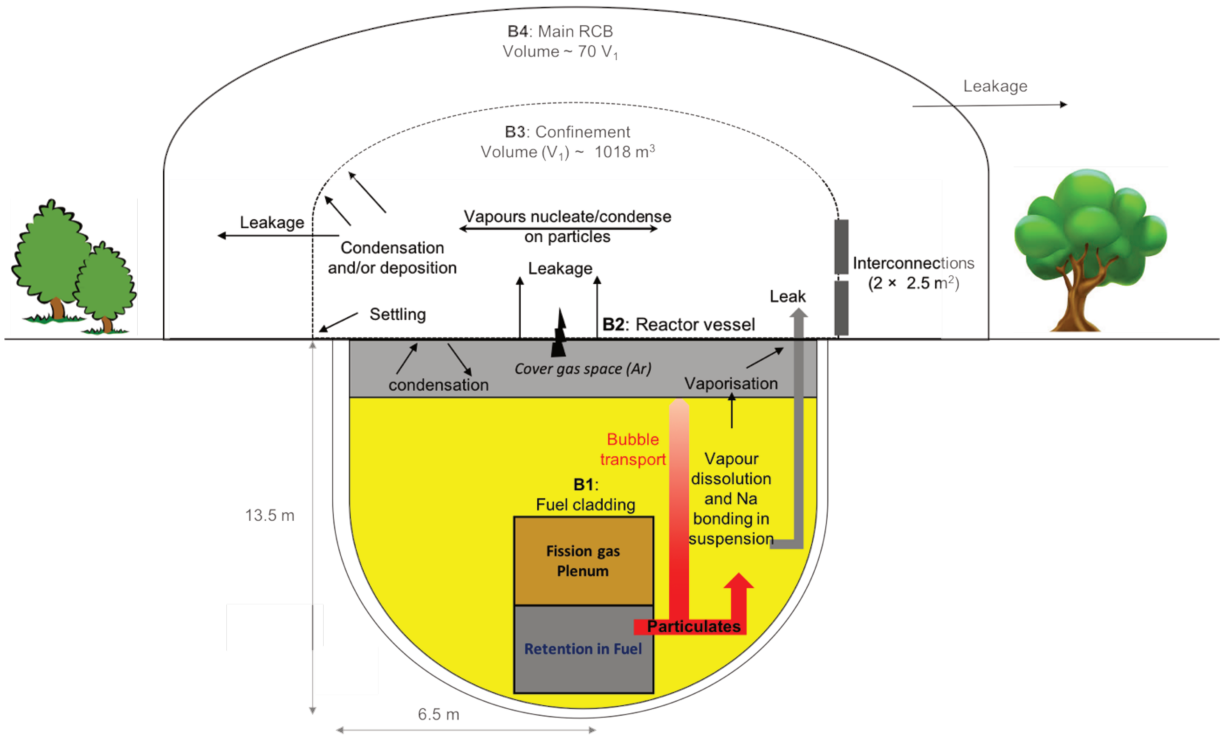

Figure 2-3 Schematic diagram (not to scale) showing main physical barriers B(1→4): fuel cladding, reactor vault, confinement, and the reactor containment building) together with the main phenomena governing the FP behavior [28], [29].

2.3 SFR source term determination

To have a complete description of the consequences of an SA for the determination of a realistic source term, one shall include the following:

1. Primary sources of radioactive releases
2. FP transport considerations
3. Principal characteristics and states of FPs in liquid sodium coolant
4. Selection of the most relevant core degradation conditions i.e.,:
    a. Fuel pin limited damage accidents involving releases of a small fraction of the volatiles (i.e., noble gases),
    b. Severe core damage accidents involving significant fuel damage without reactor vessel failure or core-concrete interactions,
    c. Complete core melt events with core-concrete interactions (in case of rupture of the principal and safety vessels and inefficiency of the core catcher).
5. Strategy for best-estimate and conservative calculations i.e.:

a. Use of existing experimental data,
b. Evaluation of associated uncertainties for each phase of the modelling process,
c. Flexibility in source term parameters to encapsulate design-specific features including safety features (i.e., filters, aerosol deposition and so forth).

In the past, there have been specific safety studies on radio-contaminant transfer in the primary circuit, but unfortunately, there exist no associated analytical methodology (models/codes) due to the complex phenomenology of the events, i.e., extremely high temperatures, pressures, and rapid kinetics processes. In addition only very few experimental results are available. Most of these studies were performed within the framework of Superphenix safety analyses where two different paths for radioactive releases were considered:

- Radioactive sodium (Na^{22}, Na^{24}) and FPs releases through penetrations in the reactor slab in case of a high mechanical energy release resulting from a fuel-coolant interaction or from re-criticality events;
- Gaseous and aerosol FPs releases from the cover gas circuit after the opening of the safety valves which protect the main vessel against over-pressurization as a result of building concentration of FPs and over-heating. This phenomenon is the only way of FP releases in case of a non-energetic accident.

The calculations performed for Superphénix in the early 1980's for both energetic and non-energetic SAs. It highlighted that the energetic severe accidents may induce more FPs retention in relation with the important mixing of the core components. Quite unexpectedly then, it came out that for source term the non-energetic path could be as detrimental as the energetic path.
More recent analyses (in the mid-1990s with SIMMER-CONTAIN code) were performed for the EFR project, taking into account simplified assumptions for the FP distribution in cover gas/containment region. The contamination of cover gas was deduced from an estimation of FP minimum retention, during the bubble expansion phase. For in-containment release an arbitrary factor (0.85) was taken into account.
To conclude this section, it is important to emphasize that the assumptions made for FP transportation distribution in the past are questionable and conflicting hence not acceptable for the determination of source term for future SFRs.
That is why the future model development for source term determination will have to be more analytical in order to reduce as far as possible the uncertainties. It is the strategy chosen by IRSN which is developing a new integral code (named ASTEC-Na) for safety analyses of the future SFRs from the current LWR European code

system ASTEC. The new code compatible for SFRs is characterized by a robust and modern architecture as well as a high flexibility to integrate new physical models (i.e., for future advanced designs). It capitalizes the state-of-the-art knowledge of SFR accidents. The development and validation of ASTEC-Na are currently underway [30]. The model developed for simulation of the primary phase of accidental scenarios has/will have to take into account fundamental phenomena affecting the in-containment source term.
It is expected that, at midterm, ASTEC-Na should be able to evaluate the consequences of unprotected accidents on material relocation and primary system loads as well as to determine the source term produced by the migration of activated FPs and likelihood to be released to the environment.

2.4 The combustion of sodium

This section will explore the combustion of liquid sodium, sodium combustion aerosol generation, and aging. Only main outcomes of past R&D work on sodium fires will be recalled in this section, as they are not the focus of this thesis.
A substantial amount of research has been done in the past on sodium combustion. The combustion of sodium is generally initiated from the Na vapors.

In case of a CDA, three kinds of sodium fires can occur in the containment vessel mainly depending on the size of the breach in the primary circuit, i.e., in the reactor top slab for pool-type reactors (interested readers can find more information about the experiments performed to study sodium-fires, in literature [26], [31]):

1. Pool fires[8]: The primary factor that determines the ignition of a sodium pool is the sodium temperature. Furthermore, the sodium-pool combustion rate depends on numerous factors such as sodium temperature, pool surface area and thickness, oxygen concentration, and so forth. During the combustion, sodium oxide aerosols are formed; a fraction of them being emitted in the gas phase and the remaining part deposited back in the pool. Depending on how this oxide layer is covering the sodium pool, combustion may not be able to last anymore. Indeed, while the oxide layer properly protects the sodium at low temperatures preventing oxygen to diffuse through and react with sodium; the oxide layer becoming porous at intermediate and high temperatures is no longer protective. The sodium ignition/combustion is maintained as long as the amount of heat produced from oxidation is higher than the amount of heat lost in the system [26].

[8] For significant breach or in the case of unburnt sodium during spray fires.

2. Spray fires[9]: The ignition of sodium sprays depends on its characteristics and of sodium temperature. Fire energy release is directly linked to the sodium-air interface that itself depends on the sodium spray characteristics (jet volume, droplet, size, spray duration). However, some generalizations can be made. Chemical oxidation reaction takes place when a droplet of sodium, comes in contact with atmospheric oxygen. The O_2 diffusion in the spray volume limits the combustion efficiency and the burned sodium mass finally depends on the ratio of ejected sodium mass to available O_2. The thickness of the oxide layer above the sodium core increases with time. Since it is an oxidation reaction (exothermic), temperature subsequently increases and the reaction gives rise to the production of sodium oxide aerosols in the atmosphere. Studies have shown that small sodium droplets may ignite even at room temperature if they are condensed from a vapor mist [32].

3. Mixed fires: It is a combination of spray and pool fires in the same containment volume. It is the most likely process to occur in the containment following a CDA and the combustion of expelled sodium. The sodium pool extension collecting the unburnt sodium from the spray will depend on the spray fire efficiency, itself, as already mentioned, determined by the sodium jet characteristics.

2.4.1 Sodium aerosol generation and aging

Sodium monoxide particles are formed in the flame as a result of the reaction between sodium vapor and, oxygen and vapor condensation. As for the ignition/combustion of sodium, the rate of sodium oxide formation is affected by the temperature of the sodium, the available reactive surface (sodium pool diameter or specific surface of sodium droplets) and the rate of oxygen transport to the combustion area. As sodium pool and spray fires have different burning characteristics and efficiency (mainly because the sodium surface area is more prominent in spray than in pool), the aerosol production and characteristics also differ between these two types of fires. Experiments have indeed shown that pool fires produce aerosol amounts ranging from 10% to 30% of the spread sodium, while for spray fires this amount is around 60% of the sprayed sodium [7].

The first oxidation reaction of Na(l) occurs very close to the exposed surface of Na, i.e., the zone of flame which has typically a thickness of about one cm. Sodium

[9] For small breach.

monoxide is formed by the combustion of sodium vapour, shown in reaction below. In the zone of flame, at about 1300°C, Na_2O is stable.

$$2\ Na\ (g) + ½\ O_2\ (g) \rightarrow \quad Na_2O\ (s),\ \Delta H^0_{298} = \text{-}100.7\ Kcal\ mole^{-1} \qquad \text{R 2-1}$$

Meanwhile, the surface of Na(l) where O_2 has diffused through the flame reacts with Na(l) to form a mixture of Na_2O and Na_2O_2, which can accumulate on the surface to form a crust that plays a self-extinguishing role for pool fires, by limiting the amount of O_2 entering in the pool.

$$Na_2O\ (s) + ½\ O_2\ (g) \rightarrow \ Na_2O_2(s),\ \Delta H^0_{298} = \text{-}\ 106\ Kcal\ mole^{-1} \qquad \text{R 2-2}$$

If the supply of O_2 is not limited, only peroxides will be formed. At this stage, the oxidation on the other hand reaction of Na(l) is complete, the reaction is written as:

$$2\ Na\ (l) + O_2\ (g) \rightarrow \ Na_2O_2(s),\ \Delta H^0_{298} = \text{-}120.6\ Kcal\ mole^{-1} \qquad \text{R 2-3}$$

The sodium oxide/peroxide aerosols can further react with available water vapour and carbon dioxide forming sodium hydroxide and carbonates. The final size and chemical composition of the aerosols is highly dependent on the ratio between sodium on one hand and CO_2 and H_2O.

The following two reactions show the hydration reaction of sodium oxide and peroxide aerosols, transforming it into more hazardous sodium hydroxide aerosol. The reaction to form hydroxides is very rapid, compared with the other reactions.

$$Na_2O\ (s) + H_2O\ (g) \ \rightarrow \ 2\ NaOH\ (s),\ \Delta H^0_{298} = \text{-}46.8\ Kcal\ mole^{-1} \qquad \text{R 2-4}$$

$$Na_2O_2\ (s) + H_2O\ (g) \ \rightarrow \ 2\ NaOH\ (s) + ½\ O_2\ (g), \qquad \text{R 2-5}$$
$$\Delta H^0_{298} = \text{-}124\ Kcal\ mole^{-1}$$

The hydroxide aerosol (more or less hydrated) is especially highly hygroscopic and deliquescent, meaning, it would have high affinity with the surrounding H_2O molecules. Depending on the relative humidity and the temperature, the NaOH particles can then be considered either under liquid or solid forms. These aerosols, still unstable and reactive, can further consume carbon dioxide present inside the containment to form substantially less toxic and fairly stable sodium carbonate aerosols which will, in turn, react with water vapor and carbon dioxide (if available) to finally form sodium bicarbonate which is chemically stable (at SA conditions) and

non-toxic. The available concentration of carbon dioxide and water vapor plays then an important role in the subsequent chemical transformation of sodium aerosols.

$$2\ NaOH\ (s\ or\ l) + \ CO_2\ (g) \ \rightarrow \ Na_2CO_3\,(s) + H_2O\ (g) \qquad \text{R 2-6}$$
$$\Delta H^0_{298} = -\ 40\ Kcal\ mol^{-1}$$

$$Na_2CO_3\,(s) + \ CO_2\ (g) + \ H_2O\ (g) \ \rightarrow \ 2\ NaHCO_3\,(s), \qquad \text{R 2-7}$$
$$\Delta H^0_{298} = -\ 30\ Kcal\ mol^{-1}$$

As already mentioned, a vast amount of research was done in the past (1960-80s) on sodium fires along with SFR safety analyses and studies. However, at that time, the studies mainly focused on sodium combustion energetics and its thermo-dynamical consequences (over-heating and over-pressurization) on the containment thermo-mechanical damage and integrity. In particular, many experiments were performed on both spray and pool fires in France and Germany along with the Superphénix safety studies.

Some experimental studies dedicated to the physics of sodium combustion aerosols were nevertheless performed. They indicate that the aerosols have a median diameter between 0.5 and 5 microns. The average concentrations of aerosols measured. In these studies range from 2 to 25 $g.m^{-3}$, depending if they were performed in a confined space or free atmosphere [33].

More recently, Subramanian *et al.,* and Baskaran *et al.,* carried out experiments in the aerosol test facility (ATF) in India where the aerosol physico-chemical behavior was also investigated [34], [35].

Understanding the sodium burning process and having a better knowledge on the sodium combustion aerosol behaviour and their chemical composition should be a major step forward for any safety evaluation of future SFRs. Indeed, as already mentioned, sodium aerosols are themselves responsible to a great extent for the radiological and chemical source term. In addition, their radiological impact is much higher if, in addition, they act as a vector for RN transportation. As both chemical and radiological source terms will depend on the chemical transformations of the former sodium oxides, it is then essential, as a first step, to properly model, these chemical reactions.

2.4.2 A Literature review on sodium aerosol aging modeling

As said previously, in the past, most analytical developments have concerned the sodium fire thermal-hydraulics and only few focused on combustion aerosol physics and chemistry. Studies carried out by Clough and Garland in 1971 [35], Cooper in

1980 [36], Ramsdale in 1989 [32], and the most recent modeling by A. Plantamp in 2016 [37], are discussed in this section.

Different kinds of models have been developed in the literature to simulate these physicochemical transformations. The most currently used, the so-called "core shrinking model" developed by Cooper [36], considers the solid state diffusion of reactive gasses (H_2O, CO_2) as the limiting step. However, it leads for sodium fire aerosols which are typically less than ten micrometres in diameter [38], in a swift (a probably overestimated kinetics rate) conversion of sodium peroxides into carbonates in representative conditions of a severe accident in SFRs (characteristic reaction times less than 10 s).

If most of the experimental analyses confirm that the oxidation of sodium into oxides (Na_2O and Na_2O_2), and the hydration reaction of the oxides to form NaOH are rapid; the reaction to form Na_2CO_3 was found to take about 10 minutes, at the time of atmospheric dispersion. The limiting step in the carbonation reaction could be the relative humidity in the atmosphere which indeed determines the physical state of NaOH, solid or liquid. Therefore, it is currently thought that the final chemical composition of aerosols would also depend on the containment relative humidity [6], [13].

The theoretical analysis of the thermodynamic characteristics of the products encountered during sodium fire, by Clough and Garland, has highlighted the phase change of sodium hydroxide according to the relative humidity where this compound was modelled to pass from a solid state to that of an aqueous solution for relative humidity higher than 35% [36]. Also, in their model, according to the experimental data, the limiting reaction during the chemical transformation of aerosols is the carbonation of NaOH, which is controlled by the diffusion of CO_2 in the solid or liquid NaOH phase.

For Ramsdale's model [32], mainly based on the experimental data from Cherdron *et al.,* 1985 [39] the carbonation of the NaOH aerosols is also estimated as the limiting step, but the conversion rate is, this time, controlled by the diffusion through the layer of solid carbonate. In their model as in previous Cooper's work, the evolution of the chemical composition is then described using a so-called shrinking core model. The primary parameter of this model is the diffusion of CO_2 through this layer of Na_2CO_3, where the diffusion coefficient has been estimated to be 10^{-9} $m^2.s^{-1}$. By comparison with the available experimental results of Hofmann *et al.,* (1979) [40], Cherdron *et al.*, (1984) and Subramanian *et al.,* (2009)[39], [34], the value of the CO_2 diffusion coefficients in Na_2CO_3 was then adjusted to 10^{-10} $m^2.s^{-1}$. More recent improvements of the Cooper model, based on new experimental measurements of the CO_2 diffusion coefficients through solid peroxide pellets ($5\ 10^{-9}$ $cm^2\ s^{-1}$) also lead to a very fast consumption of CO_2 and transformation of sodium combustion aerosols into sodium carbonates within SA conditions [7].

Therefore, the shrinking-core models have only been partially validated because the diffusion coefficients of CO_2 in Na_2CO_3 were adjusted on experimental data. These adjustments in the diffusion coefficients have to be made for alleviating the model lacks in modelling the high hygroscopic nature of NaOH compounds and in predicting the physical state variations of NaOH as a function of humidity.
Recently, Plantamp *et al.,* [6] developed and validated a new kinetic model for the conversion of sodium droplet into sodium carbonate using new experimental data from tests, primarily investigating the role of humidity in carbonation kinetics. The range of relative humidity (RH) and temperature studied was 30-60% and 55-80°C, respectively. For RH higher than 60%, the model predicts NaOH conversation rate of about 90%. The calculated time-scale for the complete conversion of NaOH to Na_2CO_3 was reported to be 50-60 minutes which is in a rather good agreement with the experimental results.

2.5 Iodine behavior in-containment SFR during severe accidents

Iodine chemistry in PWR containments during SAs has been the subject of a vast amount of research and development that highlighted important features for the radiological source term. In light of these results and considering, the upgraded safety objectives for Gen-IV reactors, the behavior of iodine in-containment SFR has also to be very well understood and should be further investigated. The primary focus shall be the specificity of iodine behavior with sodium and, as previously mentioned, on the interactions of gaseous iodine with sodium combustion aerosols are of primary concerns [41].

2.5.1 Background

Depending on the accidental scenarios, the conditions in which iodine is released may be different. Both fuel temperature and pressure before fuel pin break-up, and the conditions within which radionuclide releases will occur (i.e., in sodium channel voided or in Na boiling conditions) will determine the amount of released iodine and its chemical form (I_2, NaI). In general, the temperatures experienced by the SFR fuel in case of a SA are higher than in a PWR where the degraded fuel temperatures can reach in the center of the fuel pellet 4000K. Thus, in the fuel pin already, radionuclide releases under an elementary form can start in the form of a gas mixture, including iodine. When the relaxation phase occurs, i.e., after fuel pin break-up and the ejection of the gas mixture and molten fuel in the sodium channel (i.e., in Na vapor and/or liquid phase), those vapors will condense and other species could be formed. The NaI compounds usually considered as the primary species transporting iodine in the

primary coolant circuit usually applied for iodine release in non-saturated sodium pool where the iodine is quickly dissolved and then trapped by sodium. In that case, the fraction of iodine that would be vaporized would be very low because of the very low vapor pressure of NaI even at the sodium boiling temperature at one bar (1-2 kPa which will be even lower in case of a diluted solution of iodine).

However, once the sodium is ejected inside the containment, the chemical reactions of sodium with the containment atmosphere (O_2, H_2O) or with the gases released from the containment concrete heating (H_2O, CO/CO_2) as well as the subsequent increase of the sodium temperatures (in sodium flame ~ 1300°C, in sodium pool ~ 600°C) might change the radionuclide speciation and repartition between the condensed (former state) and gaseous phase. It would be mainly the case for iodine where the thermal decomposition of NaI (dissolved in sodium) in the air, forming I_2 or HI, is expected since ambient temperature (though the decomposition at this temperature is low).

$$NaI\ (s) + H_2O(g) \rightarrow NaOH\ (s) + HI\ (g) \qquad \text{R 2-8}$$

$$2\ HI\ (g) \rightarrow I_2\ (g) + H_2\ (g) \qquad \text{R 2-9}$$

Taking into account the containment thermal hydraulic conditions during and/or after the fires (average gas temperatures ranging from ambient temperatures up to 200°C), I_2/HI could remain highly volatile and further leads, as in PWR accidental conditions, to the formation of highly volatiles organic iodides (i.e., CH_3I) and/or iodine oxides by respectively reaction of I_2 with organic materials (such as dyes, insulation, lubrication materials, cables or paints) and air radiolysis products (see Figure 2-4). Since CH_3I, the most likely organic species to be formed in that case, is highly volatile it could further penetrate particle containment filters and be troublesome to be trapped otherwise. That is why once released it would significantly contribute to the radiological source term even if the containment integrity is not lost.

For high humidity ratios, the situation might even be more complicated, with the formation of aqueous solutions of hydroxides and/or carbonates which could also react with I_2 by forming back iodates and iodides through the following reactions:

$$3\ I_2 + 6\ NaOH \rightarrow NaIO_3 + 5\ NaI + 3\ H_2O \qquad \text{R 2-10}$$

$$3\ I_2 + 3\ Na_2CO_3 \rightarrow NaIO_3 + 5\ NaI + 3\ CO_2 \qquad \text{R 2-11}$$

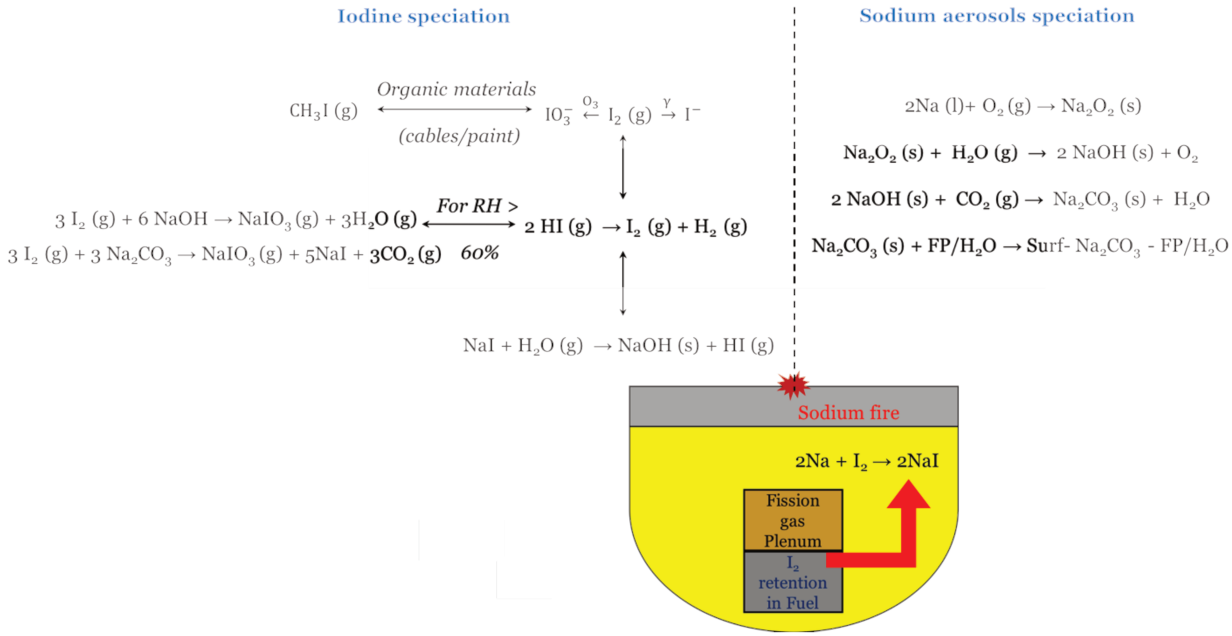

Figure 2-4 Schematic figure showing the in-containment iodine and sodium aerosols speciation in SFR containment under postulated energetic SA.

In comparison to PWRs, the volatile iodine-based FPs (I_2, HI, CH_3I) chemistry inside the SFR containment could be significantly different due to sodium. In particular, the sodium combustion aerosol physicochemical behavior could significantly impact the radiological source term. Under some favorable thermodynamic conditions the trapping of volatile FPs might be indeed favored. That is why it is of utmost importance to have a better knowledge of the interactions between I_2/HI and sodium aerosol species produced during the fires.

In summary, whenever the reactor top vault will be damaged during the SA scenario, NaI (dissolved within the ejected Na) and I_2 are the most expected species to be released inside the containment.

2.5.2 Experimental studies on iodine behavior in sodium pool conditions

Only a few experimental data are available regarding the iodine behavior in sodium pool combustion conditions [42], [43]. In addition, the results from these experiments are only qualitative and do not allow to draw any conclusions nor to derive any kinetic information.

This section especially aims to summarize the experiment performed with I_2 in the past within the FANAL program [20], [43]. This experimental investigation was performed in the 1970s at IPSN (Institute of radio-protection and Nuclear safety,

former IRSN) at Cadarache nuclear research center, France. The FANAL program consisted of 12 distinct experiments which investigated the radionuclides emissions from a sodium pool fire and the interactions between sodium aerosol combustion products and radionuclides. One of these experiments (FANAL 13) is of primary interest for this work, as it concerned the study of molecular iodine interaction with the sodium combustion products when it is released separately from the pool fire, see Figure 2-6.

The schema of the FANAL test is shown in Figure 2-5. In a first step, an I^{131} aqueous solution was deposited drop-by-drop, onto a plate. In a second step, the liquid medium was then evaporated with a strong flow of dry argon gas. The radioiodine covered plate was then placed on the generation system underneath the sodium burn pan, where it was heated to generate iodine vapors into a flow (1.5 L min^{-1}) of hot air over the first 30 minutes of the test. The Na-fire involved the combustion of 5 kg of Na-metal, and the sodium pool fire lasted for about 40 minutes until the fire self-extinguished due to the lack of oxygen. The aerosol and iodine concentration in the gas phase was measured for the entire length of the test using a set of glass-fiber + knit-mesh and TEDA-impregnated charcoal filters. Additionally, after the test, the walls, floor and ceiling of the vessel were washed for mass balance closure. There were no direct measurement of the release rates of sodium aerosols from the fire and iodine from the iodine generation system during the test, but their cumulative releases were estimated from air concentration measurements against time and final deposition measurements [20].

For both sodium/iodine aerosols and iodine vapor, the release rates were found to be highest during first 30 min of the test. The sodium aerosol concentration peaked after about 30 min, and, as predicted, dropped as sodium fire started to vanish due to the lack of oxygen. The I^{131} concentration rapidly felt after the generator was stopped, indicating that the I_2 vapors rapidly reacted with airborne and deposited sodium aerosols.

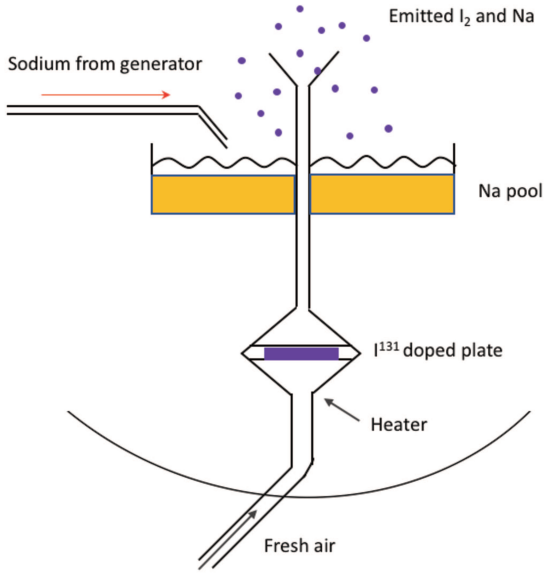

Figure 2-5 Schematic diagram of radioactive I^{131} generation system from I_2 (s), employed in FANAL test. The diagram also shows Na (l) pool and the sodium supply line.

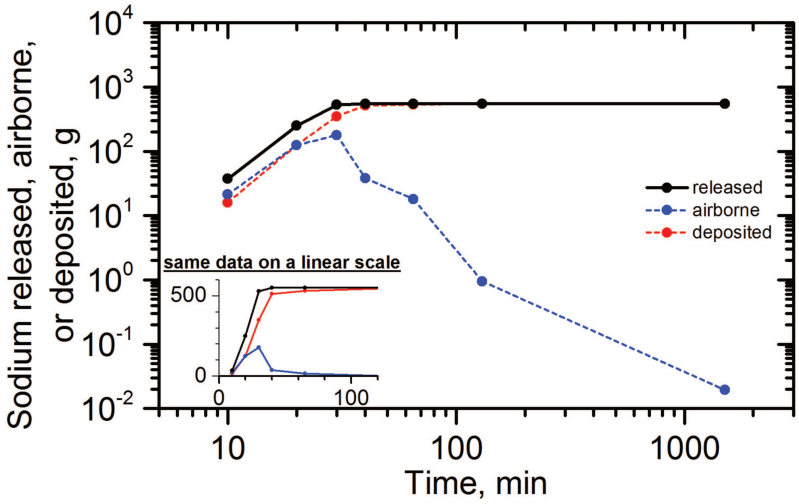

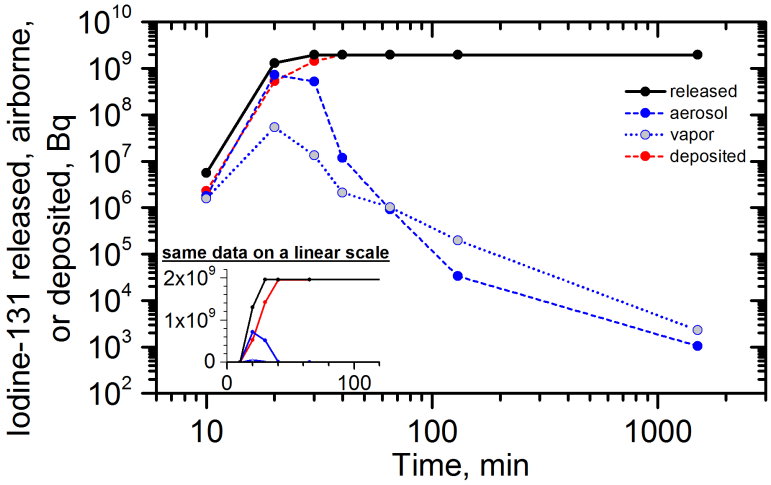

Figure 2-6 Releases of sodium aerosols and I^{131} vapor in FANAL 13, including the total airborne I^{131} in vapor form and aerosol form [20].

The FANAL test does not give enough information on the mechanisms of the chemical reactions between radioiodine vapors and Na-aerosols. Indeed, it is not possible from this single test to investigate the individual contributing factors such as temperature effects, effects of particle size, the influence of partition of Na-combustion aerosols and, so forth. The main outcome of the test is to check if radioiodine reacts rapidly with Na-combustion aerosols whether these are airborne or deposits. After the test, when the walls and the ceiling were washed, 550 g of sodium was found emitted from the Na-fire and, 18.5×10^9 Bq of I^{131} (which is within 5% of the balance done with measurements of the radioiodine plate in the generation system before and after the test) was measured in the deposits as well.

FANAL-13 is the only test available in the literature to study Na-aerosol and radioiodine interactions. The results reported provided useful qualitative information, but it was difficult to make broad generalizations from this single test. Nevertheless, form the experimental results analysis, the overall reaction order and kinetic constants were respectively estimated around 2 and 1.4×10^{-10} $Bq^{-1}.kg^{-1}.s^{-1}$. Further investigations are however required to have the further understanding of the reaction phenomena and a methodology to quantitatively estimate the I_2 adsorption on sodium fire combustion product surfaces which lead to the crux of this thesis then restricted to the study of sodium carbonates.

2.6 Thesis objectives and approaches

As explained in the previous sections, gaps in knowledge regarding the in-containment FP behavior have motivated this research. It is the purpose of this thesis to bring knowledge to the field of heterogeneous reaction between I_2 (g) and Na_2CO_3 (s). Both kinetic and thermodynamic aspects of the reactions were studied.

The opted strategy was a multi-scale investigation using theoretical chemistry, ab-initio DFT methods combined with ab-initio thermodynamics. This facilitated us to obtain thermodynamic properties of the possible interactions at atomic scale. In parallel, experimental investigations using two distinct setups were performed to study the interactions and their kinetics on a macroscopic scale.

In this manuscript, the combined experimental and theoretical approach will be presented, discussed, and the results are compared. This research attempts to answer the following specific questions:

- Does I_2 (g) significantly interact with Na_2CO_3 (s)?
- What is the quantitative I_2 (g) uptake on Na_2CO_3 (s) sorbent surfaces and their kinetics?
- What are the thermodynamics and kinetics of adsorption/desorption of reacted I_2 (g) from the Na_2CO_3 (s) sorbent surface?

Beyond these specific objectives, the work is also intended to develop a theoretical approach and model for I_2 (g) adsorption on sodium carbonate surfaces in a way that could be further extended to others gaseous FP and sodium aerosol species. This way, once the methodology is validated for I_2 (g) and Na_2CO_3 (s) system, it can be extended to other radionuclides (Ru, being volatile and toxic is one of another important concerns) and aerosol surfaces of interest without performing experiments. Experiments involving the use of sodium and radionuclides are indeed always difficult to design and tedious in execution.

Chapter 3 Theoretical tools

The interactions between Na_2CO_3 (s) and I_2 (g) are of crucial interest. However, the thermodynamic and kinetic data of their interactions have not been studied in the past. Experiments were performed aimed to study the adsorption of I_2 on sodium fire aerosols in the 1970s [43] (FANAL experiments, discussed in Section 2.5.2), but no characterization of the interactions and thermodynamic data, such as the residual partial pressure of I_2, surface coverage, and desorption of I_2 from the surface were addressed. One major challenge in the experimental study of these reactions is the isolation of sodium aerosols because of their intrinsic instability in the uncontrolled atmosphere.

In this work, we propose a multiscale methodology to study these interactions and investigate their thermodynamic properties. A brief background on the description of an atomic level system using quantum chemistry theories, tools and their extrapolation to temperatures and pressures of interest is presented in this chapter. At the atomic scale, the density functional theory (DFT) is the most commonly used electronic structure method, when dealing with systems containing a large number of atoms. High level of accuracy, using theoretical chemistry tools is limited to small systems. For realistic applications, with a significant number of valence electrons, several approximations have to be made. The major challenge is to find a balance between accuracy of the results and computational cost. As mentioned earlier, this work follows a multiscale approach; microscopic properties such as surface stabilities and adsorption energies at 0 K were determined using theoretical chemistry tools. Those results have been extended to (T, P) of interest in order to deduce some macroscopic properties such as adsorption isotherm and total iodine gas uptake. Such an extrapolation is possible using statistical thermodynamics and could be confronted with experimental measurements. A brief review of theories used is presented in this chapter. Interested readers can find a detailed description in numerous review articles [44]–[46] and books [47], [48] that discusses quantum chemistry theories in greater detail and depth.

This chapter is divided into four major sections. First, an introduction to quantum chemistry is discussed; electronic structure theories – Hartree-Fock, DFT and their implementation are introduced; the concept and applicability of different functionals

are discussed. Finally, the extrapolation of data using ab-initio thermodynamic theories and correlations are briefly reviewed.

3.1 Background

Classical mechanics fails to describe a system on a molecular or atomic scale as the duality of the matter shall be considered for atoms/molecules. This is when quantum mechanics can be applied to describe the state of an atomic system. According to the fundamental postulate of quantum mechanical theory, the energy of an n-particles system can be fully described in the form of wavefunction $\psi_n(x_1, x_2, x_3, \dots, t)$ where ψ is the time-dependent wave function; $x_1 \equiv$(r, s) are the spatial and spin coordinates of the particles 1, 2, 3…; and t is the time. In this work, we are interested to have insights on the stationary states of the system; hence the time-independent Schrödinger equation will be used. For many-body systems consisting of N electrons and M atoms, the time-independent Schrödinger equation reads:

$$\boldsymbol{H}\psi(x_1, x_2, x_3, \dots., R) = E\psi(x_1, x_2, x_3, \dots, R), \qquad 3\text{-}1$$

where ψ is the time-independent wave function of the system, x and R, are coordinates of the electrons and nuclei, respectively. Pauli's exclusion principle (which is a product of antisymmetric principle), states that two fermions cannot occupy identical quantum states. Otherwise speaking, two fermionic particles cannot have the same set of quantum numbers.

The total energy of a system is obtained by applying the Hamiltonian operator, H to the wave function. The Hamiltonian is the sum of kinetic and potential energy operator (H = T + V).

In principle, Equation 3-1 is solved by finding the eigenstates (ψ) and the eigenvalues (E) of the Hamiltonian. The wavefunction with the lowest energy represents the ground state of the system. The Hamiltonian of the many-body system is expressed as:

$$\mathrm{H} = \mathrm{T_n} + \mathrm{T_e} + \mathrm{V_{n\text{-}e}} + \mathrm{V_{n\text{-}n}} + \mathrm{V_{e\text{-}e}}\ , \qquad 3\text{-}2$$

where the subscript n denotes nuclei and e denotes electrons. The last three terms respectively describe the potentials arising from the interactions between nuclei and electrons, between the nuclei, and between the electrons. The Hamiltonian in Equation 3-2 is written in full form as:

$$\boldsymbol{H} = -\sum_i \frac{1}{2}\nabla_i^2 - \sum_A \frac{1}{2M_A}\nabla_A^2 - \sum_{i,A} \frac{Z_A}{r_i A} + \sum_{i<i} \frac{1}{r_{ij}} + \sum_{i,A} \frac{Z_A Z_B}{R_{AB}}, \qquad 3\text{-}3$$

where subscripts i and j are for electrons and A, B for nuclei. The first and second terms are electron and nuclei kinetic energy, respectively. The third, fourth, and the

fifth terms are electron-nucleus coulomb attraction, electron-electron repulsion, and the nuclear-nuclear repulsion. Equation 3-1 and 3-3 provide a complete description of a system consisting of N electrons and M atoms (neglecting the relativistic effects and time dependence). In principle, this equation can be solved analytically for systems with one electron, like hydrogenoïde atoms. However, as mentioned previously, solving these equations for a realistic system with multiple electrons is very challenging. To give the reader idea and magnitude of the problem in hand, a system with 20 Na atoms (each atom with 11 electrons) has N and M values of 220 and 20, respectively. This means that $\psi(\mathrm{r},\mathrm{R})$ is a 720-dimensional function (each nucleus and electron has three spatial coordinates). With current computing technologies, solving a 720-dimentional equation is not feasible. The rest of this section will discuss the approximation methods and mathematical techniques to make such computations practically possible.

Born and Oppenheimer approximation

The Born-Oppenheimer approximation [49] separates the wavefunction into two parts: nuclear and electronic wavefunction. It makes use of the fundamental fact that the mass of an atomic nucleus in a molecule is much larger than the mass of the electron (more than at least one thousand times). As a result, the motion of the nucleus can be neglected. It can be said that the electrons in a molecule move in the electrostatic field generated by the so-called stationary nuclei. This approximation implies that the electron distribution in a molecular system is a function of nuclear position. With this theory, a system with a given set of nuclear coordinates can be solved with the electronic Schrödinger equation as follows:

$$\mathrm{H_e}\psi(\mathrm{r})=\mathrm{E_e}\psi(\mathrm{r}), \qquad 3\text{-}4$$

where $\mathrm{H_e}$ and $\mathrm{E_e}$ are electronic Hamiltonian and electronic energy, respectively. The electronic Hamiltonian is written as, rewriting equation 3-3:

$$\mathbf{H}_e = \sum_i \frac{1}{2}\nabla_i^2 - \sum_{i,A}\frac{z_A}{r_i A} + \sum_{i<i}\frac{1}{r_{ij}} + \sum_{A<B}\frac{z_A z_B}{R_{AB}}. \qquad 3\text{-}5$$

The solution of Equation 3-4 gives the electronic potential to guide the motion of the nuclei. On the other hand, the motion of nuclei can be approximated by classical mechanics, and the forces acting on the atoms are determined using the Hellmann-Feynman theorem [50].

3.2 Hartree-Fock scheme

3.2.1 Mean-field approximation

Hartree-Fock theory states that each electron's motion can be described by a single-particle function, also known as spin-orbital. Moreover, this motion is explicitly independent of the instantaneous motion of other electrons. The n-electron wavefunction is written as a functional of n one-electron functions. The one-electron is assumed to move in an average field generated by the (n-1) electrons, referred to as mean field. Fock and Slater proposed a variational approach for the total wavefunction with an assumption that the exact many-body wavefunction can be represented by the so-called Slater determinant of N spin-orbitals, which satisfies both, anti-symmetry and Pauli's exclusion principle. The resultant wavefunction is thus written as:

$$\psi_{\mathrm{HF}} = \frac{1}{\sqrt{\mathrm{N!}}}\begin{bmatrix} \varphi_1(\mathrm{x}_1) & \varphi_2(\mathrm{x}_1)\ldots & \varphi_{\mathrm{N}}(\mathrm{x}_1) \\ \varphi_1(\mathrm{x}_2) & \varphi_2(\mathrm{x}_2)\ldots & \varphi_{\mathrm{N}}(\mathrm{x}_2) \\ \vdots & \vdots & \vdots \\ \varphi_1(\mathrm{x}_{\mathrm{N}}) & \varphi_2(\mathrm{x}_{\mathrm{N}})\ldots & \varphi_{\mathrm{N}}(\mathrm{x}_{\mathrm{N}}) \end{bmatrix}, \qquad 3\text{-}6$$

where φ is the spin-orbital which is merely the product of a spatial orbital and the spin function; such that $\varphi(\mathrm{x}) = \phi(\mathrm{r})\omega$, and x includes the coordinates of space and spin. The expansion of orbitals in atomic basis set is presented in Section 3.5.3. The use of Slater determinant forces the mathematical formulation to respect the anti-symmetry principle, and, in addition to it, the indistinguishability of electrons is also established as each electron is associated with every orbital. The HF energy can be written by using fundamental quantum mechanical expression, in Dirac notation (normalized wavefunction, as: $\langle\psi|\psi\rangle = 1$):

$$\mathrm{E_{el}} = \langle\psi|\mathrm{H_{el}}|\psi\rangle. \qquad 3\text{-}7$$

To have a better approximation of ψ, the variational theorem shall be used, according to which the determinant giving the lowest energy is the solution closest to the exact wavefunction of the ground state, hence the optimized orbitals are those which minimize the $\mathrm{E_{el}}$. Skipping the rigorous mathematics which can be found in the literature[51], the Hartree-Fock energy, E_{el}, reads:

$$E_{HF} = \sum_i \langle i|h|i\rangle + \frac{1}{2}\sum_{ij}[(ii|jj) - (ij|ji)], \qquad 3\text{-}8$$

where $\langle i|h|j\rangle$ is mono-electronic energy, $(ii|jj)$ is Coulomb's energy and $(ij|ji)$ is exchange energy. The latter is a result of anti-symmetrization of the wavefunction.

$$\langle i|h|j\rangle = \int dx_1 \varphi_i^*(x_1) h(r_1) \varphi_j(x_1), \quad 3\text{-}9$$

$$(ii|jj) = \int dx_1 dx_2 \emptyset_i^*(x_1) \emptyset_j^*(x_2) \frac{1}{r_{12}} \emptyset_i(x_1) \emptyset_j(x_2).$$

$$(ij|ji) = \int dx_1 dx_2 \emptyset_i^*(x_1) \emptyset_j^*(x_2) \frac{1}{r_{12}} \emptyset_j(x_1) \emptyset_i(x_2).$$

The core of the HF approximation is to replace the complicated many-electron problem with one electron problem in which electron-electron repulsion is treated in an average way which might lead to an inadequate description of the electronic structure. The HF ground state energy is the upper bound to the exact-ground state energy, ∂_0.

$$E_{corr} = \partial_0 - E_0 \quad 3\text{-}10$$

The difference is termed as the correlation energy which is often too large to be ignored. The calculation of this difference, the correlation energy, ∂_0, is performed by using the so-called post-HF methods, which are explained in the next section.

3.3 Electron correlation methods

The primary flaw of the HF theory lies in the one Slater determinant approach. For higher accuracy, the wavefunction has to be expanded over several Slater determinants. The exact form of n-electron wavefunction can be expanded using a finite number of Slater determinants as:

$$|\psi_n\rangle = C_0^{(n)} |\phi_0\rangle + \sum_{ar} C_a^{r(n)} |\phi_a^r\rangle + \sum_{\substack{r<s \\ a<b}} C_{ab}^{rs(n)} |\phi_{ab}^{rs}\rangle + \cdots \quad 3\text{-}11$$

Equation 3-11 includes all possible excitation states. $|\phi_a^r\rangle$ and $|\phi_{ab}^{rs}\rangle$ are the singly and doubly excited determinants, respectively. For convenience, these determinants are often referred to as Singles (S), Doubles (D),… ,etc. Alternatively, Equation 3-11 can be written as:

$$\psi = \sum_{k=0}^{k_{max}} C_k D_k \,, \quad 3\text{-}12$$

where D_k fully spans the Hilbert space of the wavefunction. The determinants used are a complete set of N-electron functions while D_0 is the ground-state HF

determinant. In principle, a very large number of configurations, expanded in Slater determinants, are required to have the exact many-body wavefunction. The number of Slater determinants which can be included in Equation 3-12 for N-electrons and M-basis functions can conceptually reach:

$$C_M^N \text{ or } k_{max} = \frac{M!}{N!\,(M-N)!} \qquad 3\text{-}13$$

If the basis set is complete, the solution of the so-called Full configuration-interaction (FCI) approach is exact. Conceptually, this method is exact and elegant, but, on practical grounds it is expensive hence can only be applied to only small systems. Approximations to full-CI method are discussed in the next section.

3.3.1 Approximations

The full-CI method is limited for very small systems and cannot be applied for larger number of electrons as K_{max} become notoriously high and hence computationally prohibitive. Approximations have to made to limit the number of Slater determinants to be taken into account for the wavefunction. Two families of post-HF method can be distinguished.

Mono-reference methods

In these methods, the HF spin-orbitals are not affected during the calculations of the coefficients of Slater determinants involved in the wavefunction. There are two ways of truncation to reduce the computational effort.

- Truncation in space of determinants: In this method, determinants beyond a chosen order of excitation are omitted, in the expression of wavefunction. Example, configuration interaction Singles and Doubles (CISD).
- Truncation in space of coefficients of determinants: In these methods, all determinants are considered but their coefficients are truncated at a given order. Example perturbation theory (PT) and the coupled-cluster (CC) method. These methods are not variational.

Multi-reference methods

HF spin orbitals are optimized to have the most suitable mono-determinantal wavefunction (the HF determinant itself). However, they are not necessarily the best to describe multi-determinantal wavefunction. In multi-reference methods, the optimization of the orbitals is performed in parallel with the optimization of 'generally-exact-wavefunction' in reduced spin-orbital space (reduced active space). Examples are, Complete Active Space-Self Consistent Field (CAS-SCF). Once this multireference wavefunction is described in this reduced space, one can generally use

one of the methods explained previously. Examples are CAS-PT and MR-CI methods.
This way, a trade-off between computational cost and accuracy can be made.

3.4 Density Functional Theory

A brief review of the density functional theory of electronic structure is presented in this section. DFT simplifies the N-electron wavefunction, $\psi(r_1, r_2, r_3 \ldots, r_n)$ and the associated Schrödinger equation with a simple quantity – the electron density which is a function of three spatial variables.

3.4.1 Thomas-Fermi model: the root of DFT

In the 1920s Thomas and Fermi proposed a theory of deriving the electronic energy using the electron density distribution, n(r), which could calculate the ground state properties such as total energies of atoms [52]. The root of this theory lied in the idea that the statistical considerations can be used to approximate the distribution of electrons in an atom. Moreover, the presence of an effective potential field which is "determined by the nuclear charge and this distribution of electrons." In a nutshell, the TF theory considered interacting electrons are moving in an external potential v(r), and gave an implicit relation between v(r) and the density distribution, n(r), which could be written in the form[53]:

$$n(r) = \gamma\, [\, \mu - V_{eff}(r)]^{3/2}, \quad \gamma = \frac{1}{3\pi^2}\left(\frac{2m}{\hbar^2}\right)^2, \tag{3-14}$$

$$V_{eff}(r) = v(r) + \int \frac{n(r')}{|r-r'|}\, dr', \tag{3-15}$$

where μ is the position independent chemical potential. The second term in equation 3-15 is the classically computed electrostatic potential generated by the electron density distribution n(r'). The TF theory was a crude and rough approximation of the exact solution of many-body Schrödinger equation. The TF theory was expressed in terms of n(r) and the Schrödinger equation in $\psi(r_1, r_2, r_3 \ldots, r_n)$. However, there was a lack of strict connection between them. DFT acts as bridge between the two approaches as it can be expressed entirely in terms of the density, n(r), in the Hohenberg-Kohn formalism and in terms of single particle wavefunction, $\psi(r)$, in the Kohn-Sham formalism; this is explained in detail in the coming sections.

3.4.2 Hohenberg-Kohn Formulation

Hohenberg and Kohn formulated the fundamental theorems[54] behind DFT which proved that the electron density distribution could uniquely determine the total energy of the system. According to the first theorem, the ground state properties of the system such as its energy and wavefunction are unique functional of n(r). In other words, it states that there is a one-to-one mapping between the external potential, $V_{ext}(r)$, to which the electrons are subjected and the electron density, n(r), of the systems in the ground state. The $V_{ext}(r)$ therefore uniquely determines electron density. The electronic energy, E, of a system can be thus written in the form of a functional, $F[n(\boldsymbol{r})]$ which is a universal functional valid for any number of electrons and $V_{ext}(r)$[54].

$$E[n(r)]= \int V_{ext}(r)n(r)dr+F[n(r)]. \qquad 3\text{-}16$$

The second theorem of Hohenberg and Kohn states that a correct ground state electron density is the one which minimizes E[n(r)]. The condition constrains the minimization:

$$\int n(r)dr = N. \qquad 3\text{-}17$$

According to the two theorems of Hohenberg and Kohn, a determination of the ground state properties of N interacting electrons in a given external potential $V_{ext}(r)$ is reduced to a minimization problem of the functional E[n(r)]. Now, the only unknown which remains is the universal functional, F[n(r)]. An explicit form of F[n(r)] is unknown. Thus the primary challenge is associated with the knowledge of F[n(r)]. Thanks to Kohn-Sham equations[55] which provide a way to approximate F[n(r)].

3.4.3 Kohn-Sham Equations

Kohn and Sham reformulated the energy functional, E[n(r)], in terms of Coulomb interaction, kinetic energy, and exchange-correlation energy, which can be written as:

$$E[n(r)]= \int V_{ext}(r)n(r)dr+\frac{1}{2}\iint \frac{n(r)n(r')}{|r- r'|}\, dr\, dr' + T_s[n(r)]+ E_{XC}[n(r)], \qquad 3\text{-}18$$

where Coulomb interaction energy between electrons is given by the second term, the kinetic energy of non-interacting electrons of density n(r) by T_s, and the

exchange and correlation energy of interacting electrons of density n(r) by E_{XC}. The presented form of E[n(r)] in equation 3-18 is exact since the E_{XC} term includes all of the energies that are not represented by the rest of the terms in the equation. Now, E_{XC} does not only include the exchange and correlation energies due to the Pauli exclusion principle and quantum mechanical electronic repulsions, but also the correlation term omitted by accounting only for the kinetic energy of non-interacting electrons in T_s. Thus the electron density, n(r), can be reconstructed with the a mono-determinant wavefunction of the electrons, $\psi_i(r)$, by:

$$\psi_{KS} = \frac{1}{\sqrt{N!}}\begin{bmatrix} \varphi_1(x_1) & \varphi_2(x_1) \dots & \varphi_N(x_1) \\ \varphi_1(x_2) & \varphi_2(x_2) \dots & \varphi_N(x_2) \\ \vdots & \vdots & \vdots \\ \varphi_1(x_N) & \varphi_2(x_N) \dots & \varphi_N(x_N) \end{bmatrix},$$

The kinetic energy of non-interacting electrons, $T_s[n(r)]$, will be then:

$$T_s[n(r)]=T_s\left[\{\psi_i\}_{i=1}^{N}\right]= \frac{1}{2}\sum_{i=1}^{N}\int |\nabla_r \psi_i(r)|^2 \, dr. \qquad 3\text{-}19$$

The minimization process that provides the ground state energy also determines the corresponding wavefunction of the electrons. Therefore, the ground state energy depends only on n(r). Finally, the only term in Equation 3-18 that remains unknown is E_{XC}. The approximation of E_{XC} is explained in the following section.

3.4.4 The Approximations for exchange-correlation term

The exchange-correlational functional, E_{XC} can be defined as:

$$E_{XC} = E_X + E_{C.} \qquad 3\text{-}20$$

Alternatively, regarding exchange and correlation per particle, as:

$$E_X[n(r)]= \int \epsilon_X\big(n(r)\big)\, n(r) dr. \qquad 3\text{-}21$$

$$E_C[n(r)]= \int \epsilon_C\big(n(r)\big)\, n(r) dr. \qquad 3\text{-}22$$

where ϵ_X and ϵ_C is the exchange and correlation energy per particle.

For example, in uniform electron gas of density n, the exchange part in atomic units is given by [53]:

$$\epsilon_X(n) = -\frac{0.458}{r_s}, \qquad 3\text{-}23$$

where r_s is the radius of the sphere containing one electron and is given by $(4\pi/3)r^3$. The correction part was first estimated by:

$$\epsilon_C(n) = -\frac{0.44}{r_s + 7.8}. \qquad 3\text{-}24$$

The most streightforward approximation for $E_{XC}(n(r))$ is the so-called LDA, $E_{XC}^{LDA}[n(r)]$.

Studies have shown that the LDA works quite well for calculating the ionization energies of atoms, dissociation energies of molecules and cohesive energies with an accuracy of typically 10-20% [56], and bond lengths, geometries of molecules and solids with an accuracy of about 1%.

The LDA is exact for a uniform electron gas and could be applied to the limiting case of the densities varying very slowly on the scale of local Fermi wavelength. However, the limiting case mentioned above is not satisfied in solids and molecules, and hence this condition is severely violated in situations where the density undergoes rapid changes. Additionally, the LDA can fail in systems with massive fermionic systems, dominated by electron-electron interaction effects; this lacks any resemblance with non-interacting electron gas.

An improvement to this can be made by addressing the inhomogeneity of the electron density and adding the dependence in its gradient into the exchange-correlation energy expression. The so-called Generalized Gradient Approximation (GGA)[57] is written as:

$$E_{XC}^{GGA}[n(r)] = \int \epsilon_{XC}(n(r), \nabla n(r))\, n(r) dr. \qquad 3\text{-}25$$

The GGA functional can be enhanced by considering the Laplacian of the density leading to so-called meta-GGA functional.

The GGA type functional and in particular the one developed by Perdew, Burke and Ernzerhof (PBE)[58], is the most widely used in the materials research field and gives a successful description of processes such as adsorption phenomena, adsorption sites, geometry, and relative stability [59]. For the entire work in this thesis, the PBE functional is used.

van der Waals Functionals

Dispersion (van der Waals) forces are present as a result of long-range electron correlation effects which are absent from local and semi-local density functionals [60] but these functionals are desirable to have an better description of the system[61] [62] [63].

A refined form of E_{XC} can be written as:

$$E_{XC} = E_X^{GGA/LDA} + E_C^{GGA/LDA} + E_C^{non-local} \quad 3\text{-}26$$

The non-local electron correlational term, $E_C^{non-local}$, depends explicitly on the position vector. The classes of vdW type functionals developed in earlier times include the dispersion interaction by adding a correction term with a $-1/r^6$ asymptotic behavior [60]. The DFT-D3 method, proposed by Grimme *et al.*[64] has been used in this work.

The total DFT-D3 energy is given by:

$$E_{DFT-D3} = E_{KS-DFT} + E_{disp}, \quad 3\text{-}27$$

Where $E_{KS\text{-}DFT}$ is the energy calculated by the general KS equations, and the E_{disp} is the dispersion correction as a sum of two and three-body energies. Unlike other methods, this approach computes the dispersion coefficients using an ab-initio method instead of empirically driven interpolation. A detailed derivation of the E_{disp} can be found in the literature [64]. The final form of vdW-energy expression used in the DFT-D3 method is:

$$E_{disp} = -\frac{1}{2}\sum_{i=1}^{N}\sum_{j=1}^{N}\sum_{L}\left[f_{d,6}(r_{i,j}L)\frac{C_{6ij}}{r_{ij,L}^6} + f_{d,8}(r_{i,j}L)\frac{C_{8ij}}{r_{ij,L}^8}\right]. \quad 3\text{-}28$$

Parameters like cut-off radius for the calculation of pair interactions and coordination number is adjusted in the algorithm, based on the system under study. The computed dispersion coefficients are geometry-dependent, they are adjusted on by local geometry (coordination number in the algorithm) around atoms i and j.

3.5 Implementation of DFT

3.5.1 Basic Algorithm

The algorithm DFT typically starts with is first reading the input files and extracting necessary information about the system, such as atomic number, number of electrons, and positions of atoms etc. Then KS equations are solved using the SCF cycle [55].
The KS Hamiltonian is effective Hamiltonian as Hartree term, and it depends on orbitals, which are eigenvectors of Hamiltonian. Such a dependence induces the need of an iterative prosses.
The iterative numerical implementation of Kohn-Sham equations is referred to as a self-consistent field (SCF) computation. Figure 3-1 shows a flowchart of the SCF implementation. The first step is to provide a starting guess for the electron density; the KS equations are then solved which would result in a new density. The new density is compared with the trail density, and the program continues until it reaches the desired accuracy. Once convergence is achieved, the results are printed in the output file.

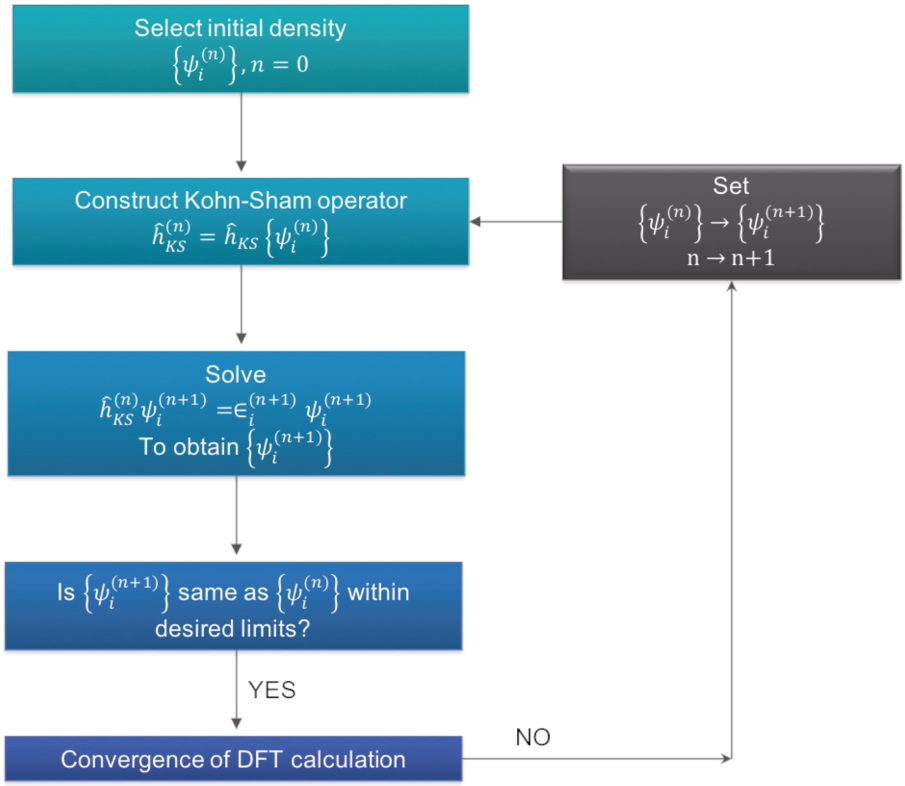

Figure 3-1 The self-consistency field (SCF) procedure.

3.5.2 Structure Relaxation

As mentioned before, within the Born and Oppenheimer approximation the nuclei are assumed to be stationary, and the electrons move in the field generated by the stationary nucleus. After every SCF cycle, the forces acting on atoms are calculated according to the Hellmann-Feynman theorem[50] and the optimal interatomic distances are determined. Forces acting on the atomic nuclei are minimized as a result of which the total energy is also minimized. This way the optimal atomic structure is found which is also referred to as structure relaxation or geometry optimization. A simplified computational procedure of the structure relaxation computation is illustrated in Figure 3-2. Various levels of constraints such as letting a subset of atoms in the cell move, restricting the degree(s) of freedom, relaxing all degrees of freedom including volume can be imposed in the structure relaxation computation. The atoms that are set free to move freely along the spatial coordinates are called as "relaxed" and the opposite are called "frozen".

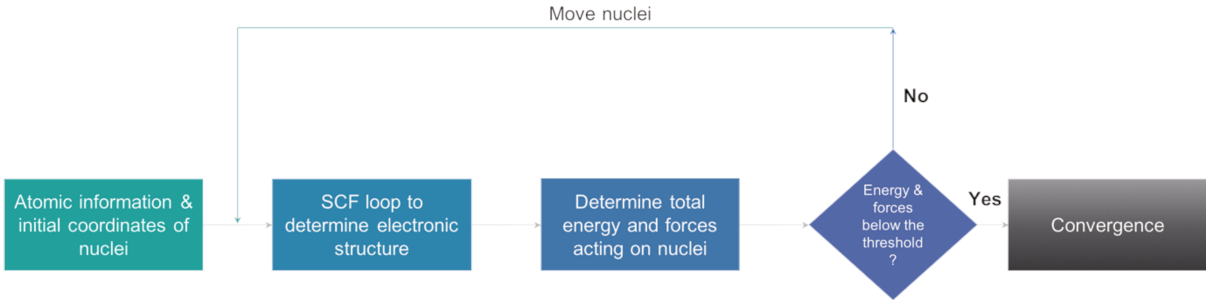

Figure 3-2 Computational procedure of a structure relaxation computation.

3.5.3 Basis Sets

To solve the single-particle KS equations, the single-electron wavefunctions must be expanded in terms of a basis. This transforms the series of integro-differential single-particle Schrödinger equations, into a matrix equation which can be solved computationally in an efficient fashion.
The following types of basis functions are widely used in DFT codes: Atomic Orbital (AO), Gaussian, Augmented and Plane Waves (PW). All of the computation results presented in this thesis are performed with VASP package [65] [66] which uses a PW basis set and periodic boundary conditions.

Atomic orbitals

An intuitive way to solve the equations of DFT is provided by the basis sets. Usually, for an isolated system, they are derived from solutions to Schrödinger equation. The radial solution gives functions of the form:

$$R(r) = e^{-r/na_0}\, r^l\, l_n, \qquad 3\text{-}29$$

where L_n are the Laguerre polynomials. These functions can be used somewhat directly in the form of Slater orbitals. Often, however, Gaussian orbitals are used to facilitate computation of integrals. As the product of a Gaussian is a Gaussian, four-center integrals reduce to just two-center integrals. These functions differ depending on the angular momentum channel. They are multiplied by the spherical harmonics, $Y_{l,ml}(\theta, \phi)$.

Plane waves

K-S wave functions can be represented as a linear combination of plane waves.

$$u_{n,k} = \sum_G u_{G,n,k}\, e^{iG.r} \ . \qquad 3\text{-}30$$

Plane wave method is advantageous as the form of the system does not bias them or limited to one type of atom. Additionally, fast Fourier transformation can be used to move between real space and k-space, making the computations much faster. As the plane waves do not depend on the position of the atoms, the Hellman Feynman theorem can be used to calculate the forces directly. The electrons in a system without ionic cores will have plane waves as their eigenfunctions. That is, plane waves are eigenfunctions of the homogeneous electron gas. Therefore, the real wavefunctions produced when including the effect of the cores should be somewhat similar to plane waves, as in the nearly free electron model. The difference is taken into account by building up the wave-function from many different plane waves using Fourier analysis.

Periodicity

Simulation of an isolated system which contains a few atoms is straightforward. However, often it is required to simulate a solid bulk material, which would require a great many atoms. However, this can be avoided by simulating a unit-cell of the solid and periodically repeating this in all three spatial dimensions. Surfaces can be simulated similarly, by leaving a vacuum gap in one of the dimensions.. As well as enabling the simulation of bulk solids and surfaces, periodic boundaries also have some computational benefits. When a periodic system is being treated, Bloch's theorem can be applied. This states that the eigenfunctions of the Schrödinger equation with a periodic potential can be written as:

$$\psi_{n,k} = u_{n,k} e^{ikr} \ , \qquad 3\text{-}31$$

where $u_{n,k}$ has the periodicity of the underlying lattice. These are the eigenfunctions of the wave equation with a periodic potential. The Bloch function $u_{n,k}$ is defined as having the period of the lattice. Therefore, like any periodic function, it can be expanded using a Fourier series of terms that are the reciprocal lattice vectors. For example, as a series of plane waves with wave-vectors G equal to the reciprocal lattice vectors of the periodic lattice.

$$u_{n,\boldsymbol{k}} = \sum_{G} u_{G,n,k}\, e^{iG.r} \ . \qquad 3\text{-}32$$

There are of course an infinite number of reciprocal lattice vectors defined by an infinite lattice. However, the higher frequency components of this plane-wave expansion for the Bloch function are less critical due to their higher curvature. Therefore, to a good approximation, the expansion can be truncated at a specific cut-off. Note, that this truncation is required and determined by the amount of processing power and memory available for the calculation. Thus only components with:

$$|K+G|^2 \frac{\hbar^2}{2m_e} < E_{cut}, \qquad 3\text{-}33$$

are included. Systems should be tested for convergence to ensure that the effects of the truncation are not affecting the conclusions drawn from the calculation. Putting the expansion for the periodic Bloch function into the Bloch theorem expression of equation 3-31 gives:

$$\psi_{n,\boldsymbol{k}} = \frac{1}{\omega} \sum_{G} u_{G,n,k}\, e^{iG.r}. \qquad 3\text{-}34$$

This expression is merely a linear combination of plane waves. The original wave-function which was spread over the infinite space of the periodic lattice has been transformed into a wave-function localized inside just one of the periodic cells. However, this wave-function must be calculated at an infinite number of k-points. This need can be circumvented by imposing Born von Karmen boundary conditions.

$$\psi(r + N_i a_i) = \psi(r). \qquad 3\text{-}35$$

Moreover, using Bloch's theorem, Equation 3-31:

$$\psi(r + N_i a_i) = e^{iN_i K_i . a_i} \psi(r). \quad 3\text{-}36$$

The only k-values for which this is true are those who give the argument of the exponential value of 2nπ.

$$K_i = \frac{integer}{N_i} g_i. \quad 3\text{-}37$$

Thus there are an infinite set of infinitely close together k-points if the number of cells N_i considered in the calculation is infinite. However, the energy is a smooth function of the wave-vector k, and the Bloch wave solutions are unique only up to a reciprocal lattice vector. Therefore they can be fully described using just their components in the first Brillouin zone, and the wave-function can be approximated by the average of its value at a finite number of k-points within this. Sometimes it is enough to take the average of the two equivalent Gamma points k = 0, and k = π. This transformation from real space into k-space is in effect numerical sampling and dramatically simplifies the plane-wave formalism. Care must be taken as k-point sampling is more complicated and essential when dealing with systems with highly curved Fermi-surfaces, such as a nearly metallic system, which will then require more k-points to sample accurately.

3.5.4 Pseudopotentials

Near an atomic nucleus, the Coulomb potential becomes extremely strong. To balance this, the kinetic energy of the wave-function must also become very large, and consequently, the wave-function oscillates a great many times and requires a considerable number of Fourier components to be accurately represented. This problem is avoided by using pseudo-potential. In most situations, the core electrons do not play an essential role in the bonding of an atom, as they are highly localized around the nucleus. Only the valence electrons are involved in bonding. It is, therefore, an excellent approximation to take the core electrons in any system to have the same distribution as they would in an isolated atom. That is, solutions of the radial Schrödinger equation multiplied by spherical harmonics. The interaction between the core electrons and the valence electrons is then approximated by what is known as pseudo-potential, rather than being treated explicitly. It is also possible to treat this interaction correctly using the projector augmented wave method, as discussed in the next section. However, first here, the pseudopotential approximation is discussed.

There are several advantages to the pseudopotential approach. First, it results in fewer electrons needing to be considered by the calculation and thus reduces the computational cost, as there are less Kohn-Sham eigenstates and therefore fewer matrix elements to compute. Another advantage is that the core electrons constitute a significant fraction of the total energy. This energy can now be used as the baseline in a calculation, and so the energy minimization can be sensitive to the far smaller energy changes of the valence electrons. The second advantage is that the creations of a pseudo-potential that has the same effect on the valence electron wave-functions away from the core but allows them to be smooth within the core region results in a dramatic reduction in the number of plane waves needed to represent those wave-functions.

The main drawback of using pseudopotential in contrast to an all-electron method is that it compromises the universality of the method. Pseudopotential must do its best to accurately reflect the interaction between core and valence electrons, in all the different possible environments into which an atom could be placed. In a bulk solid, as part of a molecule, when in a liquid and so forth. This is known as the transferability of the pseudopotential. In most cases, it is not perfect and should be checked. Transferability is particularly hard to achieve when an atom has many different possible charge states and therefore different possible numbers of bands. Often the correct charge state will depend on the coordination of the atom, which changes according to the environment. Titanium and manganese are notable examples of essential elements that pseudopotentials can have difficulty with.

There are various kinds of pseudopotential. Norm-conserving pseudo potentials ensure that the charge within the cut-off region is equal to the charge of the core electrons. This ensures that the core region of the atom is not significantly affected by the surrounding environment and so aids transferability. There are ultra-soft pseudopotentials, which result in smoother Kohn-Sham wave-functions and thus require fewer plane waves. Finally, there is a method known as the projector augmented wave (PAW) method which will be used in the studies in this thesis. This method is outlined next.

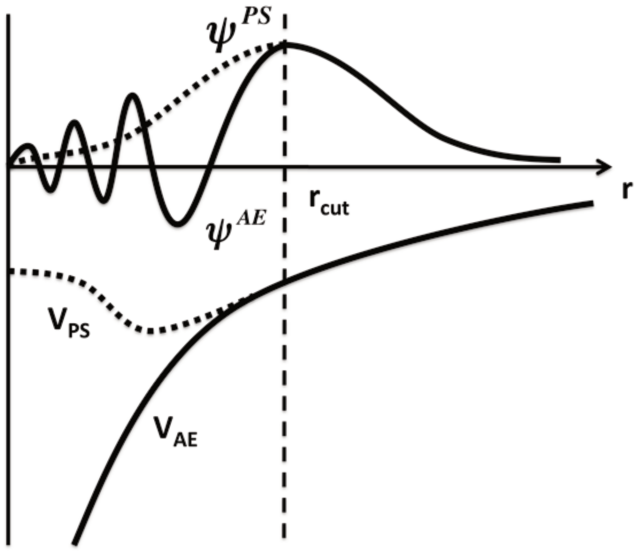

Figure 3-3 Schematics of the effect of pseuo-wavefunction [67]. ψ^{PS} and ψ^{AE} are the pseudo wavefunction and the all-electron wavefunction, respectively; V_{PS} and V_{AE} are the pseudopotential and all-electron potential respectively; and r_{cut} is the cut-off radius.

Projector augmented-wave method

The projector augmented wave method [68] is used in this thesis. An outline of the basics is given here, but as always the details of implementation are more complicated, see for example [69]. The advantages of both localized basis sets and plane wave implementations have been described. The PAW method, however, combines the advantages of both basis sets. The PAW method uses plane waves in the interstitial region between atoms and a localized basis close to the atoms. This means that the method has access to the full all-electron wave-function and consequently that it can be a more transferable method than a pure plane-wave implementation. As the PAW method contains all the electrons in the system, it has at least some variational freedom in the core region that enables it to produce more accurate results than a frozen core approximation. However, in order to keep the computational cost within limits and the conveniences of using single convergence (cut-off energy) parameter , using plane waves appears to be an efficient alternative. The PAW method also has the straightforward force calculation of the plane wave pseudopotential method.

In the PAW method a search is made for a smooth wave-function that is related to the exact all-electron wave-function via a linear transformation:

$$|\psi_n\rangle = \tau\ |\tilde{\psi}_n\rangle \qquad 3\text{-}38$$

Here, $|\psi_n\rangle$ is the fast oscillating all-electron wave-function that is hard to represent, while $|\tilde{\psi}_n\rangle$ is the smooth pseudo-wave-function that can be easily built using plane waves. A transformation is searched for such that:

$$\tau = 1 + \sum_R S_R, \tag{3-39}$$

where the function S_R is defined in non-overlapping spheres centered around the atoms, that is, the core region. Within this region, a partial-wave basis $|\phi_i^R\rangle$ is constructed from solutions of the Schrödinger equation for an isolated atom. For each of these functions, there is also a corresponding 'soft' partial wave $|\tilde{\phi}_i^R\rangle$. These are chosen to match at the edge of the region R. A form for the wave-function can be derived:

$$|\psi_n\rangle = |\tilde{\psi}_n\rangle + \sum_{R,i} \left[|\tilde{\phi}_i^R\rangle - |\phi_i^R\rangle \right] \langle \tilde{p}_i^R | \tilde{\Psi}_i^R \rangle, \tag{3-40}$$

which gives the linear transform as:

$$\tau = 1 + \sum_I \left[|\phi_I\rangle - |\tilde{\phi}_I\rangle \right] \langle \tilde{p}_I |, \tag{3-41}$$

where, I = (R, n, l, m). The transformation above is used to create a basis in which plane waves represent the wave-function between the atoms and local functions (projectors), derived from the plane waves, represent the wave-function close to the atoms. The PAW method currently provides one of the best mixes of transferable accuracy and speed in density functional calculations.

3.5.5 Periodic Boundary Conditions

This thesis applies DFT to the compute the properties of Na_2CO_3 surfaces. The system under study is assumed to be symmetrical and repeat itself infinitely in the x, y, and z directions. This assumption allows one to use a small computation cell to reduce the computational cost as atoms and electrons are repeated. An interface modeled using a periodic boundary condition is referred to as a supercell approach. The supercell approach treats the interface as a slab where the interface is extended infinitely in the XY-direction but consists of several atomic layers in the z-direction. The side and top view of the three-layer slab of the system under study - Na_2CO_3 (001) is shown in Figure 3-4. There are two main parameters to consider in order to obtain reliable computation results:

- The number of layers in the slab
- The thickness of the vacuum region; and

- The lateral size of the supercell

A sufficiently large number of layers should be included in the slab such that the atoms in the middle of the slab have the physical properties of the atoms in bulk. The required number of layers varies from one system to another; generally speaking three to seven layers are typically used. The supercell should include enough vacuum to avoid any artificial interactions with its periodic images along the z-direction. A typical vacuum thickness used in the supercell approach is around 15 Å to 20 Å.
To avoid an artificial interaction between the adsorbates the lateral size of the supercell (along with the XY-plane) shall be chosen sufficiently large. A comparison of the results using different lateral sizes is presented in Chapter 5.

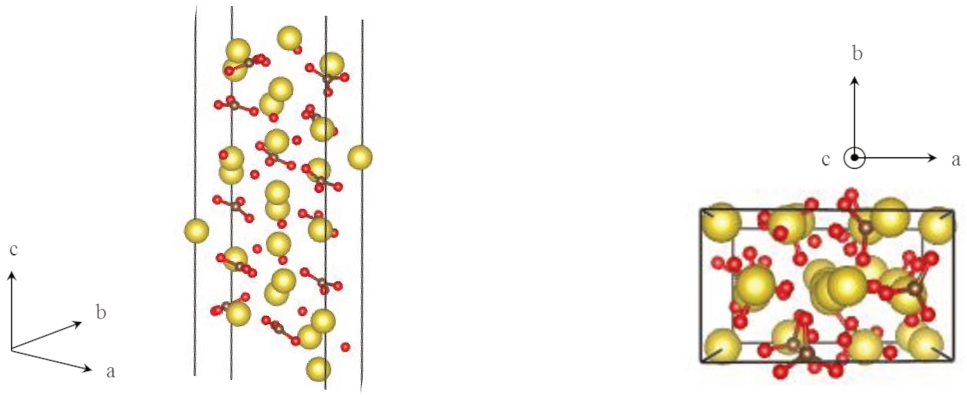

Figure 3-4 Illustration of the supercell approach for modeling a $Na_2CO_3(001)$ surface. The supercell consists of three layers of unit cells and vacuum. The periodic boundary conditions repeat the supercell infinitely in all three dimensions. *Yellow* Na; *red* O; *brown* C.

3.6 Computational details

In this study, the Vienna Ab-initio Simulation Package (VASP) [66], [70] was employed to perform calculations based on the DFT using pseudopotentials and planewave basis sets. The Perdew, Burke, and Ernzerhof (PBE) exchange-correlation functional and Projector Augmented-Wave (PAW) method were used [58], [68], [71]. The cut-off energy for the expansion of the planewave basis sets was optimized and set at 500 eV. To improve the description of the long-range interactions, the DFT-D3 method of Grimme as implemented in VASP was employed [72]. The Kohn-Sham equations were solved self-consistently until energy difference between cycles becomes lower than 10^{-4} eV. A Methfessel–Paxton smearing with $\sigma = 0.1$ eV was used [73]. The ionic positions have been optimized until all forces were smaller than 0.03 eVÅ^{-1} per atom. The k-point grids were set at 4×6×6

for the bulk simulations[10]. To model the surface, the depth of the slab has been chosen equivalent to three layers (three unit cells). Every unit cell (each layer) is containing eight atoms of Na, four atoms of C, and twelve atoms of O. Only the bottom layer was frozen. The vacuum spacing in the cleavage direction of repeated cells was 15 Å.

The specific surface energy, (eV.Å^{-2}), γ, was computed using the following expression:

$$\gamma = \frac{E_S - n \cdot E_b}{S}, \qquad 3\text{-}42$$

where, S is the active surface area, E_s is the energy of the slab, E_b is the energy of the bulk, and 'n' is the number of unit cells in the slab. According to Equation 3-42, the smaller the value of γ, the more stable the surface is.

3.7 Isotherm modeling- a literature review

The process of adsorption is usually studied with graphs known as adsorption isotherms which is a plot between the amounts of adsorbate (x) adsorbed on the surface of adsorbent (m), at a constant temperature. In this study, to study the performance of the adsorption of iodine on the sodium carbonate surfaces, we proceed to study the isotherm modeling in detail.

$$A + B \rightarrow AB$$

According to Le-Chatelier principle, the direction of equilibrium would shift in the direction where the stress can be relieved. In case of application of excess partial pressure of the adsorbate (gas), equilibrium is favored in the forward direction. As with all chemical equilibria, the position of equilibrium will depend on a number of factors, which include the following factors, such as

- The relative stabilities of the adsorbed gas phase species involved in the reaction
- The available surface
- The temperature of the system both gas and the surface, although, in standard circumstances, these are the same
- The pressure of the gas above the surface

[10] The same proportion with respect to lattice parameters has been kept for surfaces calculations. 4×6×1 for (001), 1×6×6 for (100), and so forth.

In general, the last two factors exert the opposite effects on the concentration of adsorbed species – that is to say, the surface coverage may be increased by raising the gas pressure but will reduce if the surface temperature is raised.
While considering the adsorption isotherm, it is conventional to adopt a definition of surface coverage (θ) which defines the ratio of sites occupied by the gas molecules and a total number of available sites on the surface. This quantity gives a relative estimation of the surface coverage. The maximum surface coverage (saturation) of a particular adsorbate on a given surface is $\theta_{max} = 1$. A brief review of two majorly used existing adsorption isotherm models is presented in this section. There are many other types of adsorption isotherms which differ from one another by the basic assumptions made in deriving the expression for the surface coverage; in particular how they treat the surface coverage dependence on the enthalpy of adsorption.

3.7.1 Langmuir adsorption model

The Langmuir adsorption is the simplest of all; it still provides useful insight into the pressure dependence of extent of the surface coverage. This isotherm is based on the assumptions that 1) dynamic equilibrium exists between adsorbed gaseous molecules and the free gas molecules 2) adsorption is of monolayer type 3) the adsorbed species do not interact with one another 4) all the adsorbent sites are equivalent. A relationship between the number of active sites on the surface and partial pressure of the gas was described as:

$$\theta = \frac{k^I P}{1 + k^I P} \qquad 3\text{-}43$$

where θ is the number of sites on the surface which are covered with the gas phase species, P is the pressure of the gas, and k^I the equilibrium constant. One of the limitations of this isotherm is that it is valid for small pressures only such that $(1+k^I P)$ in the denominator remains negligible.

3.7.2 Brunauer-Emmett-Teller adsorption isotherm theory

This adsorption isotherm explains that the multilayer adsorption is the accurate picture of the adsorption. It assumes that 1) the gas phase species adsorbs to the solid surface in layers and there is no interaction between each layer such that the Langmuir theory can be applied to each layer 2) After a certain point, the energy of adsorption remains the same for all the adsorbing molecules. Under the condition of high pressure and low temperature, thermal energy of the gas species decreases resulting in higher number of gas molecules available per unit surface area. Due to these phenomena, multilayer adsorption would take place. The BET equation reads:

$$\frac{P}{V_{total}(P-P_0)} = \frac{1}{V_{mono}C} + \frac{C-1}{V_{mono}C}\left(\frac{P}{P_0}\right), \qquad 3\text{-}44$$

where V_{mono} is the adsorbed volume of the gas at high pressure condition which is sufficient to cover the active sites with one layer of molecules.

3.7.3 Types of adsorption isotherms

Physical adsorption can broadly be classified into six groups, as presented in Figure 3-5. A brief description of each type is given below.

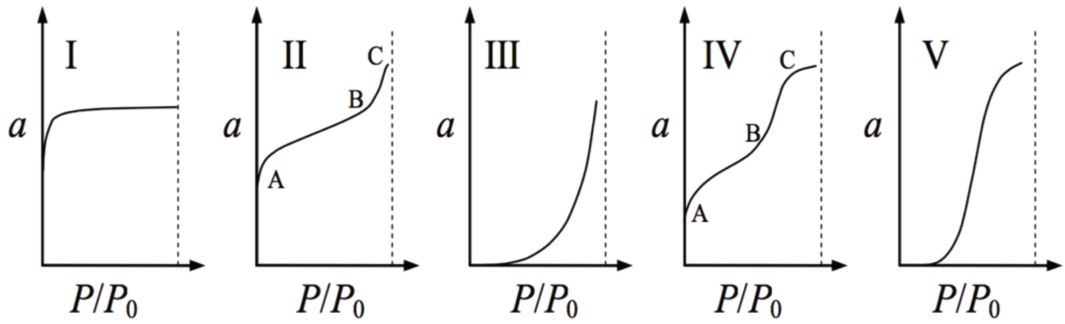

Figure 3-5 The IUPAC classification of Adsorption isotherms for gas-solid equilibria [74], [75].

Type I: This type of isotherm is often called as single-molecule (or single layer) isotherm. This type can be explained using Langmuir isotherm theory, as explained in the previous section. They are characterized by a horizontal plateau, i.e., after a particular pressure, the mass of the adsorbed molecules stall, independent of the increased pressure. These isotherms are a characteristic of microporous material, where the capillaries are filled but multilayer adsorption is not feasible. The core of this theory is that there is absolutely no interaction between the species adsorbed at the surface.

Type II: This type of isotherm is specific to non-porous or macro-porous sorbent. It illustrates unrestricted, monolayer-multilayer adsorption. The first half of the curve (almost plateau) shows a somewhat slow increase; this increase signifies monolayer adsorption. However, the second half shows a sharp increase, characterizing multilayer adsorption in addition to the filling and condensation of the gas molecule in the pores of the sorbent. In can be seen that in this case, saturation point is absent. It implies that there is no limitation on the mass adsorbed within the

condition that the adsorption temperature is lower than the critical temperature of the adsorbate.

Type III: As it can be seen from the figure that this isotherm shows considerable deviation from the Langmuir model. There is an absence of a flat region, which indicates the absence of monolayer adsorption. In this case, the adsorbent surface-adsorbate interaction is strikingly lower than the lateral interaction between the adsorbed molecules. This case is specific to strongly associated molecules.

Type IV: At lower pressure, this isotherm is similar to type II adsorption isotherm. The adsorption process initiates by generating a monolayer and furthermore a multilayer. Moving on, after pressure attains a threshold value, the region BC in the figure represents the capillary condensation of molecules in meso-pores which limits the adsorption over a range of high pressure and the hysteresis behavior.

Type V: This isotherm is derived from type IV. It shows the weak interaction between adsorbate-adsorbent at the surface. However, with an increase in relative pressure of the gas, the mass of the adsorbed molecules increases, but the increase is slow implying that the pores in the adsorbent are restricted in number.

Isotherm modeling of the interactions between Na_2CO_3 and I_2 was performed using experimental data and theoretical chemistry modeling. The shape of the isotherm was then compared with the types of isotherms explained above, and their interpretation is presented in Chapter 5 and Chapter 6.

Chapter 4 Experimental methods and tools

This chapter presents the experimental processes that were designed and executed in the laboratory to study the heterogeneous reaction between Na_2CO_3 (s) sorbent surface and I_2 (g). The main challenge in performing the experiments were to be as representative as possible as to the in-containment SA conditions (discussed in Chapter 2). This implies in particular to work with low I_2 (g) concentrations. Otherwise speaking, high Na_2CO_3 (s) to I_2 (g) ratios.

4.1 Experimental methods

The major components of the experimental investigations are listed below.

- Preparation of reacting Na_2CO_3 (s) surfaces, their physical and chemical characterization.
- Gaseous molecular iodine generation and detection.
- Quantification of I_2 (g) uptake on Na_2CO_3 (s) surfaces and associated kinetics.

First, different methods of preparing and treating the reacting surfaces are discussed in Section 4.2. The next section gives an overview of the surface characterization methods used in this work. Section 4.4. and the following sections describe the method and principles for I_2 (g) generation and detection. Finally, the two distinct techniques and facilities used to quantify I_2 (g) uptake on sodium carbonates are discussed in Section 4.7 and 4.8.

4.2 Preparation of sorbent surfaces

In case of a SA, sodium to iodine molar ratio ranges from 1000 to 4500[11] [76]. Keeping in consideration this fact, the amount of Na_2CO_3 sorbent, in our experimental

[11] The ratio highly depends on the SA sequence.

investigations had to be adjusted. However, the concentration of generated Na_2CO_3 is a function of the extent of sodium leak and the rate limiting factors (such as CO_2 concentrations, etc.) [7]. It is then safe to assume that Na_2CO_3/I_2 ratios will be extremely higher than 4500. To be representative of realistic SA conditions, we proceed with a wide range of the mass of Na_2CO_3 sorbent. To do so, the mass of the sorbent was kept between 0.035 and 8 g (Na_2CO_3/I_2 ratio of the order 10^{20}).

As a first step to understand the physical properties and hence the reactivity of Na_2CO_3 surfaces towards I_2 (g), we start our experimental investigation using pure Na_2CO_3 powder (Sigma-Aldrich, purity = 99.5%). The preparation of the sorbent was carried out in two different fashions; a) aerosol deposition from aqueous solution of Na_2CO_3 powder and b) using pure Na_2CO_3 powder without any further preparation.

4.2.1 Aerosol deposition from aqueous solution of pure Na_2CO_3 powder

For this approach, the generation of Na_2CO_3 aerosols was done by preparing an aqueous solution of Na_2CO_3 powder in deionized, ultra-pure water by atomization technique. The aerosol generator PALAS-AGK2000 was used to generate Na_2CO_3 aerosol deposit.

In this technique, the liquid (here, aqueous solution of Na_2CO_3 powder, 0.15 M) to be dispersed is filled in a reservoir. A nozzle system is immersed in the liquid, see Figure 4-1. This nozzle system is based on the Laskin principle [77]. According to this principle, compressed air is fed down a supply tube to radial holes. Just above these holes a ring is secured with adjacent holes above the air. The nozzle arrangement is immersed in the fluid to be nebulized. As the compressed air flows at high velocity out of the radial holes, it effectively atomized and small air bubbles are created, which then grow and move to the surface of the liquid where they burst and release the generated particles they contain into the air. The mass flow is adjusted using the volume flow through the nozzle. The volume flow is controlled by a pressure regulator and a manometer on the device. The size of generated Na_2CO_3 particles is a function of the concentration of the aqueous solution. The particle size spectrum can thus be adjusted reproducibly in the range from about 5 nm up to 15 µm, depending on the concentration of Na_2CO_3 in the solution and on the carrier gas flow. This size of aerosols is representative of SA conditions in SFR. The two parameters (molarity of the aqueous solution and the gas flow) were set to get a typical mass of deposits of Na_2CO_3 on a glass plate to be between 3 and 8 mg.

The outlet, after the aerosol deposition was connected to bubblers filled with NaOH solution to trap minute aerosol particles, as they can be hazardous, if inhaled. The

experimental setup for aerosol generation is shown in Figure 4-1. The resultant deposit is shown in
Figure 4-2

Figure 4-1 Aerosol deposition device PALAS AGK-2000 (left); and the experimental setup (right).

A glass surface has been chosen for aerosol deposit as it is known to be inert with I_2 (g). After the aerosol deposit, the glass plates were removed from the apparatus and stored in an inert controlled environment. Before the experiments, the aerosol plates were heated at 150°C for several hours to make sure that the organic compound or humidity are removed from the reacting aerosol surfaces.

4.2.2 Pure Na_2CO_3 powder

Pure Na_2CO_3 powder was used to prepare the reacting surfaces for a second set of experiments. Two ways of using the powder are explained in this section.

- A couple of experiments were performed with the sorbent in a rupture tube. A rupture tube is a 5 cm long tube of diameter slightly less than the FTR and made of glass fiber. The rupture tube is placed along the horizontal axis of the FTR. The motivation behind using a rupture tube is to 'force' iodine to pass through all the grains of the powdered sorbent.

Furthermore, another way of exposing sorbent powder to iodine flux involved manually putting a few grams of the powder was homogeneously across the length in glass/Teflon cells, shown in

Figure 4-2. The dimensions of the cell were length, L ≈ 5 cm; width, W ≈ 1cm.

The powder was first mechanically crushed and then pellets of about 200 mg were made by compressing the powder. The diameter of one pellet is about 1 cm (see Figure 4-2).

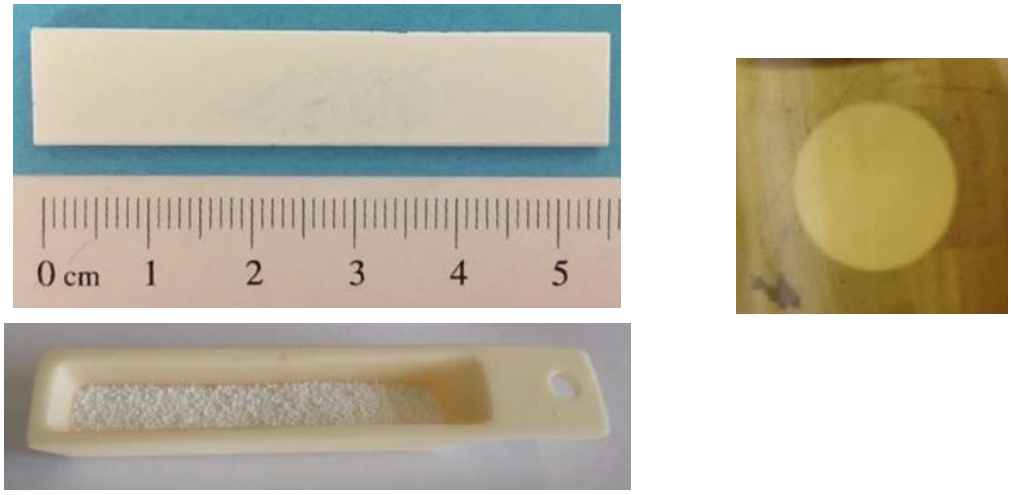

Figure 4-2 Na_2CO_3 reacting surfaces. Top left: aerosol deposit on a glass plate; top right: pellet; bottom: powder in a Teflon cell.

4.3 Surface characterization

The important question in uptake and kinetic studies is how the sorbent surface (chemistry, structure, and morphology) influences the response of the adsorbate. As key interactions (chemical and electrostatic) between the adsorbent and the adsorbate generally occur at the surface, a better knowledge of the sorbent surface structure is crucial. A complete characterization of the surface requires the use of many techniques to compile all the information needed. In this work, we performed the following surface characterization techniques a) surface morphologies were investigated with scanning electron microscopy (SEM) b) surface area measurements were performed using Brunauer–Emmett–Teller (BET) analysis technique, and c) the chemical compositions of the different surfaces were investigated with time-of-flight secondary ion mass spectrometry (ToF-SIMS).

4.3.1 Particle size determination by Scanning Electron Microscopy

Scanning electron microscopy (SEM) is widely used and well documented in the literature[78][79]. The principle of SEM is the focusing and rastering of a relatively high-energy primary electron beam (typically 5 to 35 kV) on a sample. Secondary electrons (SE), backscattered electrons (BSE) and X-rays are emitted from the surface and are collected by suitable detectors for evaluation. SE signals have a very low energy in the range of 8 eV, which corresponds to an attenuation length of 5 to 10 nm. The minimum lateral resolution of a SE image will be in the same range. BSE have energies of the order of the primary electron energy. Therefore, an attenuation length of 100 to 1000 nm will be expected, depending on the sample and the energy of the primary electron beam. The primary electron beam also results in the emission of X-rays. These element-characteristic X-rays are used to identify elements with the technique called energy-dispersive X-ray (EDX) analysis. SEM has some advantages, such as the large depth of focus, the high lateral resolution down to the nm range, the feasibility to study structures with high aspect ratio, and direct production of images of the surfaces. SEM images easily give a three dimensional impression of the surface. However, quantitative information about the morpholophy could not be obtained from a single micrograph.

Instrument and sample preparation

A JEOL 7600F High Resolution Analytical SEM was used on the aerosols deposits, pellets, and powdered surfaces. To remove the traces of humidity and volatile compounds from the surfaces the samples were heated at 150°C for one hour.

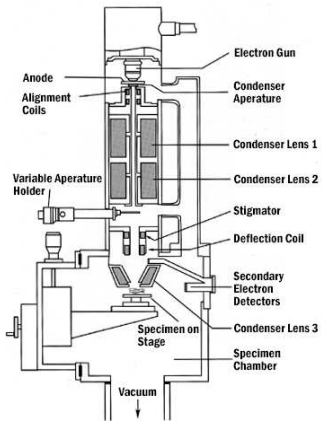

Figure 4-3 A view of the SEM, University of Lille.

4.3.2 Specific surface area by Brunauer-Emmett-Teller measurements

Nitrogen adsorption is one of the main experimental techniques to determine the specific surface area of powders and porous materials [80], [81]. Using Brunauer–Emmett–Teller (BET) theory, nitrogen adsorption isotherms is used for determining the specific surface area of solid surfaces [82]. BET surface area measurements and their analyses were performed using a Mono-point BET micromeritics flowSorb III surface area analyzer. The calibration of the instrument was carried out by using nitrogen gas.

Instrument and principle

The specific surface area of the powdered sample is determined by physical adsorption of N_2 gas on the surface of the Na_2CO_3 sorbents and by calculating the amount of adsorbate gas corresponding to a monomolecular layer on the surface. Physical adsorption results from relatively weak forces (van der Waals forces) between the adsorbate gas molecules and the adsorbent surface area of the powder. The determination of the specific surface is usually carried out at the temperature of liquid nitrogen. The amount of gas adsorbed can be then measured by a volumetric or continuous flow procedure.

Sample preparation

Before the specific surface area of the sample can be determined, it is necessary to remove gases and vapors that may have become physically adsorbed onto the surface after manufacture and during treatment, handling, and storage. If outgassing is not achieved, the specific surface area may be reduced or may be variable because an intermediate area of the surface is covered with molecules of the previously adsorbed gases or vapors. The outgassing conditions are critical for obtaining the required precision and accuracy of specific surface area measurements because of the sensitivity of the surface of the materials. In our measurements, the sample Na_2CO_3 sorbent was heated up to 150°C to remove any traces of humidity or volatile organics from the surface.

4.3.3 Analysis of chemical composition of the surfaces by ToF-SIMS

Secondary ion mass spectrometry (SIMS) is the mass spectrometry of atomic or molecular species, which are emitted when a surface is bombarded by energetic

primary particles, usually ions. The secondary ions, which are detected, may be emitted from the surface in the ionized state or they may be initially emitted as uncharged species to be post-ionized before analysis. In the case of dynamic SIMS, a high flux of primary ions is directed at the material surface. The surface is eroded very rapidly and it is possible by monitoring elemental composition changes with depth to get elemental depth profile. In the static mode, secondary ions are emitted from areas not previously damaged and the surface monolayer lifetime is well in excess compared to the time required for analysis. The importance of static SIMS for surface analysis arises from the fact that a surface mass spectrum is generated and thus the chemical structure characterization is available. By raster scanning the beam across a surface area and collecting the secondary ions at each point a chemical image of the surface can be generated. This variant of the technique is known as imaging SIMS. ToF-SIMS allows monolayer analysis with high sensitivity, a wide mass range, high mass resolution, and high lateral resolution. A time resolution of 1.25 ns per step was used for good signal-to-noise ratio at high m/z[12] range. The pressure of the main chamber was kept between 10^{-8} and 10^{-10} Torr for each analysis. Each specimen was analysed a minimum of three times for checking the results reproducibility. The samples were prepared by compressing the Na_2CO_3 powder to make pellets. The analyses were restricted to surface spectroscopy only, without surface imaging and depth profiles. Indeed those latter analyses would have required a higher primary ion doses, potentially damaging the surface links.

4.4 Gaseous molecular iodine generation

In order to generate iodine vapors, solid iodine crystal were heated at a constant temperature. In all our experiments permeation tube primarily filled with molecular iodine crystals and located in an oven were used. Keeping the temperature constant for the duration of the experiment facilitated a constant flow rate (moles min^{-1}) of iodine vapors with respect to time. However, the flow rate (hence, partial pressure) of gaseous molecular iodine was varied in our experiments to study its impact on the kinetics of molecular iodine adsorption on sodium carbonate surfaces. This was achieved by changing two parameters: a) the temperature at which iodine crystals are heated and b) the flow rate of the carrier gas.

Iodine being vaporized at atmospheric pressure at relatively low temperature is extremely volatile and produces iodine vapors. One of the main challenges will then, in the facilities used for measuring its adsorption on sodium carbonates

[12] Mass to charge ratio.

surfaces, to avoid any cold points that would lead to gaseous molecular iodine losses by condensation.

Figure 4-4 shows the phase diagram of iodine where BO, OC, and AO are respectively the sublimation, vaporization, and the fusion curves. The triple point is 114.1°C and 0.12 atmospheric pressure, while the melting and ebullition point at atmospheric pressure is respectively 113.8°C and 130°C. The most notable feature of iodine's phase diagram is the small (less than a degree) difference between the triple and the melting point. In our experiments, performed at ambient pressure, the range of temperatures chosen to generate iodine vapors at different partial pressures was set between 70°C and 130°C. The temperature of permeation tubes was never exceeded to 130°C to ensure their integrity.

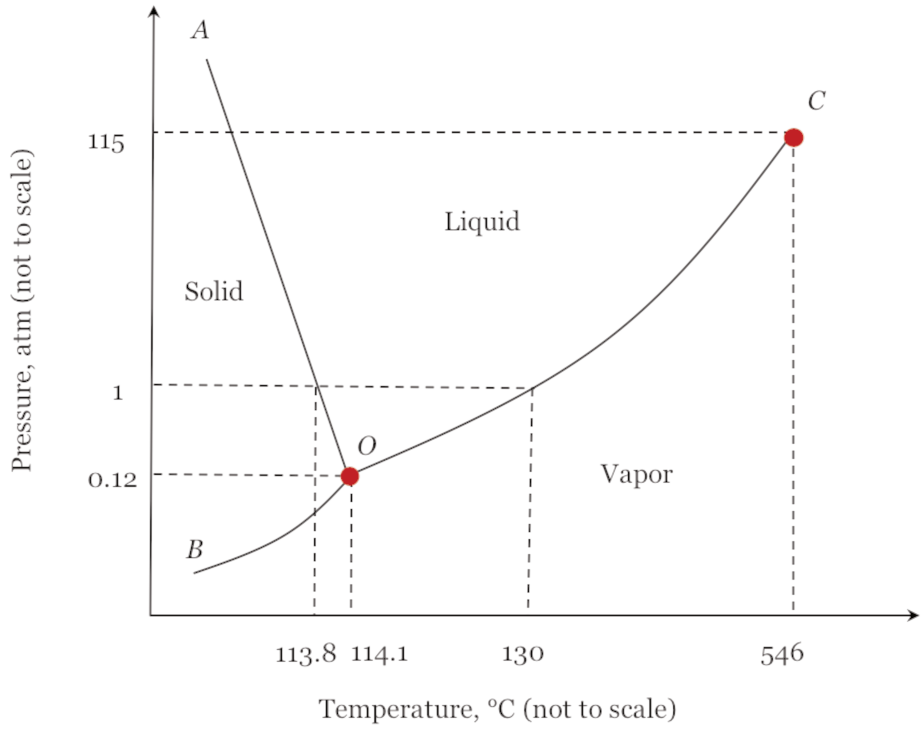

Figure 4-4 The phase diagram of iodine [83].

To quantify the concentration of I_2 flowing through the gas phase, two distinct techniques have been used:

- UV spectrometry
- Incoherent Broad-Band Cavity Enhanced Absorption Spectroscopy (IBBCEAS).

Both the techniques are explained in the next section.

4.5 Iodine detection by UV-visible spectrometer

Quantification of I_2 concentration was performed by bubbling I_2 gaseous mixtures through a 0.1 M KI aqueous solution. The I_2 trapping in the bubbler is based on the reaction between I^- and I_2 (aq), forming I_3^-. This reaction, R 4-1 , is rapid, meaning that, providing that the KI concentration is high enough, the conversion of I_2 to I_3^- is very efficient and the equilibrium is pushed virtually entirely towards the I_3^- side [84]. In our experiments, to verify the high efficiency of the bubbling system in trapping I_2 (g), a second bubbler was installed downstream the first one. The I_3^- concentration in the second bubbler was always found to be too low to provide a measurable signal, thus corroborating the high I_2 trapping efficiency of the first bubbler.

$$KI\ (l) + I_2\ (g) \rightarrow K^+(l) + I_3^-\ (l) \qquad \text{R 4-1}$$

The I_3^- concentration was then quantified by UV-visible spectrometry measuring the cross absorption spectrum as a function of wavelength.
The UV-vis spectrum of triiodide ions is shown in Figure 4-5. The spectra can be measured by scanning the aqueous solution of potassium iodide with iodine. The maximum absorption wavelength is reported to be 350 nm and 297 nm for triiodide ion.

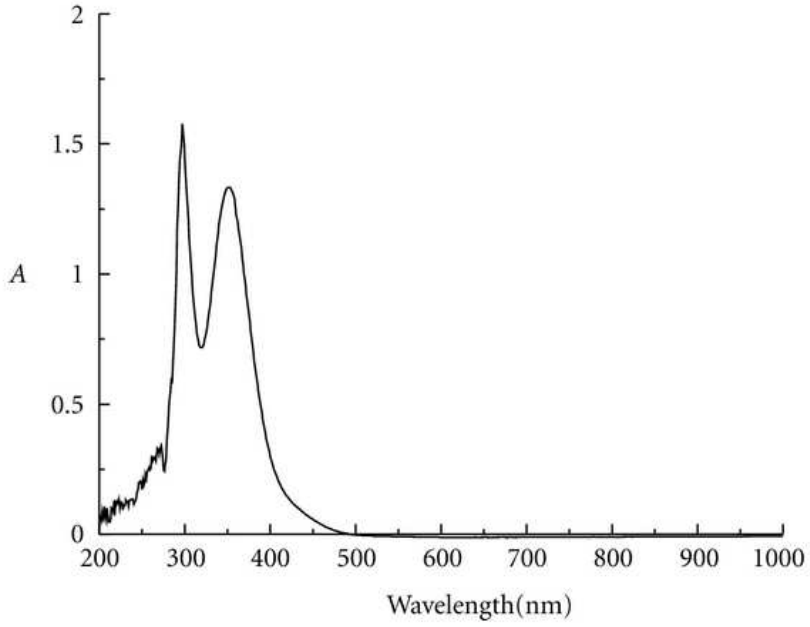

Figure 4-5: UV-visible absorption spectra of triiodide ions. Two peaks separated by 53 nm are reported in the literature [85].

The molar concentration of iodine was then calculated using the Beer-Lambert law that defines the relationship between the concentration of a solution and the amount of light absorbed by the solution as:

$$C = \frac{A}{\epsilon \times d}, \qquad 4\text{-}2$$

where, A: UV absorbance
ε: molar absorptivity at a specific wavelength (for I_3^- at 381 nm, $\varepsilon = 1.53\times10^4$ l $mole^{-1}$ cm^{-1})
d: path length of the cell containing the sample (1 cm)
C: I_3^- concentration (mole l^{-1}).

Detection limit: The minimum detectable absorbance limit of the instrument used (Agilent 8453) is 0.001 which equates to 3.98×10^{-8} moles l^{-1}.

4.6 Measurements of I_2 (g) by IBBCEAS

IBBCEAS (Incoherent Broad-Band Cavity-Enhanced Absorption Spectroscopy) is a spectroscopic technique to measure and quantify trace gases (I_2, in our case) in a closed volume with high selectivity and sensitivity. Important practical advantages of IBBCEAS are:

- On line measurements, implying that there is no need to trap or sample iodine.
- High temporal resolution compared to UV-visible spectrometry (1 measurement per 30 sec vs 1 measurement **per 10 min for UV-visible spectrometer).**

Principle of IBBCEAS device

The IBBCEAS method is based on the measurements of the interactions of I_2 molecules and an incoherent light generated from a green LED source (490-555 nm spectral range) and transmitted through a high-finesse optical cavity equipped with high reflective mirrors. Since the mirror reflectivity R is usually very close to one in most IBBCEAS applications, the optical extinction coefficient $\alpha(\lambda)$ due to the considered sample absorption (here I_2 in cm^{-1}) present inside the cavity can be approximated by [86], as presented below.

$$\alpha(\lambda) \approx \frac{1-R(\lambda)}{d}\left(\frac{I_0(\lambda)}{I(\lambda)} - 1\right), \quad \text{4-3}$$

where:

d: effective single-pass extinction path length, cm
R: mirror reflectivity
I_0: intensity of the transmitted light recorded with only the sample carrier gas inside the cavity
I: intensity of the transmitted light recorded with sample gas inside the cavity, both being a function of the studied samples, here molecular iodine.

In order to determine absorbance directly from equation 4-3, we need to measure the cavity mirror reflectivity spectrum (λ) and the effective path length d. That is why, using this technique a more reliable and alternative method consists in calibration measurements using a reference spectrum from a sample of known concentration. Using this calibration method does not require any more reference absorption cross-section which is convenient in our case since the iodine absorption cross-sections are unknown at 100°C & 150°C (as explained in Section 4.4). Therefore, based on this technique only relative data can be retrieved that provide the ratio between the sampling and calibration iodine density (n_{I2}) which reads:

$$n_{rel} = \frac{n_{I_2,sampling}}{n_{I_2,calib}} \quad \text{4-4}$$

One of the biggest strengths of using IBBCEAS technique compared to FTR coupled with UV-spectrometer is that it is an on-line measurement fitted with a very high temporal resolution (one measurement per 30 seconds) which is beneficial when studying the uptake kinetics of I_2 by sodium carbonates.

Moreover due to the cavity enhanced nature of the technique high stability and sensitivity can be achieved (around 26 pptv of I_2 for 1 min acquisition time) for the measurements enabling spectra to be taken at short integration times [87].

Some drawbacks exist with a dependence of:

- The sensitivity on the light source stability
- The measurement accuracy on the transmitted intensity.

The technique then requires a reliable calibration procedure to determine baseline optical losses of the system performing by introducing a known concentration of the absorbing species of interest into the cell.

IBBCEAS has been successfully used to measure I_2 trace gas [88]. It was especially shown that a light of around 530 nm wavelength excites several rovibronic lines of the B←X electronic transition of the molecular iodine. The I_2 visible and near – infrared spectrum has then been well characterized in the past [89].

Two different kinds of facilities were used to measure the iodine uptake kinetics by sodium carbonates:

- Flow tube reactor (FTR) specifically designed and built during this work where only discrete measurements of iodine can be performed. The FTR was in turn connected to the UV-visible spectrometer for I_2 detection and quantification.
- An optical cell where the heterogeneous reaction was studied. This cell was a part of the IBBCEAS facility. This iodine detection method provided on-line measurements of the gas phase I_2.

4.7 Quantification of the I_2 (g) uptake by Na_2CO_3 - FTR

A FTR was designed complying with a set of criteria that were built in order to be as representative as possible to conditions expected in a SFR containment experiencing a SA. The designing criteria of the FTR are discussed in Section 4.7.2. The design criteria included several factors like residence time of iodine inside the FTR, Reynold's number, etc.

4.7.1 Experimental setup

A schematic of the experimental setup used to study the kinetics of the heterogeneous reaction between Na_2CO_3 (s) and I_2 (g) is shown in Figure 4-11.

Figure 4-11In this apparatus, inert gas (Ar or N_2) was flowed into the first oven at controlled temperatures ranging from 70°C to 130°C where iodine permeation tubes were placed. The heated perfluoroalkoxy (PFA) tube transported this mixture of carrier gas and I_2(g) into a second oven (temperature controlled from 100°C to 150°C, with a precision of 1°C) where the FTR was placed. After passing through the FTR, either empty or containing the sorbent, the gas mixture was bubbled through a 0.1 M KI scrubber solution. Discrete sequential samplings of the solution are then performed for I_2 concentration measurements by UV-spectrometry. The dimensions and the shape of the main components of the experimental setup, the FTR and the gas bubblers are shown in Figure 4-6.

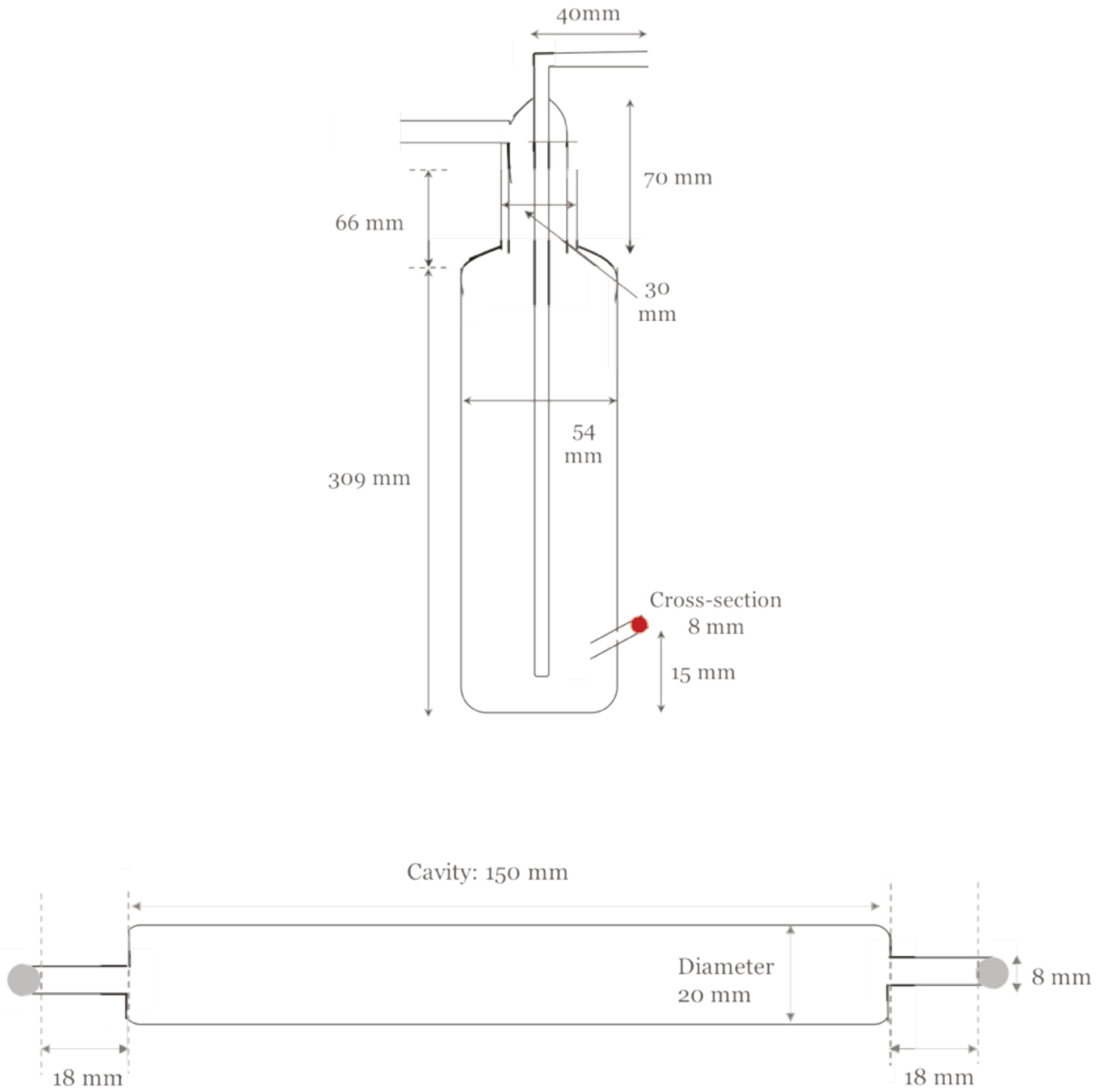

Figure 4-6 A schematic diagram of the gas-trap bubbler (top), and the FTR (bottom). Both the materials are made of glass.

4.7.2 Designing the Flow Tube Reactor

The FTR is a cylindrical hollow tube made of glass with a provision of both the ends to be connected to PFA tubes carrying gas phase species and operating at atmospheric pressure. It was designed and constructed to investigate the uptake of I_2 by Na_2CO_3 sorbent in conditions as representative as possible to the boundary conditions of a SFR containment following a SA. The required criteria to design the FTR relied then both on thermal-hydraulics and chemistry with:

- Gas temperatures ranging from 100 to 150°C
- High residence time (i.e., low flow velocities)

Experimental methods and tools

- Low molecular iodine concentration (the lowest acceptable concentration being fixed by the UV spectrometer detection limit): $< 10^{-6}$ M; I_2/Na_2CO_3 molar ratio (1000-4500).

The residence times and molecular iodine concentrations were adjusted by:

- The permeation tube temperature
- Argon/nitrogen mass flow rate

However the limited range of operating temperatures for the permeation tube (i.e., the limited range of generated I_2 partial pressures) strongly determined the range for carrier gas flow rates also. In the experiments two different flow rates for the carrier gas was used: 0.4 and 1Nl min^{-1}

4.7.3 FTR thermal-hydraulic conditions

The thermal-hydraulic conditions in the FTR were calculated for the two different argon gas flow rates and temperatures used in our experiments (Table 4-1). Reynold's number was calculated using Equation 4-5.

$$R_e = \frac{\rho v L}{\mu}, \qquad 4\text{-}5$$

where,

ρ: fluid density ($g.cm^3$)

v: fluid velocity ($cm.s^{-1}$)

L: FTR characteristic linear dimension, i.e., FTR diameter (20 mm)

μ: fluid dynamic viscosity. In our study, the values of the parameters discussed in the equation above are listed below.

Table 4-1 Residence times and gas velocities inside the FTR.

Ar flow rate, Nl min^{-1}	FTR temperature, °C	Flow velocity, ms^{-1}	R_e	Residence time, s
0.4	100	0.029	27.3	5.2
	150	0.033	26.7	4.6
1.0	100	0.072	34.1	2.1
	150	0.082	33.3	1.8

For all experimental conditions, the Reynolds number remained low implying the flow regime is laminar. This ensures that the gas velocities near the FTR walls will be negligible, thus inducing negligible friction factor and associated pressure drop in the FTR.

4.7.4 I_2 concentration inside the FTR

The I_2 concentration inside the FTR depends both on the permeation tube temperature and the carrier gas flow rate. They have been measured during the calibration tests from which the evolution of concentration of I_2 can be calculated. Since only accumulated concentration is measured by UV-vis spectrometry, the concentration is a linear function of time. The solid line in Figure 4-7 is a linear fit of the data points. The slope of the fit (4.2×10^{-9}, in the figure) gives the rate of change (moles min^{-1}) of the concentration.

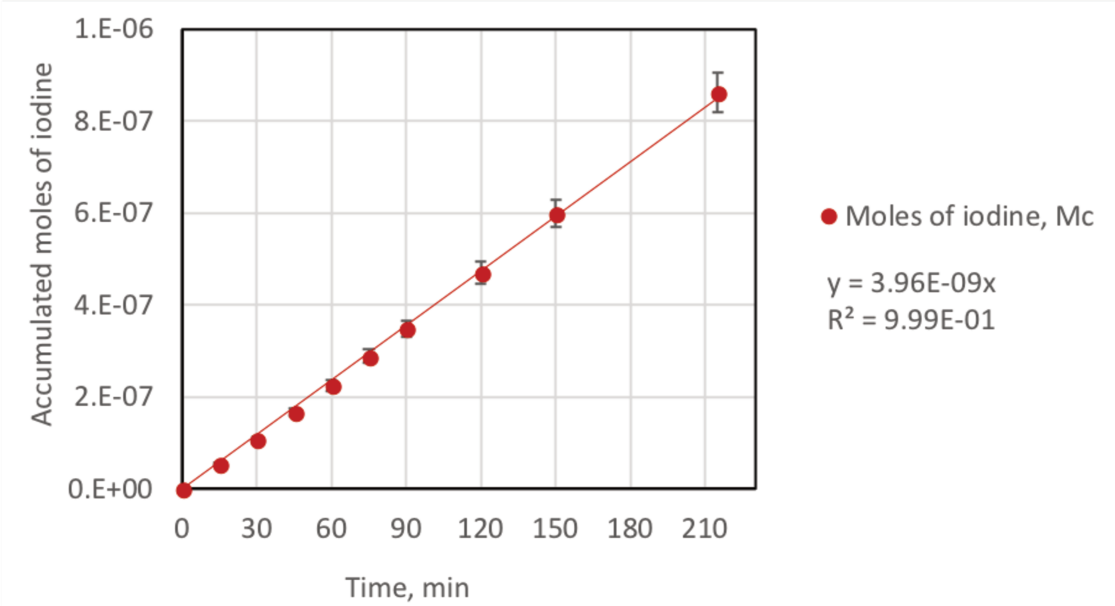

Figure 4-7 Evolution of moles of I_2 generated at 100°C and for 0.4 Nl min^{-1} argon flow rate.

Gaseous iodine inside the FTR: Calibration tests

The experimental protocol and measurement principle are explained in Section 4.7. The results obtained from the calibration tests where molecular iodine vapors was generated from solid iodine crystals in the permeation tubes then flowed through the FTR are summarized in this section. The results show the evolution of molecular iodine mole number accumulated inside the gas bubbler, plotted against time. The linear behavior of this plot allows checking that the molecular gaseous iodine generation is constant with respect to time. Estimated standard errors of the slopes of the fitted lines (for calibration tests) were 0.8%. The total error in measured I_2 flow rate during the calibration tests is thus estimated to be around 2% with the error being dominated by uncertainties in the molar absorptivity. Carrying out iodine measurements on accumulated liquid samples allows measurements to be performed on significantly higher concentrations with higher signal-to-noise ratios than had calibration been performed in gas phase.

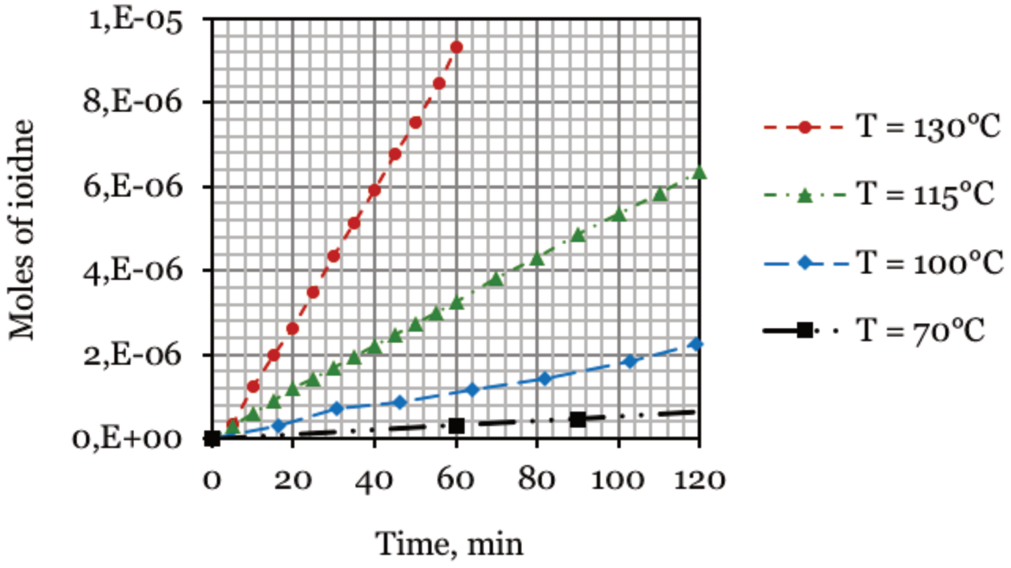

Figure 4-8 Evolution of the moles of I_2 accumulated inside the gas trap bubblers. I_2 generation at 130°C, 115°C, 100°C, and 70°C. Ar flow rate at 0.4 NL min^{-1}.

Calculation of partial pressure of iodine inside the FTR

Using the ideal gas equation which is written as:

$$PV = nRT,$$

where P, V, and T are the pressure, volume, and absolute temperature, respectively; n is the number of moles of gas; and R is the ideal gas constant.
Inside the FTR (which works at atmospheric pressure, 1.01325 bar), using the ideal gas equation:

$$P_{I_2}V = n_{I_2}RT \quad (4\text{-}6)$$

$$P_{N_2}V = n_{N_2}RT \quad (4\text{-}7)$$

$$P_{I_2} + P_{N_2} = 1.01325\ bar \quad (4\text{-}8)$$

Using Equation 4-6 and 4-7

$$\frac{P_{I_2}}{P_{N_2}} = \frac{n_{I_2}}{n_{N_2}} \quad (4\text{-}9)$$

Using Equation 4-8

$$P_{I_2} = \frac{n_{I_2}}{n_{N_2}}(1.01325 - P_{N_2}) \quad (4\text{-}10)$$

Here, P_{N_2} can be neglected as it is very small compared to unity.

Hence,

$$P_{I_2} = \frac{n_{I_2}}{n_{N_2}} (1.01325) \quad \text{4-11}$$

Calculation of n_{I_2} and n_{N_2}

n_{N_2} can be defined as the molar flow rate of N_2 (mol min^{-1}), such that:

$$n_{N_2} = \frac{\text{mass flow rate of } N_2 \text{ (g min}^{-1})}{\text{molar mass of } N_2 \text{ (g mol}^{-1})} \quad \text{4-12}$$

Moreover, mass flow rate of N_2 (g min^{-1}) is the product of volumetric flow rate and density of N_2 at finite temperature.

Volumetric flow rate of carrier gas is a quantity controlled and set at a finite value during the course of the experiment; the rest of the quantities are known in the literature. At 100°C, and 0.4 Nl min^{-1}, Equation 4-12 gives n_{N_2}=1.79 mol min^{-1}.

n_{I_2} is the molar flow rate of iodine which is measured by the calibration test. The slope of the dataset plotted between moles of iodine and time gives the value of n_{I_2} at a finite temperature.

As already mentioned the partial pressure of iodine inside the FTR can be varied by controlling two parameters a) the temperature of permeation tubes and b) the carrier gas flow rate. Such that the partial pressure is a function of two variables.

$$P(I_2) = f\ (T_{I_2}, Q_{Ar})$$

Both the parameters were changed and the resultant I_2 partial pressure was calculated, (Figure 4-9).

As shown on figure 6.5, as expected the generated I_2 concentration increases with permeation tube temperature increase and with carrier gas flow rate decrease.

Table 4-2 Relationship between temperature of iodine permeation tubes and iodine partial pressure vapors for two different flow rates of carrier gas.

Temperature of generation, °C	I_2 partial pressure, bar	
	Q_{N_2} = 0.4 NL min^{-1}	Q_{N_2} = 1.0 NL min^{-1}
70	3.7×10^{-07}	1.5×10^{-07}
100	1.1×10^{-06}	4.2×10^{-07}
115	3.0×10^{-06}	1.2×10^{-06}
130	8.4×10^{-06}	3.4×10^{-06}

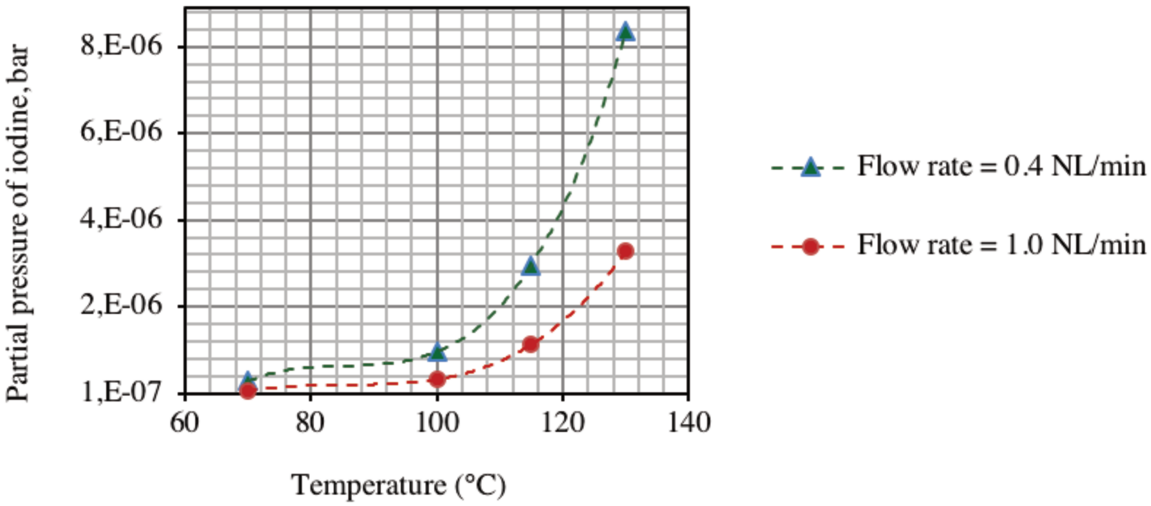

Figure 4-9 Partial pressure of I_2 inside the FTR for different generation temperatures and flow rates of Ar. Iodine generation at 130°C, 115°C, 100°C, and 70°C; carrier gas flow rate at 1.0 and 0.4 NL min^{-1}. The statistical errors on each single data points are within the symbol size.

After performing the calibration tests at different temperatures of the permeation tubes, the temperature of the permeation oven was set at 70°C and Q_{Ar} at 0.4 NL min^{-1}. Several tests were performed to check the reproducibility of the generated I_2 partial pressure (concentration) in the FTR. The arithmetic mean of the data from 17 tests is shown in Figure 4-10, where the standard deviation (SD) calculated for all the tests is plotted as error bars. It was found that the value of SD is very small which signifies that the data are closely distributed around the mean value. The calculated arithmetic mean is inside the standard deviation implying that the major cause of dispersion of the experimental data is the reproducibility of the tests where

the main source of discrepancies are the iodine generation and/or iodine trapping on the walls of FTR and associated gas lines.

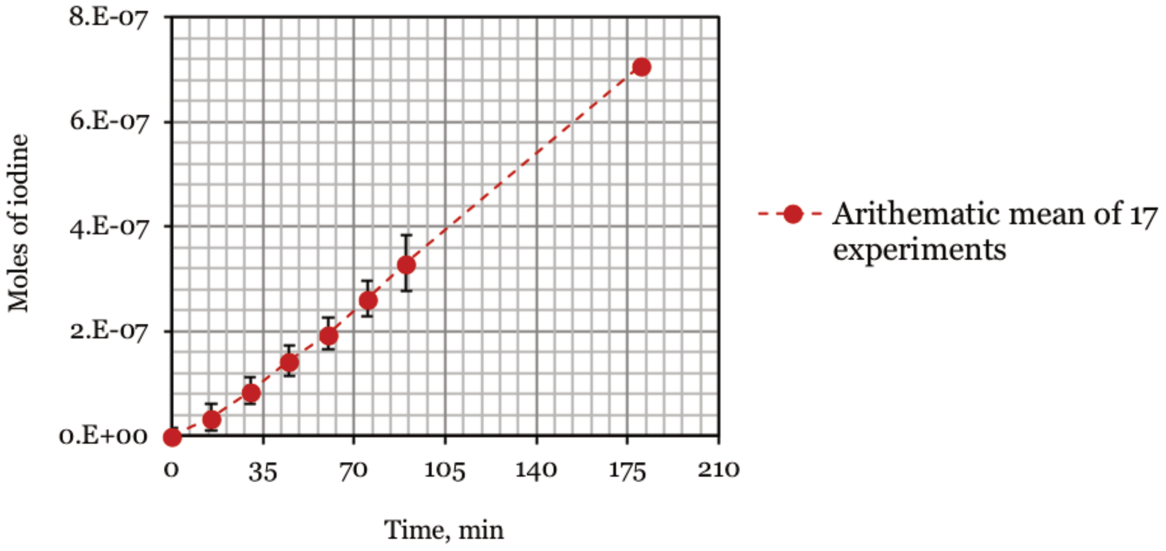

Figure 4-10 Evolution of accumulated moles of I_2 inside the gas trap bubblers, I_2 generation at 70°C and for Q_{Ar} 0.4 NL min^{-1}. The errors quoted are 1σ, statistical.

4.7.5 Measurement, stability, and precision

In order to check the stability of I_2 generation with respect to time for each permeation tube temperatures and carrier gas flow rate several calibration tests were performed. The average quantity of I_3^- measured as well as the standard deviation are reported in for 17 experiments performed with a permeation tube temperature of 70°C and an argon flow rate of 0.4 Nl min^{-1}. The generation of I_2 using permeation tubes was found to be relatively stable as a function of time with a deviation of less than 1% over the average values. The deviation observed was mainly due to small variation in the I_2 flowing through the FTR; this could be due either due small variations in I_2 generation flow rates or loss of I_2 by deposition in the facility (or temperature fluctuations).

A few experiments were performed to quantify the concentration of I_2 deposit on the walls of the reactor and analysed in UV spectrometer. The concentration of I_2 deposited was found to be below the detectable limit of the UV-spectrometer device. The samples were then analysed with more sensitive ICP-MS instrument. The concentration of iodine was found to be in the order of 103 ppb equating to 0.2 - 2% the total generated I_2 for the entire length of the experiment.

For all the calibration tests performed, the average I_2 concentrations and mole fractions have been calculated. For our experiments typical ranges of I_2 molar

fraction and concentration in argon are summarized in Table 4-3. The calculated iodine mole fractions are in the range of expected concentrations for molecular iodine in the containment in case of a SA (10^{-8}-10^{-6} M).

Table 4-3 Calculated I_2 concentration inside the FTR. Q_{Ar} argon flow rate; *PM* iodine permeation tubes.

Q_{Ar} Nl min^{-1}	PM temperature, °C	I_2 mole fraction, ppm	I_2 concentration mole l^{-1}
0.4	70	0.21	7.4×10^{-9}
	100	2.5	8.1×10^{-8}
	115	3.5	1.1×10^{-7}
	130	9.2	2.8×10^{-7}
1	100	1.3	4.2×10^{-8}

4.7.6 Experimental protocol

As a first step, the so-called calibration runs were performed without the sorbent in the FTR to determine the iodine flow rate. Then 10 ml aliquots were analyzed every 10 minutes with UV spectrometer (at both 350 nm and 297 nm, see Figure 4-5) then I_2 (g) evolution rate was determined in moles min^{-1} (M_C), as explained in the previous section. Then, in a second step, using a 3-way valve, the flow of I_2 (g) was directed through another gas-trap bubbler containing NaOH solution. Then the FTR was opened, while heating was always on. A known mass of carbonates was introduced in the FTR. After closing the reactor, the 3-way valve (made of glass and Teflon) was turn again to direct the flow of I_2 (g) into the FTR. The time corresponding to this opening was taken at the initial time (t=0) for the uptake experiment. The scrubber solutions were then collected at different evolution times and analyzed with UV spectrometer to determine the concentration of I_2 (g) in the sample (M_K, moles min^{-1}). The breakthrough concentration of I_2 (g) from the experiments with the sorbent in the FTR was then compared to the calibration runs and the capture efficiency of the sorbent was determined using Equation 4-13. Figure 4-13 shows a detailed flowchart of the experimental protocol.

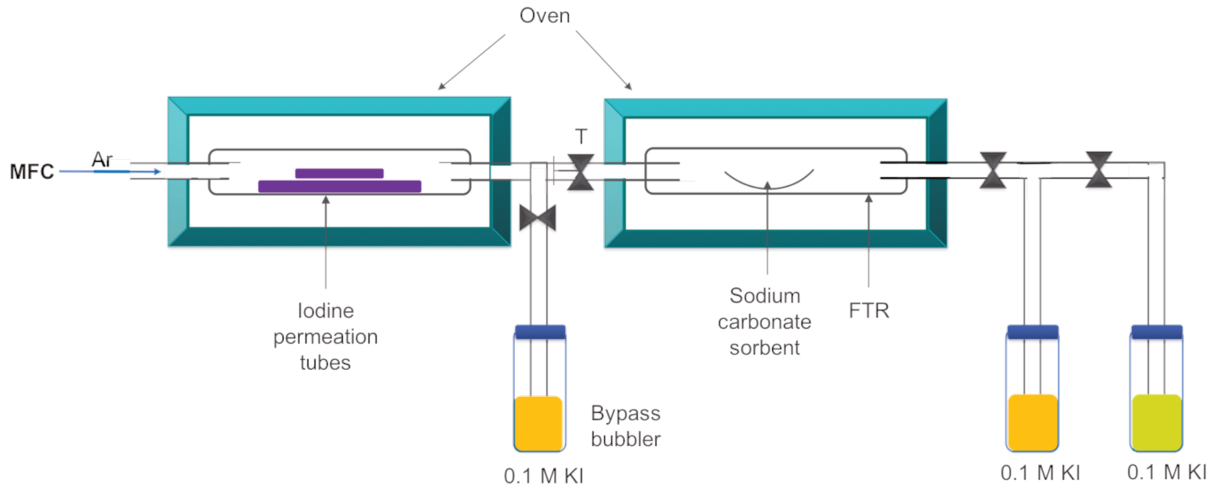

Figure 4-11 Flow tube reactor setup. Ar containing I_2 (g) between 0.05 and 5 ppm. *MFC* mass flow controller; *FTR* flow tube reactor; *T* three-way valve.

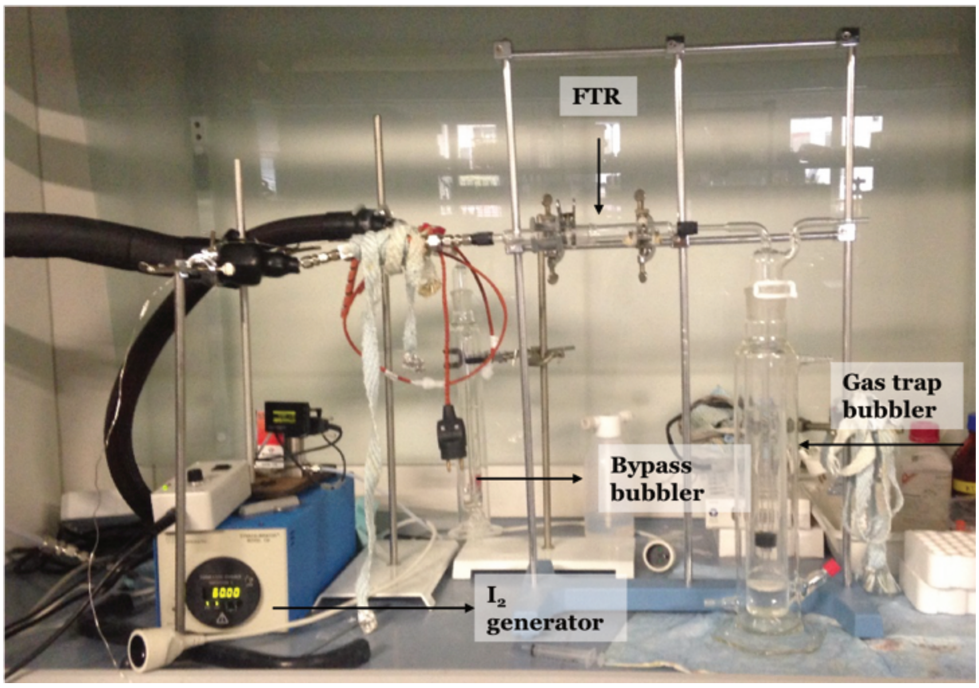

Figure 4-12 A picture of the experimental setup to study iodine uptake by sodium carbonate sorbent. The primary components, I_2 generator, gas-trap bubblers, and the FTR are marked.

$$\% \text{ capture efficiency} = \frac{\Delta M_C - \Delta M_K}{\Delta M_C} \times 100,$$

where, ΔM_C and ΔM_K are the time derivatives of the I_2 (g) concentration measured from the calibration run (without sorbent) and the kinetics run (with carbonate) for the same evolution time, respectively. It is worth noting that ΔM_C is nothing but the slope of the straight line joining the points obtained from calibration run.

It should be noted that capture efficiency is a time dependent quantity; and it strongly depends on the detection limit of the instrument.

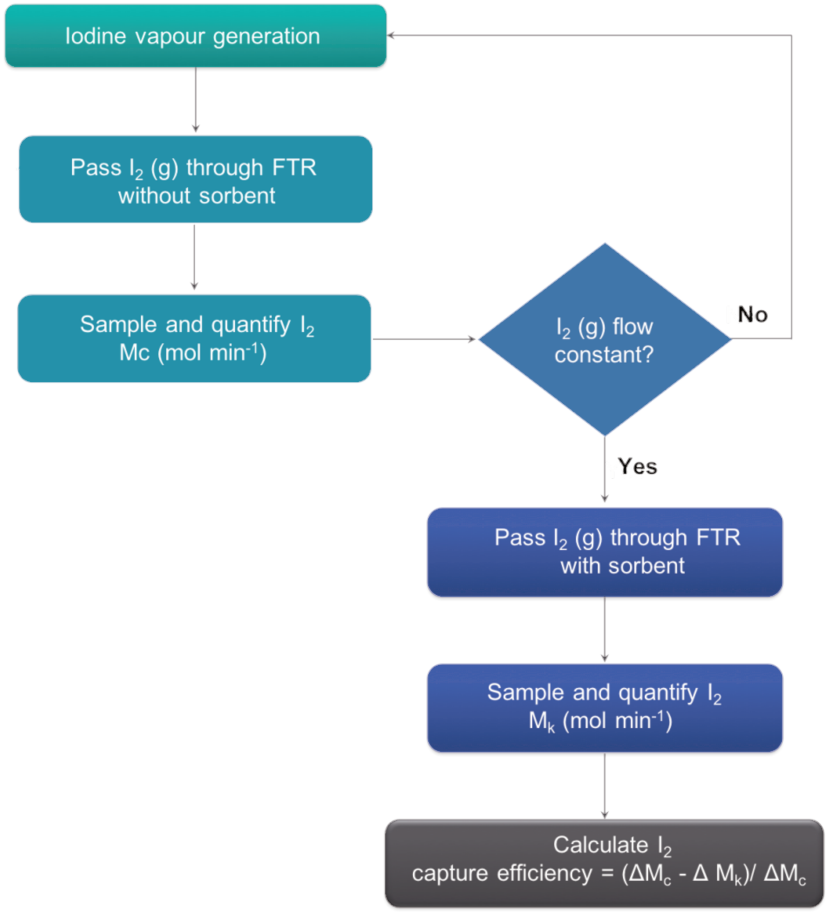

Figure 4-13 Flowchart of the experimental protocol followed for iodine capture calculations using the FTR facility.

The timeline of an experiment is displayed in Figure 4-14. It is worth mentioning that conducting one set of experiment (calibration and kinetics run) takes about 9-10 hours.

Heating phase: When the FTR and the PFA tubes are heated at a constant temperature. Since temperature is a primary parameter controlling the reaction

kinetics, special attention was given to attain stabilized temperature which takes about one hour.

Calibration run: When iodine vapors are passed through the empty FTR. After the calibration run, the FTR is opened and the sorbent is placed inside it. The whole experimental line is again heated; a constant temperature is achieved. During this time the iodine flow is directed towards the bypass bubbler.

Kinetics run: Once the temperature is stable, the iodine flow is directed towards the FTR and the samples are taken.

Cooling phase: After the kinetic experiment, the heating is stopped and argon is flown above the permeation tubes until they reach room temperature.

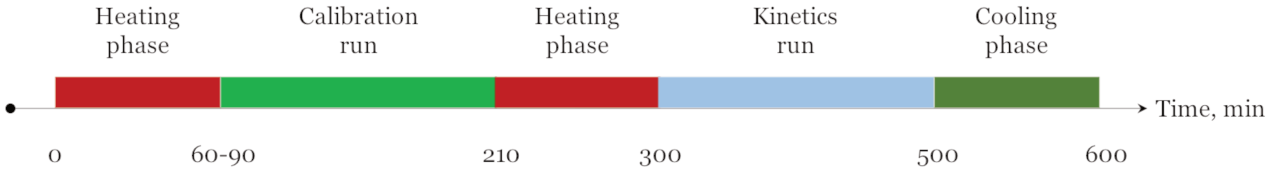

Figure 4-14 Figure showing timeline of the experiment performed using the FTR. Time for conducting one set (calibration + kinetics run) of experiment is roughly 10 hours.

Several assumptions were made for this experimental technique, which are listed below:

- The carrier gas and I_2 (g) are rapidly and well mixed and the gas mixture behave like an ideal gas
- Negligible friction between the walls of the reactor and the gas mixture;
- Negligible pressure drop across the length of the reactor
- Negligible change in velocity and density of the gases across the length of the reactor.

These assumptions are supported by the low concentration of molecular iodine generated by the permeation tube and the low velocity flow rate through the FTR.

For each experiment (with or without carbonates in the reactor), the concentration of I_3^- was measured periodically by sampling 5 -10 mL of solution in the bubbler. The total quantity of matter (in mole of I_3^-) is then plotted against time (min). The typical experimental data are reported in Figure 6-3. The experimental data were fitted using a linear function with slope of the fit the flow rate.

4.8 Quantification of the I_2 (g) uptake by Na_2CO_3 – optical cell

The measurement principle are described in detail by Johansson *et al.* [86] and was already reported in this manuscript (Section 4.6). Only the set-up and protocol used in our experiments will then be detailed here.

4.8.1 Experimental set-up

Optical measurement devices

The incoherent green LED source is coupled to an optical stainless steel cavity (50 cm long) through a short focal length lens (f = 72 mm). Due to the long optical cavity used, effective absorption path lengths of up to 1-10 km can be achieved, which allows for significant enhancement of detection sensitivity while keeping the setup very compact. The cavity mirrors (Layertec, 1-m radius of curvature), have a maximum reflectivity greater than 99.99% at around 532 nm. A lens of 175 mm focal length is placed closely behind the output mirror and focuses the cavity output into a slit through the spectrometer (AndoriDus) which is controlled by a PC through a USB connection. The light is then imaged onto a chilled CDD camera. Temperature stabilization is applied to the LED, the spectrometer, and the optical cavity. The optical cavity is equipped with two sensors (P_{cell}, T_{cell}) making it possible to measure continuously the pressure and the temperature of the gas inside. In order to have a constant flow going through the measurement cell, a critical orifice with a diameter of 560 µm was inserted between the cell outlet and the vacuum pump and a bypass tube was inserted at the end of the gas mixing tube before the cell entrance. Pressure is measured upstream and downstream the critical orifice. The optical cavity is flushed with an inert gas (argon) several minutes before starting measurements to avoid adsorption/desorption on surfaces and loss of iodine on the cavity surfaces and the gas line walls, they were heated to a temperature about 100°C

Gas lines

The general diagram of all the upstream and downstream gas lines connected to the optical cell is given in Figure 4-15. Molecular iodine which was generated by heating the permeation tubes (as explained in Section 4.4) and diluted in the carrier gas is

injected in the middle of the cavity through a heated mixing line of about 2 meter length.
The permeation tube exhaust line is connected through a three-way valve either to the optical cavity or to a calibration line allowing the measurements of the generated I_2 flow rate through liquid traps or to the general rejection (suction hood) via a line including a manual valve and an activated carbon filter. There are four different argon gas line connected respectively to:

The two optical cavity mirrors to reduce as much as possible the deposits and condensations of vapors or aerosols on the mirrors,

- To the permeation tubes to dilute and flow the generated iodine
- To the mixing line to dilute the flow of generated I_2.

The gas flow in each of the lines is controlled using a mass flow meter as shown in Figure 4-15.

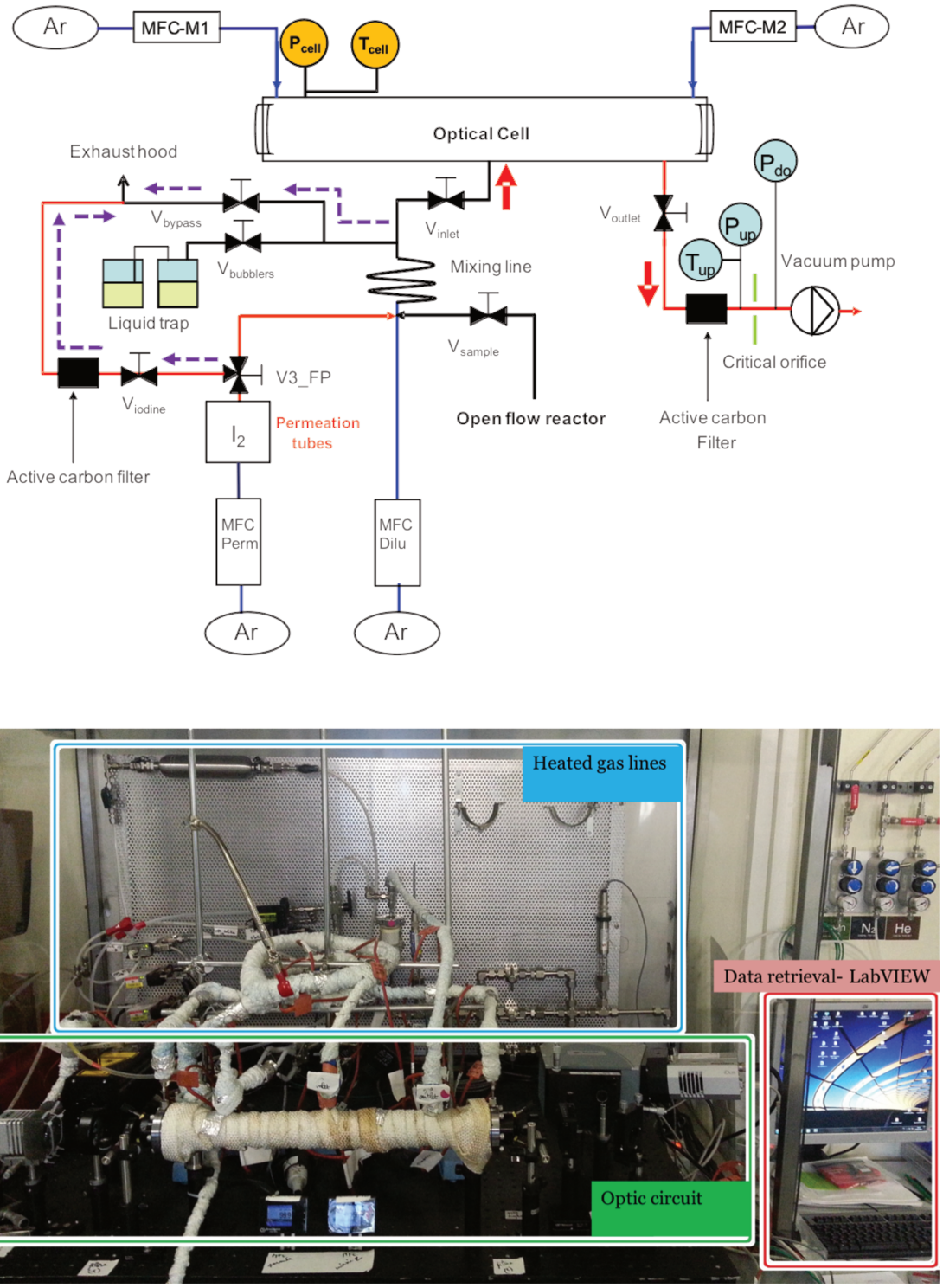

Figure 4-15 Top: Schema of the gas lines connected to the optical cell of the IBBCEAS device. *MFC* mass flow controller. *V* valve; *Ar* pure argon gas supply; *P* pressure; *T* temperature. Bottom: Laboratory experimental setup.

4.8.2 Experimental protocol

The experimental protocol was the same as explained for the FTR in Section 4.7.6. First, calibration runs were performed to have a baseline. In a second step, the sorbent was introduced in the optical cell. In both the steps, quantification of the concentration of iodine was performed using IBBCEAS device. The capture efficiency of the sorbent was calculated as:

$$\% \text{ capture efficiency} = (1 - \Delta n_{rel}) \times 100, \quad 4\text{-}14$$

where:
n_{rel}: relative number density measured by the IBBCEAS device

Measurements of iodine

Only relative measurements are performed in the IBBCEAS set-up where the ratio $n_{I_2,sampling}/n_{I_2,calib}$ of the molecular iodine density during respectively the experiments $n_{I_2,sampling}$ and the calibration tests $n_{I_2,calib}$ can be written as:

$$\frac{n_{I_2,sampling}}{n_{I_2,calib}} = n_{rel} \times R_{P,T} \left(\frac{Q^0_{CO,sampling}}{Q^0_{CO,calib}} \right) \times \left(\frac{Q^0_{dilution,sampling} + Q^0_{sampling}}{Q^0_{dilution,calib} + Q^0_{perm}} \right) \times \left(\frac{Q^0_{CO,calib} - Q^0_{mirror,calib}}{Q^0_{CO,sampling} - Q^0_{mirror,sampling}} \right), \quad 4\text{-}15$$

where,

- $n_{rel} = n_{I_2,sampling}/n_{I_2,calib}$: relative density of the molecular iodine in the optical cavity calculated according to the procedure described in Section 4.6

- $R_{P,T}$:ratio of the pressures and temperatures of the fluid in the cavity during the calibration tests and the experiments

- $Q^0_{dilution}$, $Q^0_{sampling}$, $Q^0_{permeation}$, Q^0_{mirror}, Q^0_{CO} : gas flow rates under standard conditions (T = 0°C and P = 1.0132 bar) respectively through the critical orifice, injected

via the dilution line, at the outlet of the sampling line, injected via the calibration line and protection of the mirrors (= sum of the flow rates at each mirror).

For constant mirror protection flows, and in situations where the pressure and the fluid temperature in the optical cavity as well as the flow rate through the critical

flow during the calibration and sampling phases do not vary significantly, the correlation 4-15 is simplified as follows:

$$\frac{n_{I_2,sampling}}{n_{I_2,calib}} = N_{rel} \times \left(\frac{Q^0_{dilution,sampling} + Q^0_{sampling}}{Q^0_{dilution,calib} + Q^0_{perm}} \right) \quad 4\text{-}16$$

If the dilution gas flow is fixed in such a way that $Q^0_{dilution,sampling} + Q^0_{sampling} = Q^0_{dilution,calib} + Q^0_{perm}$, the value N_{rel} thus provides a direct reading of the ratio $n_{I_2,sampling}/n_{I_2,calib}$.

4.8.3 Instrument performance: stability, precision, detection limit

An excellent stability over time of the IBBCEAS signals even in presence of sorbent was observed. Figure 4-16 shows several hours of acquisition signal with a time resolution of ~ 30 s. The standard deviation is less than 1% (Figure 4-10) The same iodine concentration level for both calibration and measurement ($n_{rel} = 1$) was used. The theoretical sensitivity of the measurement is estimated from the noise in a baseline $\Delta(I_0/I)$ assuming a mirror loss T ≈ 0.001 % and a cavity length 50 cm. For 10 s acquisition time, a noise level of ~ 5×10^{-10} cm^{-1} is obtained in the LED emitting spectrum range. Taking into account the maximum absorption cross section of I_2 at 533 nm measured by Saiz-Lopez et al. [90] ($\sigma = (4.24\pm0.50)\times10^{-18}$ $cm^2\times molecule^{-1}$), the minimum detectable concentration of iodine would be about 1×10^8 $molecules\times cm^{-3}$ i.e. 2×10^{-4} nmol/l (≈ 10 pptv). In fact, the measured detection limit is rather ~ 5×10^{-2}nmol/l, i.e., ~ 1 ppb.

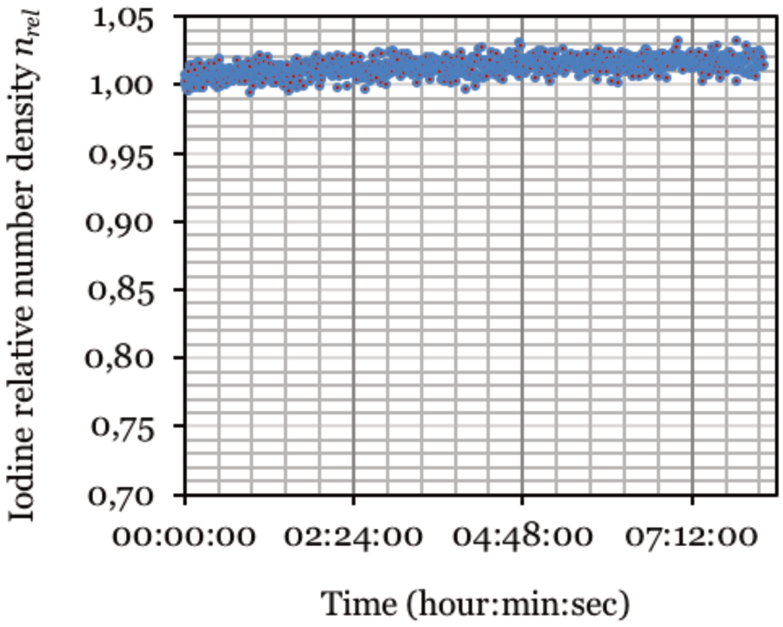

Figure 4-16 Iodine relative density n_{rel} versus time (n_{rel} = 1.008 ± 0.008).

4.9 Summary

Two different experimental setups and approaches were used to study the reaction kinetics of molecular iodine adsorption on sodium carbonates with the aim of ensuring stable and consistent results. IBBCEAS setup provided on line measurements while the flow tube reactor was that only provided discrete measurements was more easy to handle. Since the temporal resolution of IBBCEAS (1 measurement per 30 sec) was higher compared to the UV spectrometry (1 measurement per 10-15 min), it means that the FTR is not really applicable for fast kinetics reaction. However, it was possible to measure it in our experiments due to the low concentration of molecular iodine chosen which lead to time duration for the sodium carbonate surface saturation high enough to be measured in the FTR. In both the cases, reaction kinetics was studied and compared. The transient time when the sodium carbonate sorbent turns from reactive (i.e., adsorbing iodine) to non-reactive (i.e., after Na_2CO_3 surface saturation) was compared.

Chapter 5 DFT study of reactivity of γ-Na_2CO_3 surfaces

The reactivity of surfaces is controlled by a number of factors such as surface morphology, impurities, surface defects, binding energies between adsorbent and the adsorbate, interactions between adsorbents, and so forth. Generally, to simply the multi-dimensional problem in hand, in surface science, one tries to single out the factors and come up with simplified models to explain their influence on reactivity. A combination of various detailed and controlled experimental and theoretical studies would lead to a deeper understanding of the surface reactivity.
In this work, we probed the surface structures of γ-Na_2CO_3 and predicted their geometries at equilibrium. Furthermore, the reactivity of the two most stable surfaces was investigated with iodine based FP and water vapor. This chapter deals with the results obtained with ab-initio DFT calculations.
First a literature review of Na_2CO_3 and a chemically similar system are given. The crystal structure of Na_2CO_3 is discussed the next. As mentioned previously, the aim of the DFT calculations is to predict the adsorption isotherm. An analytical ab-initio based isotherm model was presented in Section 5.4. Some simplifications in the model are presented in this chapter; the analytical model was then applied to produce adsorption isotherms of the reactions between the two surfaces of Na_2CO_3 and I_2, HI, and H_2O.

5.1 Background

Previously, Dubbledam *et al.,* [91] investigated the crystal structure of Na_2CO_3 using experimental X-ray diffraction methods. More recently, Duan *et al.,* [92] used DFT to investigate the phase diagrams for multi-component systems M-C-O-H (M=Li, Na, K). Their calculations were found to be in good agreement with the experimental results. Here, we would like to emphasize that to our knowledge there is no theoretical or experimental information in the literature on Na_2CO_3 surface stabilities and their chemical reactivity. However, a DFT study on a chemically

similar system, K_2CO_3, has been done by Gao *et al.*, [93] to study its surfaces and interaction with H_2O and CO_2.
In this chapter, we investigate the stability of various surfaces of γ-Na_2CO_3 and their reactivity with I_2 (g), HI (g), and H_2O (g) using ab-initio DFT [54], [55]. The extrapolation of DFT data form 0K to any temperature, T, and pressure, P is possible as proposed by Scheffler *et al.,* [94]. Such an extrapolation allows to draw Gibb's free energy of the surface as a function of chemical potential of the gas phase and to determine the predominance zones of different surfaces. The predominance zones can also be presented as (pressure, temperature) diagram. However, this method does not allow direct quantification of the adsorption isotherm (the uptake of gas phase species by the considered surfaces at the thermodynamic equilibrium). Therefore, to address this point, a model was developed which is presented in Section 5.4 to relate the adsorbed phase with the total available surface area of the adsorbent. This model establishes the coexistence of different surfaces (with different coverages) as a function of partial pressure and temperature. This quantification of the uptake is needed for the calculation of the residual partial pressure of the gas phase species and hence the determination of the source term.

5.2 The crystal structure of Na_2CO_3

The crystal structure of anhydrous Na_2CO_3 has been widely investigated using theoretical approach [95] as well as experimental techniques such as X-ray diffraction [96], synchrotron X-ray [97], IR and optical data [98]. This compound shows several temperature-dependent phase transitions; α-Na_2CO_3, (hexagonal; 756-972 K) → β-Na_2CO_3, (monoclinic; 605-751 K) → γ-Na_2CO_3, (incommensurate monoclinic; below 605K) → δ-Na_2CO_3, (commensurately modulated, lock-in phase, monoclinic; stable below 170 K). The phase transitions are associated with the tilt of rigid triangular CO_3 units [97].

5.3 Results

5.3.1 Bulk Na_2CO_3

Four phases of Na_2CO_3, named α, β, γ, and δ exist at atmospheric pressure. A continuous phase transformation between the, β, and γ phases has been observed as a function of temperature [99]. The crystal lattice parameters are mentioned in Table 5-1.

Table 5-1: Crystal phases and lattice parameters of the Na_2CO_3

Specie	Temp (K)	Symmetry	a, b, c (Å) β (°)
α	754-1000	$P6_3/mmc$	5.20, 5.20, 6.50, 120
β	605-754	C2/m	9.01, 5.23, 6.32, 96.8
γ	170-605	C2/m	8.90, 5.24, 6.04, 101.3
δ	< 170	P21/n	8.89, 5.23, 5.99, 101.8

Phase γ was chosen for this study as it is stable at a temperature range (170-605 K) which corresponds to the expected temperatures in the larger part of the containment during and following an SA. The γ-Na_2CO_3 phase belongs to C2/m space group with four formula units (Z=4) in the primitive cell. The crystal structure of γ-Na_2CO_3 is shown in Figure 5-1. The lattice parameters obtained from experimental work [100] are a = 8.905 Å, b = 5.237 Å, c = 6.045 Å, α = γ = 90°, and β = 101.32°. The crystal lattice parameters were optimized using DFT and DFT-D3 methods, the relative deviation with respect to the experimental values are shown in Table 5-2.

Duan *et al.,* [101] reported DFT optimized crystal lattice parameters using PW91 exchange-correlational functional for γ-Na_2CO_3 in C2/m symmetry which shows reasonable agreement with the experimental values and the optimization done in this study. For this study, the maximum deviation from the experimental values remains under 2% for both PBE and PBE-D3 methods. Nevertheless, in this work, the experimental values of γ-Na_2CO_3 were used.

Table 5-2: Experimental, PBE, and PBE-D3 calculated crystal lattice parameters of Na_2CO_3.

	a	b	c	β
Experiments [100]	8.905	5.237	6.045	101.32
Duan *et al.*- [102] PW91	8.951	5.335	6.138	102.21
This work - PBE	8.956	5.336	6.144	102.06
Relative deviation, %	0.58	1.88	1.64	0.73
This work - PBE-D3	8.877	5.327	6.017	103.22
Relative deviation, %	-0.31	1.72	-0.45	1.88

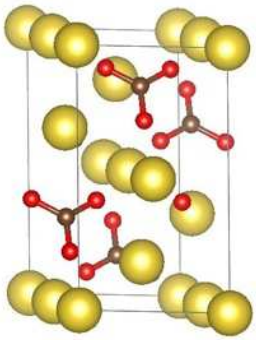

Figure 5-1: The optimized primitive unit cell crystal structure of Na_2CO_3. *Yellow*, Na; *red*, O; *Brown*, C.

5.3.2 Surface energy

The surface energies of various low index terminations were evaluated using Equation 3-42. The (001) surface of γ-Na_2CO_3 was found to have the lowest surface energy, hence expected to dominate the equilibrium concentration of γ-Na_2CO_3 aerosols. The energies of various low index cleavages are summarized in Table 5-3. The order of stability of the surfaces is (001)>(110)>(100)>(010)>(101)>(111).

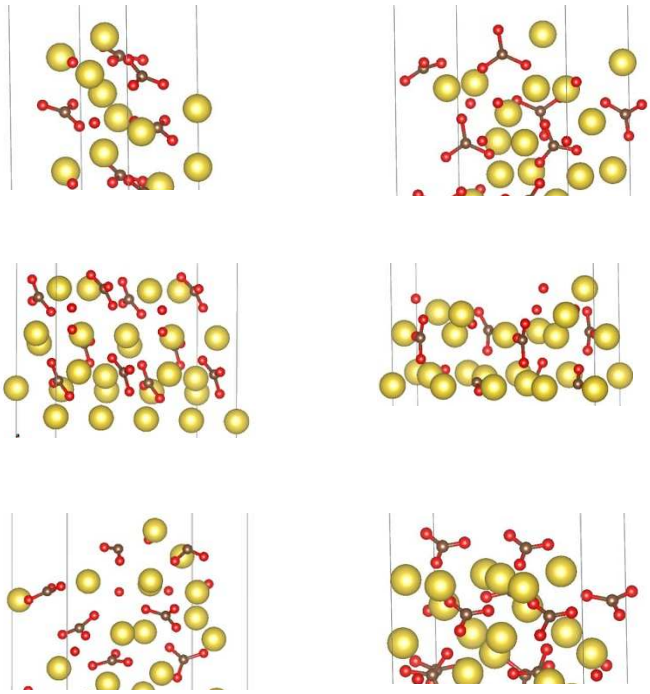

Figure 5-2 Side views of the surface primitive cells of γ-Na_2CO_3. From top to bottom, left to right: (001); (110); (100); (010); (101); (111). Yellow, Na; red, O; brown, C.

Table 5-3: DFT-D3 calculations of the specific surface energies of (001), (010), (011), (101), (110), and (111) surfaces of Na_2CO_3.

Surface facet	Surface energy, ($eV.Å^{-2}$)
(0 0 1)	0.09
(1 1 0)	0.23
(1 0 0)	0.28
(0 1 0)	0.30
(1 0 1)	0.55
(1 1 1)	0.88

As mentioned in the introduction, there is no information on γ-Na_2CO_3 surfaces. However, in DFT study on a similar system, K_2CO_3, by Geo *et al.,* [93] it was reported that the (001) surface is the most stable cleavage of K_2CO_3 which is consistent with our results on γ-Na_2CO_3.

Wulff construction

The surface formation energies were compared for a group of surfaces to establish which surfaces are likely to be exposed in the crystal. To estimate the abundance of different surfaces, the Wulff construction model was used [103], see Figure 5-3.
Surface energies of calculated low index surfaces were used in standard Wulff construction software to generate the polyhedron that corresponded to the equilibrium shape of the crystal with different cleavage surfaces at the thermodynamic limit of large particles.
At realistic conditions, the equilibrium concentration of the Na_2CO_3 aerosols will have more than just one surface. As expected due to the lowest surface energy, the Wulff polyhedron suggests that the surface cleavage (001) will dominate the equilibrium concentration at 0 K occupying 77% of the total area. While the surface cleavage (110) and (100) occupy 21% and 2% of the total polyhedron area respectively. In this work, we present the reactivity of the surface (001) and (110).

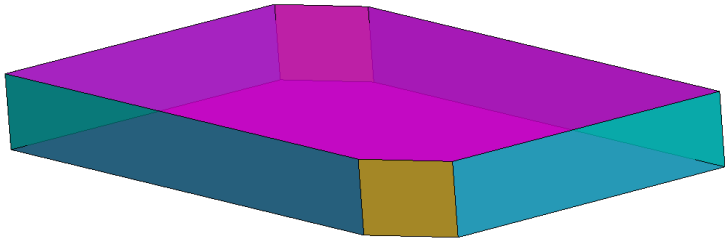

Figure 5-3: Atomistic Wulff constructions for clean γ-Na2CO3 crystal using surface energies calculated by DFT in this study. *Pink* (001); *green* (110); *yellow* (100). Face (001) occupies almost 77% of the total area.

Surface energies of calculated low index surfaces were used in standard Wulff construction software to generate the polyhedron that corresponded to the equilibrium shape of the crystal with different cleavage surfaces at the thermodynamic limit of large particles.

5.4 Ab-initio based analytical isotherm modelling

In this section, we present a model to extrapolate the thermodynamic data calculated at 0 K (DFT calculations) to temperatures and pressures of interest. To make it more comparable with experimental measurements and allow a quantification of the uptake (adsorption isotherms), we introduce the surface coverage ratio (θ) in the calculation of equilibrium partial pressure expression. The aim is to study the nature of adsorption isotherm covering vast possibilities of isotherms, from Langmuir isotherm adsorption[13] to BET isotherm adsorption[14] [104], [105]. The thermodynamic formulas presented hereafter are widely available in the literature [106], [107]. Nevertheless, a brief review is presented.
The surface coverage ratio (θ_n) was defined as the number of sites occupied by 'n' molecules of gas over the total available sites on the surface. With this definition, θ_0 is the ratio of unoccupied sites to the total number of available sites; θ_1 is the ratio of single occupied sites to entire sites and so forth.

5.4.1 Basic assumptions and developments

If the supercell is chosen large enough (large S) so the interaction between ligands adsorbed in neighboring cells is negligible. On such a large surface, the adsorption of the first molecule (g) follows the Langmuir adsorption model.

[13] Disperse monolayer adsorption

[14] Multilayer adsorption

Such adsorption reaction (^{1}r) can be written as:

$$r^1: S_0 + g = S_1$$

S_0 stands for an unoccupied site (bare surface), g for a molecule of the gas phase and S_1 a singly occupied site.

Similarly, as the adsorption of a second (or nth) ligand is not affected by the equivalent adsorption in the neighboring cells (at every adsorption the added molecules are separated by the width of the supper cell, which is assumed to be large enough, say >10Å):

$$\begin{gathered} r^2: S_1 + g = S_2 \\ \vdots \\ r^n: S_{n-1} + g = S_n \end{gathered}$$

This way, we include the lateral interactions at every level of surface loading and allow an evaluation of the energy gain between successive adsorptions. The energy of the nth adsorption is:

$$\Delta_r^n E = E[S_n] - E[S_{n-1}] - E[g] \qquad 5\text{-}1$$

At global equilibrium, all these step-reactions (r^n) will be in local equilibrium, and different chemically active sites of the total surface may have a different number of molecules adsorbed per site.

Let S_{TOT} be the total surface under study. Thus, $N_{TOT} = S_{TOT}/S$ sites are available for adsorption. Let N_0, N_1, N_2 …, and N_n be the number of unoccupied, single occupied, double occupied …, and nth occupied sites respectively. Thus,

$$N_{TOT} = N_0 + N_1 + N_2 + \cdots + N_n$$

$$Q^{system} = Q_g \,.\, Q^0 . Q^1 \,.\, Q^2 \cdots Q^{max} \,.\, Q^{conf}$$

Where:

$$Q^g = \frac{q_g^{N_g}}{N_g!},$$

is the partition function of the gaseous phase. And,

$$Q^n = \{\Omega\,(n) q_n\}^{N_n},$$

is the partition function for the adsorbed phases. $\Omega(n)$ being the degeneracy[15], and, q_x stands for the molecular partition function.
Due to the coexistence of different levels of coverage the configurational partition function takes the form:

$$Q^{conf} = \frac{N_{TOT}!}{N_0!\ N_1!\ N_2! \cdots N_{max}!}$$

This configurational partition function allows taking into account the well-known self-dependency of surface coverage as we will see later.
Here we assume that, for the adsorption of 'n' molecules on S, there is only one significant local minimum with energy $E[S_n]$ and degeneracy $\Omega(n)$, any other local minimum is assumed to have a much higher energy which makes its population negligible. We should note, in the case where this assumption doesn't hold true, for example, two minima with close but different energies $E[S_n^1] < E[S_n^2]$ the population of $E[S_n^2]$ might not be negligible with respect to $E[S_n^1]$; in this case, both the configurations should be taken into account explicitly in the expression of the partition function the system:

$$Q^{system} = Q_g \,.\, Q^0 . Q^1 \,.\, Q^2 \cdots Q^{max} \,.\, Q^{conf}$$

$$Q_i^n = \{\Omega\,(n,i) q_{n,i}\}^{N_{n,i}}$$

$$Q^{conf} = \frac{N_{TOT}!}{N_0!\ N_1!\ N_2! \cdots N_{n,1}!\ N_{n,2}! \cdots N_{max}!}$$

At equilibrium, the chemical potential of every compound is given by the expression:

$$\mu_x(T) = \mu_x(0\ K) - k_B T \frac{\partial(\ln Q^{system})}{\partial N_x}$$

So, for the gas phase:

$$\mu_g(T) = \mu_g(0\ K) - k_B T ln\left(\frac{q_g}{N_g}\right) \qquad 5\text{-}2$$

[15] Different ways of adsorbing 'n' molecules on the unit surface with the same energy

And for the adsorbed phases:

$$\mu_n(T) = \mu_n(0\ K) - \ k_B\,T\frac{\partial(\ln Q^n)}{\partial N_n} - \ k_B\,T\frac{\partial(\ln Q^{conf})}{\partial N_n}$$

$$\frac{\partial(\ln Q^n)}{\partial N_n} = \frac{\partial[\{\ln(\Omega(n)q_n)\}^{N_n}]}{\partial N_n} \ = \ln\Omega(n)q_n$$

$$\frac{\partial(\ln Q^{conf})}{\partial N_n} = -\frac{\partial(\ln N_n!)}{\partial N_n} - \frac{\partial(\ln N_0!)}{\partial N_n} = ln\ N_0 - \ln N_n$$

$$\mu_n(T) = \mu_n(0\ K) - \ k_B\,T\ln\ N_0 - \ k_B\,T\ln\left(\frac{\Omega(\mathrm{n})q_n}{N_n}\right)$$

$$Or, \qquad \mu_n(T) = \mu_n(0\ K) - \ k_B\,T\ln\left(\frac{N_0\Omega(\mathrm{n})q_n}{N_n}\right) \qquad \text{5-3}$$

$$\mu_0(T) = \mu_0(0\ K) - \ k_B\,Tlnq_0$$

The Sterling formula $[\ln(N!) \approx N\ln(N) - N]$; and the expression, $N_0 = N_{TOT} - \sum_{i=1}^{max} N_i$ have been used.

For a given step-reactions (${}^{n}r$), at the equilibrium, the chemical potential equality implies:

$$n\mu_g(T) + \ \mu_0(T) = \mu_n(T)$$

Or,

$$\Delta_r^n\mu(T) = 0$$

Including Equations 5-2 and 5-3, we obtain:

$$\Delta_r^n\mu(0\ K) + k_BT\ln\left[\frac{q_0}{q_n}\left(\frac{q_g}{N_g}\right)^n\right] + \ \ k_BT\ln\left[\frac{N_n}{N_0}\ \frac{1}{\Omega(\mathrm{n})}\right] = 0$$

The first two terms in the expression above are $\left[\Delta_r^n G(T) - RT \ln\left[\left\{\left(\frac{P_g}{P^0}\right)^n\right\}\right]\right]/A_v$

Multiplying by Avogadro's constant, we obtain:

$$\Delta_r^n G(T) - RT \ln\left[\left(\frac{P_g}{P^0}\right)^n\right] + RT \ln\left[\frac{N_n}{N_0 \Omega(\mathrm{n})}\right] = 0 \qquad 5\text{-}4$$

Here we use fractional notation, as shown below:

$$\frac{N_n}{N_0} = \frac{N_n/N_{TOT}}{N_0/N_{TOT}} = \frac{\theta_n}{\theta_0}$$

Thus, at equilibrium:

$$\theta_n = P_g^n \cdot \theta_0 \cdot K_e^n \qquad 5\text{-}5$$

Where:

$$K_e^n = \frac{\Omega(\mathrm{n})}{P^{0\,n}} \exp\left(\frac{-\Delta_r^n G}{RT}\right) \qquad 5\text{-}6$$

The isotherm given the available sites (N_{TOT}) is:

$$\theta_{TOT} = \frac{N_g^{ad}}{N_{TOT}} = \sum_{n=1}^{max} n \cdot \theta_n \qquad 5\text{-}7$$

This expression evidences the self-dependency of the isotherm.

$$\sum_{m=0}^{max} \theta_m = \theta_0 + \sum_{m=1}^{max} \theta_m = 1$$

Using Equation 5-2 here, we get

$$\theta_0 (1 + \sum_{m=1}^{max} P_g^n \cdot K_e^m) = 1$$

$$\theta_{n>0} = P_g^n \cdot K_e^n (1 + \sum_{m=1}^{max} P_g^m \cdot K_e^m)^{-1} \quad \text{5-8}$$

Thus, the isotherm expression takes the form:

$$\theta_{TOT} = \sum_{m=1}^{max} n\, P_g^n \cdot K_e^n \left[1 + \sum_{m=1}^{max} P_g^m \cdot K_e^m\right]^{-1} \quad \text{5-9}$$

The presented isotherm modeling does not presume a particular case of isotherm regime (for details on isotherm modeling, see Section 3.7), hence can be applied for a variety of heterogeneous reaction systems.
The presented model was first used to reproduce isotherm curves of a well-studied system investigated by Sauer *et al.,* in the literature [108]. It was then used to produce isotherm curves of the reactions between Na_2CO_3 (s) and I_2 (g). The results are presented in Chapter 5.

5.4.2 Simplifications in the analytical adsorption isotherm model

To reduce the computational cost, we made some approximations in the expression of the isotherm presented in Section 5.4.
The partition function of the solid state q_n is entirely vibrational and can be referred to as q_n^{vib}. We can approximate the ratio q_{n-1}^{vib}/q_n^{vib} to unity; otherwise specific calculations of the energetic levels related to the internal degrees of freedom of the condensed phases (phonons) will be needed.
Similarly, $\Delta_r^n\mu(0) = \mu_n(0) - \mu_g(0) - \mu_{n-1}(0)$ can be reduced to the reaction "electronic" energy, neglecting the $\Delta_r^n ZPE$ corrections. So, we obtain the approximation:

$$\Delta_r^n\mu(0) \approx \Delta_r^n E$$

$$K_e^n = \Omega(\mathrm{n}) \cdot P^0 \cdot \exp\left[\frac{-\Delta_r^n E - \{\mu_g^0(T) + \mu_g^0(0)\}}{RT}\right] \quad \text{5-10}$$

$\Delta_r^n E$ (J.mole^{-1}) in the expression above is calculated from DFT at 0 K.
At equilibrium, the evolution of the surface coverage has been investigated as a function of partial pressure of gas-phase species at different temperatures using the

formalism above. The isotherm plots were generated to compare and calculate the uptake with respect to the total available surface using Equation 5-10.

5.4.2.1 Applicability of the analytical model

For decades, several analytical models of the adsorption isotherms have been proposed; Langmuir, Freundlich, Sips and Toth. However, these models suffer from their relatively narrow range of applicability. In this section, we apply the analytical model to a well-studied MOF[16] by Sillar *et al.*, [108], [109]. In order to make results comparable, the interaction energies reported were directly used, without any additional ab-initio calculations [108]. Recently, K. Sillar *et al.,* have pointed out the ability of the mean-field approximation to reproduce experimental isotherms, when the lateral interactions are calculated with high-level ab-initio calculations. At present, the most conceptually accurate approach is the grand-canonical Monte Carlo (GCMC) method when combined with the high level ab-initio level of calculations. However, this method is twice computationally demanding due to its dependence on both the level of ab-initio calculations and Monte Carlo sampling. The analytical model presented in the previous section is based on ab-initio calculations without any a posteriori assumption of the nature of the isotherm. The presented model does not presume the homogeneity of the adsorption while increasing the surface coverage.

In this section, this analytical model is compared with the one obtained with GCMC simulations, concerning the adsorption of CO_2 in the MOF.

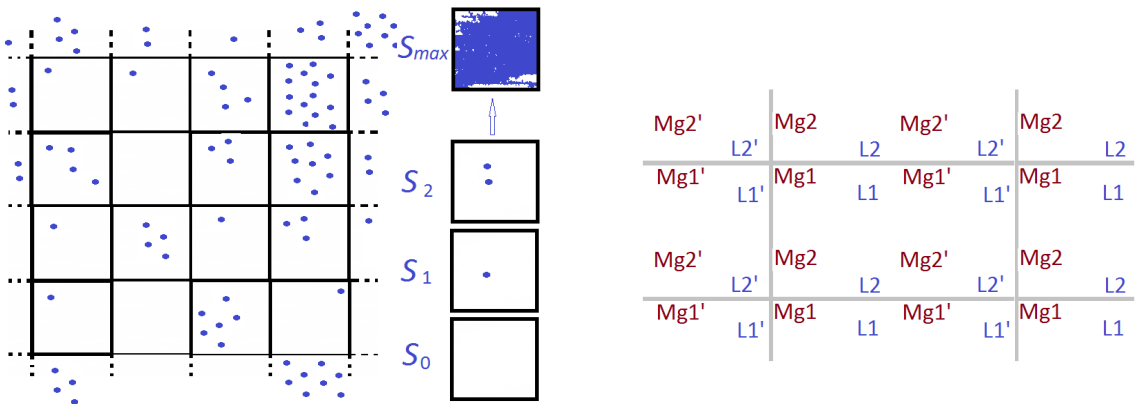

Figure 5-4 *Left*) Illustration of the coexistence of different coverages at equilibrium; *right*) representation of the supercell used in the isotherm adsorption for CO_2 in Mg-MOF-74.

[16] CPO-27-Mg (Mg-MOF-74)

The Mg-MOF-74 pores consist of successive hexagonal rings. Every ring contains six Mg sites and six Linker sites. The Mg sites constitute a local minimum of adsorption energy for CO_2 while the linker sites become a local minimum only once the neighboring Mg site is occupied. The free energies of isolated adsorption of a CO_2 molecule on Mg sites $\Delta_r G_{Mg}^{ad}$ and on linkers sites $\Delta_r G_L^{ad}$ (with the neighboring Mg site being occupied) as well as the energies of interactions between neighboring adsorbed molecules have been calculated at very high ab-initio level [108]. In this work, we did not perform any additional ab-initio calculations. We use the energies reported by Sauer *et al.,* [108] Precisely, the $\Delta_r G_{Mg}^{ad}$ at a Mg site has been calculated Mg to be -9.2 and -3.6 kJ/mole at 298 and 343 K, respectively. While for linker sites these free energies $\Delta_r G_L^{ad}$ are 5.1 and 10.5 kJ/mole at 298 and 343 K, respectively. The lateral interaction energies are in average -1.405, -1.119 and -1.057 kJ/mole for Mg---Mg Linker---Linker and Mg---linker, respectively. One should note that a part of Mg--- linker interaction energy is already included in the $\Delta_r G_L^{ad}$, since the adsorption on linker takes place after the adsorption on Mg sites, see reference [109]. Using these energies we calculate $\Delta_r^n G$ step by step and evaluate K_e^n, θ_n and the adsorption isotherm according to the Equations 5-6, 5-5, 5-7, respectively. The interactions considered by Sillar *et al.*, can be taken into account within a relatively reduced S containing four Mg sites and four linker sites, see Figure 5-4.

In the figure, the sites labelled Mg1 and Mg2 (or L1 and L2) are on the same ring, and the adsorbed molecules on these sites have a mutual Mg---Mg (or linker---linker) interactions. The case is the same for the sites labelled Mg1' and Mg2' (or L1' and L2'). The only possible Mg---Mg or linker---linker interactions are Mg1---Mg2, Mg1'---Mg2', L1--- L2, and L1'---L2'. However, the Mg---linker is possible for all the combinations: Mg1---L1, Mg2--- L1, Mg1'---L1, Mg2'---L1 ... and so on.

Due to the difference between $\Delta_r G_{Mg}^{ad}$ and $\Delta_r G_L^{ad}$ the adsorption on the linker sites is negligible until the Mg sites are completely saturated. So the adsorption of the first four molecules can be considered on the Mg sites and the later on the linker sites. The only interaction affecting the first reaction free energy is the isolated adsorption on an Mg site ($\Delta_r^1 \mathrm{G} = \Delta_r G_{Mg}^{ad}$) and the product ($S_1$) is of quadruple degeneracy, $\Omega\,(1) = \binom{4}{1} = 4$ due to the existence of four equivalent Mg sites in the S_u. For the second reaction (adsorption of two molecules) there are six possibilities:

1. Adsorption on different rings (M1- M1', M1-M2', M2-M1' and M2-M2') these four configurations are degenerated and do not include any lateral interaction, while
2. The adsorption on the same ring (M1-M2 and M1'-M2', which are degenerated) is stabilized by twice the Mg---Mg interaction (M2 having two

neighboring occupied M1). Hence, the free energy for the second reaction is $\Delta_r^2 G = 2\,\Delta_r G_{Mg}^{ad} + 2\,E_{Mg-Mg}$ and S_2 is then doubly generated.

Table 5-4 lists the different interactions involved at every level of coverage and the degeneracy of corresponding products. Note that from the fifth to eighth adsorption the fourth lateral Mg---L interaction is already included in $\Delta_r G_L^{ad}$.

Table 5-4 summery of interactions involved at every stage of surface loading and the corresponding degeneracy.

n	1	2	3	4	5	6	7	8
$\Delta_r G_{Mg}^{ad}$	1	2	3	4	4	4	4	4
$\Delta_r G_L^{ad}$	0	0	0	0	1	2	3	4
Mg---Mg	0	2	2	4	4	4	4	4
L---L	0	0	0	0	0	2	2	4
Mg---L	0	0	0	0	3	6	9	12
Ω (n)	4	2	4	1	4	2	4	1

The calculated isotherms at 298 and 343K using this analytical expression (Equation 5-7) and the one obtained with GCMC7 method are presented in Figure 5-5. In both cases, the obtained isotherms have been scaled by 0.765 to take into account the 9availability of sites, observed experimentally. One can notice the excellent agreement between the two methods.

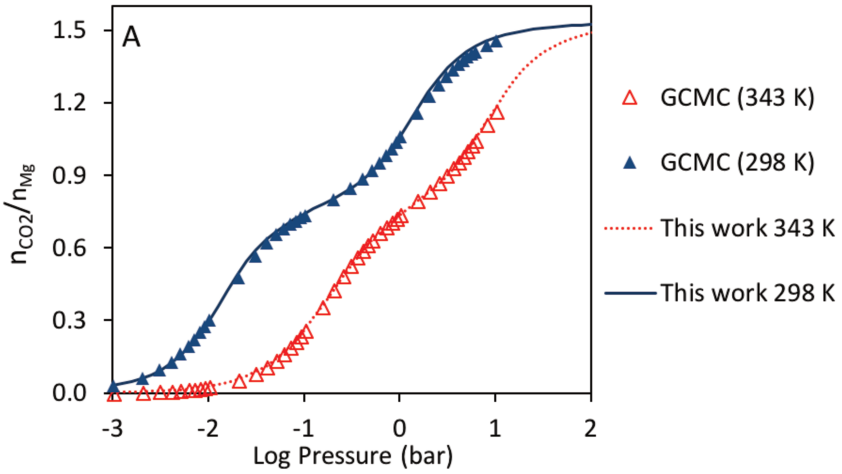

Figure 5-5 CO_2 isotherm adsorption in CPO-27-Mg at 298 (solid blue triangles) and 343 K (open red triangles) according to the presented analytical expression (lines) and calculated with GCMC. The calculated isotherms are scaled (76.5%) according to site availability [110].

We recall that the GCMC, being conceptually exact, should converge toward the thermodynamic solution of the equilibrium within two conditions: (i) all interactions are taken into account and (ii) enough sampling is performed. The presented analytical expression depends on the former, however, it allows saving the effort of sampling which could be computationally expensive. The simplified analytical model is applied to produce isotherms in the next sections.

5.4.3 Adsorption of I_2 (g) on γ-Na_2CO_3 surfaces

The main goal is to predict which case is more favorable- bare surface or a gas molecule(s) attached to a bare surface? To study the adsorption of species in gas phase to the surface, we first modelled the bare surface. The key point in periodic DFT calculation is to consider a big enough surface to avoid any interactions between the species adsorbed on the surface. We tested adsorption of iodine molecule on two surfaces: 1A-2B-3C (144 atoms) and 2A-3B-3C (432 atoms). It was observed that the adsorption energy calculated with 1A-2B-3C are lowered by 0.021 eV, compared to 2A-3B-3C but the differences between the adsorption energies of the different structures are almost the same. This is mainly due to the relaxation of now twelve instead of six surface layers.

The reconstruction of bare surface

After a complete relaxation of the bare surface, the reactivity of iodine have been investigated. The energy of the adsorption of first molecule of iodine on bare Na_2CO_3(001) surface[17] was found to be -1.402 eV. However, we noticed that re-optimization of the bare surface occurred after removing iodine from the surface. In other words, the adsorption of iodine provoked a surface reconstruction and relaxation towards a deeper potential energy well. However, this 'reconstructed surface'[18] has lower affinity for iodine. As a result of which the adsorption energy of the first molecule of iodine is reduced from -1.402 eV to -1.058 eV.
This type of reconstruction was not observed for any other gas molecules (H_2O and HI) or Na_2CO_3 (110) surface. This not-fully relaxed bare surface is not certainly relevant thermodynamically, given the huge energy difference. However, we can imagine that this surface is stabilized by an energetic barrier which could make this surface observable, in the short and medium term.
In the coming sections, calculations to investigate adsorption on the most stable bare surface (Na_2CO_3(001)-b) are presented.

[17] From now on referred as Na_2CO_3(001)-a.
[18] Referred as Na_2CO_3(001)-b.

5.4.3.1 I_2 (g) adsorption on γ-Na_2CO_3 (001) surface

As there is a possibility of having many local minima for adsorption phenomena, various initial configurations for I_2 (g) placed on the γ-Na_2CO_3 surfaces were tested. On this surface, sixteen initial configurations (positions of I_2 on the surface) have been investigated. Only the most stable configuration has been presented in Figure 5-6. The I_2 tilted adsorption structures (I-I bond inclined toward the surface) was found to be more stable than the upright adsorption structure or the bond parallel to the surface configuration. The calculated value of the bond length of I_2 in the gas phase is 2.681 Å which is in good agreement with the experimental value of 2.670 Å [111]. The calculated I-I bond length in the adsorbed I_2 molecule for the most stable configurations is 2.887 Å, which is 7% longer than the gas phase optimal value of 2.680 Å. The adsorption energy of the first molecule, $\Delta_r^1 E$ (in its most stable configuration) was found to be -1.058 eV. However, this energy of the first adsorption was found to be -1.502 eV, considering the perfectly cleaved surface.

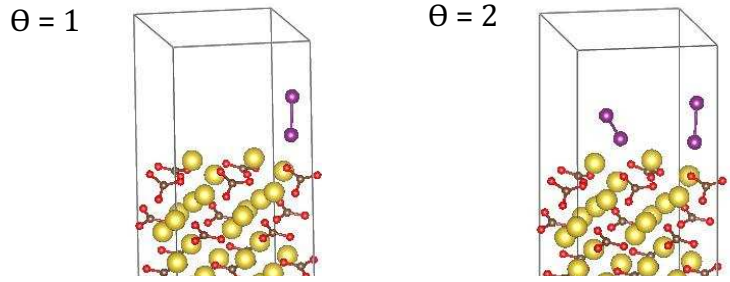

Figure 5-6: The optimized slab model of γ-Na_2CO_3 (001) with I_2 molecule on the top of it. *Yellow*, Na; *red*, O; *brown*, C; *purple*, I.

The successive adsorption energies of I_2 (g) molecules $\Delta_r^n E$ were calculated using Equation 5-1. The adsorption energy of the second molecule of I_2 (g) on (S_1) was found to be -1.261 eV (Table 5-5). The third and fourth adsorptions energies were found to be weaker (-0.840 eV and -0.588 eV respectively). The dissociative adsorption was found to be thermodynamically non-favorable.

Table 5-5: Adsorption energies of I_2 (g) γ-Na_2CO_3 (001) Surface.

n	Ω(n)	$\Delta E_r^n - \Delta E_r^{n-1}$ (eV)	ΔE_r^n (eV)
1: I_2	4	-1.058	-1.058
2: I_2 - I_2	2	-1.261	-2.319
3: I_2 - I_2 - I_2	4	-0.840	-3.519
4: I_2 - I_2 - I_2 - I_2	1	-0.588	-3.747

Table 5-5 shows that the energy of the second adsorption is more negative which implies that after the adsorption of the first molecule of I_2, the structural configuration of the surface changes in a way which has comparatively more affinity for I_2 molecule. The equilibrium coverage of I_2 was determined as presented in Section 2. The evolution of surface coverage ($\Theta_{0\to4}$) as a function of partial pressure of I_2 (g) is demonstrated in Figure 5-7, Figure 5-8, and

Figure 5-9 at three different temperatures (353.15, 373.15, and 423.15 K respectively).

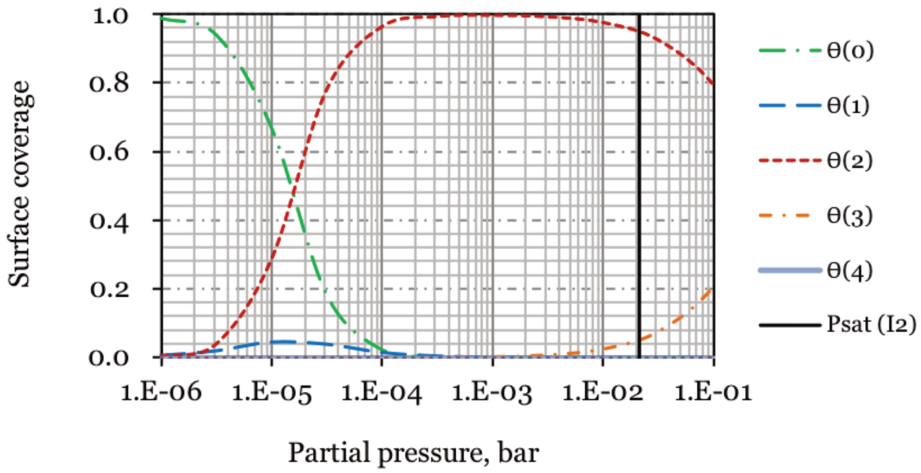

Figure 5-7: Evolution of partial pressure of I_2 as a function of surface coverage on bare γ-Na_2CO_3 (001) at 353.15 K.

At 353.15 K, Figure 5-7, the bare surface (Θ_0) is predominant exclusively for low pressures of I_2 (g) ($P<10^{-6}$ bar). As the pressure increases, the single occupied surface (Θ_1) starts developing but remains lower than 2% of the global surface. As a matter of fact, as soon as it is formed, the formation of the double occupied surface (Θ_2) is favored. With the increase of partial pressure of I_2 (g), the surface turns from the bare surface to double occupied when I_2 (g) partial pressure reaches 1.6×10^{-5} bar with a surface coverage of 49%. Beyond 2×10^{-4} bar, the surface is entirely double occupied. The third adsorption occurs right before the partial pressure reaches the intrinsic I_2 (g) saturation pressure.

At T = 373.15 K (Figure 5-8), the behavior explained above is shifted to higher partial pressures. At this temperature, the bare surface (Θ_0) prevails for I_2 (g) partial pressures below 10^{-5} bar. Actually, with an increase of partial pressure of I_2 (g), the surface turns from the bare surface to double occupied beyond 2×10^{-4} bar with a surface coverage of 49%. Beyond the 10^{-3} bar, the surface is entirely double occupied.

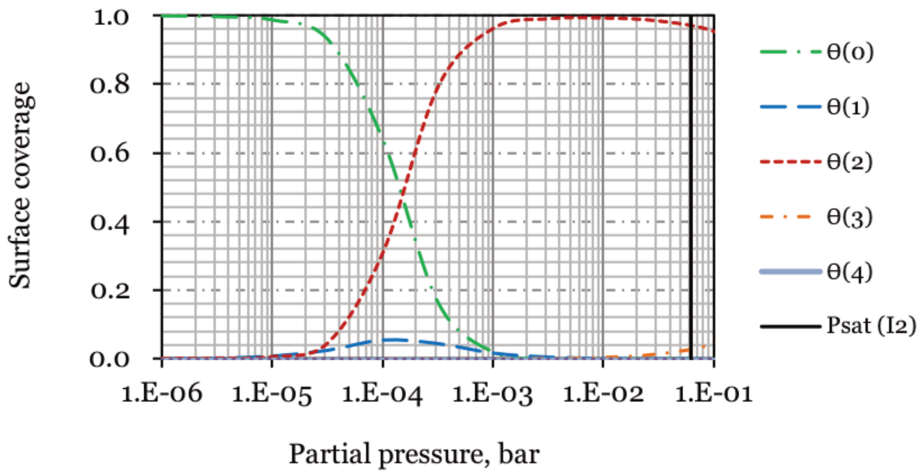

Figure 5-8: Evolution of partial pressure of I_2 as a function of surface coverage on γ-Na_2CO_3 (001) at 373.15 K.

The third adsorption starts taking place after the saturation. In reality, beyond the saturation pressure, there should be no limitation on condensation of I_2 (g). The reason behind this delay comes from the approximation we made in calculating Gibb's energy for the condensed phase, where the effect of the internal degrees of freedom (phonon) in the stabilization of the condensed phase was neglected.
Similar behavior was observed at 423.15 K (see

Figure 5-9) where the transition from double occupied to the bare surface occurs at I_2 (g) partial pressures of 2×10^{-2}bar.

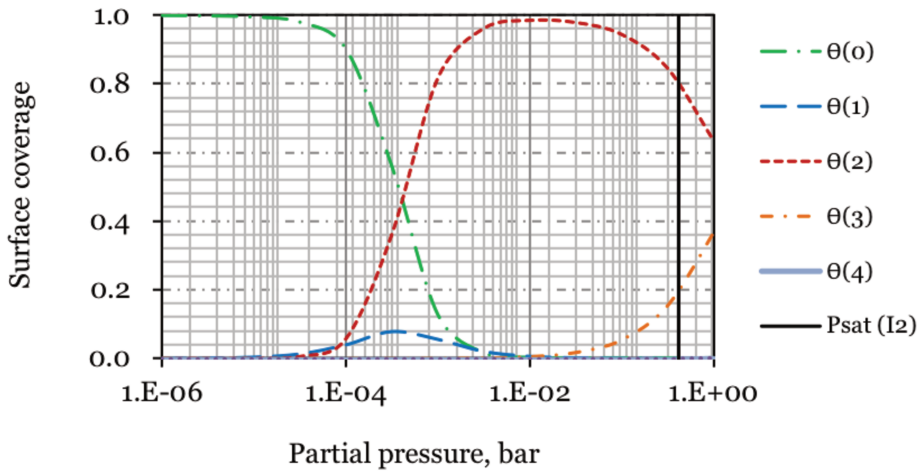

Figure 5-9: Evolution of partial pressure of I_2 as a function of surface coverage on bare γ-Na_2CO_3 (001) at 423.15 K.

5.4.3.2 I_2 adsorption on γ-Na_2CO_3 (110) surface

According to the Wulff's construction (Figure 5-3), the second most representative surface after (001) is (110), 21% of the total surface. Hence, we proceed to study I_2 (g) reactivity with γ-Na_2CO_3 (110).
Among the initial bonding configurations studied, the most stable ones are presented here, Figure 5-10.
The $\Delta_r^1 E$ (of the first molecule of I_2) on the bare γ-Na_2CO_3 (110) was found to be -1.005 eV. The adsorption energies of second, third and fourth molecules were found to be -0.790, -0.978, and -1.253 eV respectively (Table 5-6). However, the dissociative adsorption of I_2 (g) on this surface was found to be thermodynamically unfavorable.

Table 5-6: Adsorption energies of I_2 on γ-Na_2CO_3 (110) Surface.

n	Ω(n)	$\Delta E_r^n - \Delta E_r^{n-1}$ (eV)	ΔE_r^n (eV)
1: I_2	4	-1.005	-1.005
2: I_2 - I_2	2	-0.790	-1.795
3: I_2 - I_2 - I_2	4	-0.978	-2.773
4: I_2 - I_2 - I_2 - I_2	1	-1.253	-4.026

Table 5-6 shows that the fourth adsorption of I_2 (g) is the most stable.

Figure 5-11 and Figure 5-12 show the plot of θ against partial pressure of I_2 (g) at 353.15 K and 373.15 K respectively.

At 353.15 K, the bare surface predominates for low partial pressures of I_2 (g) ($<10^{-5}$ bar). The surface starts turning single occupied (θ_1) with an increase in partial pressure and occupies a maximum of 35% of the global surface when the partial pressure reaches 2.5×10^{-3} bar. The double and triple occupied sites remain negligible due to their low $\Delta_r^n E$. Thus the surface practically turns from single occupied to quadruple occupied as shown in

Figure 5-11. We can see also at 4×10^{-3} bar there is a simultaneous intersection between the bare surface, the mono-occupied and the quadruple occupied, 33% of the total surface for each kind. Beyond this partial pressure, the quadruple occupied sites start dominating the surface and become the sole existing surface, right before the saturation pressure. With an increase in temperature, 373.15 K (Figure 5-12), similar behavior was observed with a shift to higher partial pressures.

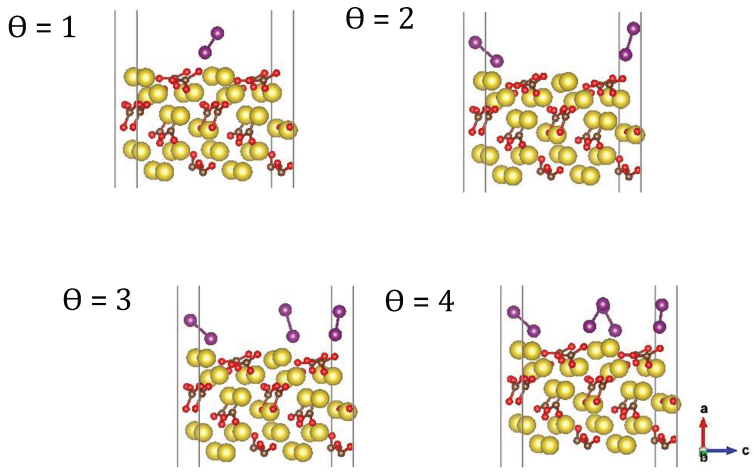

Figure 5-10: The optimized slab of γ-Na_2CO_3 (110) with 'n' I_2 molecules on the top of it. n = (1, 4). *Yellow*, Na; *red*, O; *brown*, C; *purple*, I.

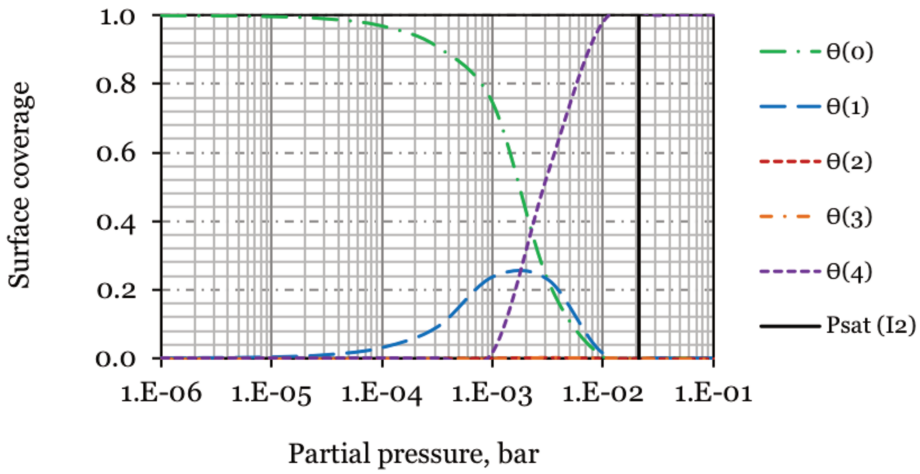

Figure 5-11: Evolution of partial pressure of I_2 as a function of surface coverage on bare γ-Na_2CO_3 (110) at 353.15 K.

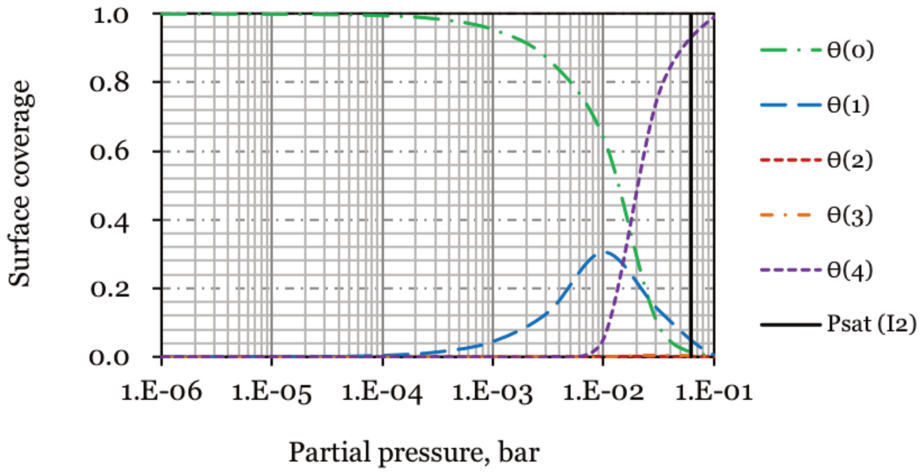

Figure 5-12: Evolution of partial pressure of I_2 as a function of surface coverage on bare γ-Na_2CO_3 (110), at 373.15 K.

5.4.3.3 The adsorption isotherm of I_2 on γ-Na_2CO_3 (001) and (110) surfaces

In this section, we present an application of the uptake calculation as presented in Section 5.4. Recalling Equation 5-7.

$$\theta_{TOT} = \frac{N_g^{ad}}{N_{TOT}} = \sum_{n=1}^{max} n \cdot \theta_n$$

We quantified the total I_2 (g) uptake by the two studied surfaces of γ-Na_2CO_3: (001) and (110). The adsorption isotherm at 373.15 K, shows that the surface (001) has a lower uptake than (110) near the saturation (two molecules per cell for the former against four molecules per cell for the latter). Precisely, when considering the surface area (93.27 $Å^2$ and 128.67 $Å^2$ for (001) and (110) respectively) we obtain the following efficiencies: one molecule per 47$Å^2$ for (001) and one molecule per 32$Å^2$ for (110). However, as mentioned previously the (001) is efficient for lower partial pressure.

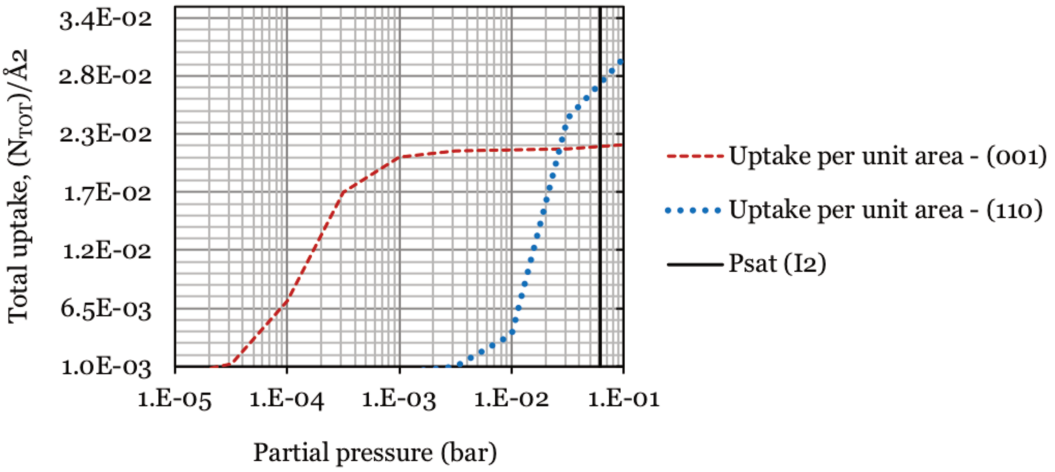

Figure 5-13 Adsorption isotherm of I_2 (g) on γ-Na_2CO_3 (001) and (110) surfaces at 373.15 K

In case of an SA, the quantity of I_2 (g) release inside the containment is very low compared to the surface area of the aerosols generated by combustion of Na (l) (Na/I is substantially high) [112]. In such conditions, and assuming that Na_2CO_3 is representative of the total generated surface, we can expect the number of adsorbed molecules (N_g^{ad}) of I_2 (g) to be sharply lower than the total available sites (N_{TOT}). So,

$$P_g^{eq} \ll N_{TOT} \; or \; equivalently \; \frac{N_g^{ad}}{N_{TOT}} \ll 1$$

In other words, in such condition, one may expect the total uptake to be lower than N_{TOT} (corresponding to one in Figure 5-13) at equilibrium. Otherwise speaking, at equilibrium, the partial pressure is expected to be much lower than 2×10^{-4} bar inside the containment at 373.15 K.
The fact that the sodium carbonate is known to be less reactive than the other expected species (Na_2O, Na_2O_2, NaOH, Na_2CO_3) one may expect the I_2 (g) uptake by the other species to be even higher. This, indeed, enforces the confidence one may put in this boundary limit of pressure.

$$P_g^{eq}(373\ K) \ll 2 \times 10^{-4} bar$$

Here, we bring the attention to iodine reactivity of the surface Na_2CO_3(001)-a (surface reconstructions explained in the beginning of this section). This surface showed stronger affinity for iodine compared to the reconstructed bare surface. The adsorption isotherms for both the surfaces are presented in Figure 5-14. It can be seen that the N_{TOT} of iodine uptake by Na_2CO_3(001)-a surface is 1 at a partial

pressure corresponding to 10^{-6} bar, however, to have the same surface coverage, the partial pressure required by the surface Na_2CO_3(001)-b is about one hundred times higher, 10^{-4} bar. This result implies that the Na_2CO_3(001)-a surface is a hundred times more reactive compared to Na_2CO_3(001)-b surface. Since, the probability of having Na_2CO_3(001)-a surface (due to the needed reconstruction to form Na_2CO_3(001)-b) in the medium/short term is not zero, one can expect that both the surfaces will contribute to iodine adsorption.

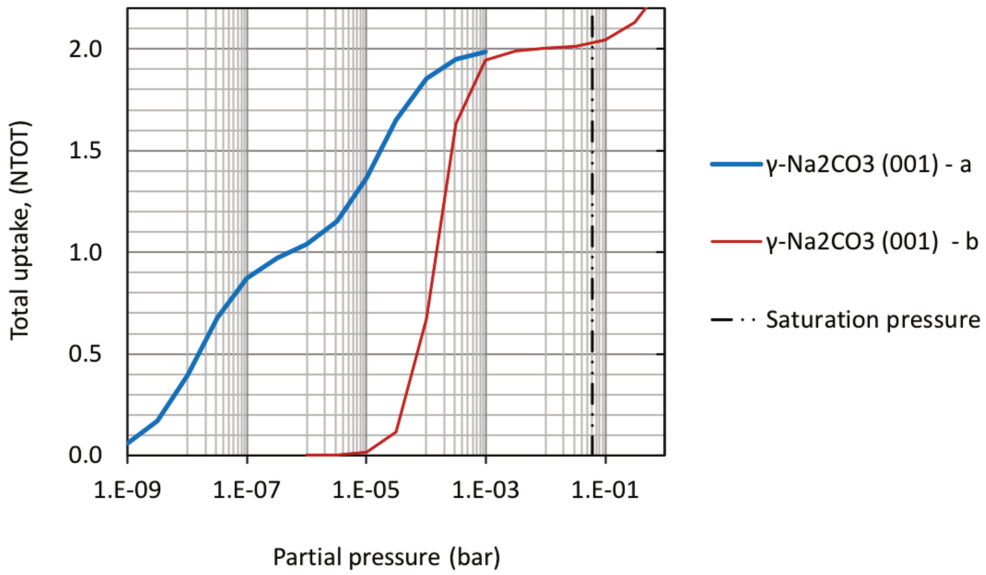

Figure 5-14 Comparison between adsorption isotherm of I_2 (g) on γ-Na_2CO_3 (001)-a and γ-Na_2CO_3 (001)-b surfaces at 373.15 K.

5.4.4 HI and H_2O adsorption on γ-Na_2CO_3 (001) surface

5.4.4.1 HI adsorption

HI could be formed in the SFR containment building during an SA following the sodium ejection and combustion due to either NaI thermal decomposition, or reaction of I_2 with HI [21]. The results of the interactions between Na2CO3 (001) surface and HI in gas phase are reported in this section.

The DFT computed value of H-I bond length in gas phase is 1.63 Å, which is in good agreement with the literature value of 1.61 Å. On the ideal Na2CO3 (001) surface, the associated H and I atoms adsorb in three stable configurations. The adsorption energies (ΔEads, eV) are -1.9825 eV, -1.7908 eV, and -1.6833 eV. This DFT study suggests that the ideal Na_2CO_3 (001) surface reacts very strongly with HI. In all three adsorption geometries, I atom is adsorbed to the Na atom with a bond length of 1.0025 Å, 1.0049 Å, 1.01250 Å. In the most stable configuration, iodine atom is bonded to the nearest Na atom, which permits a stabilizing attraction

between Na and O. The calculated adsorption energy for dissociation of HI molecules on the surface is positive hence endothermic in nature.

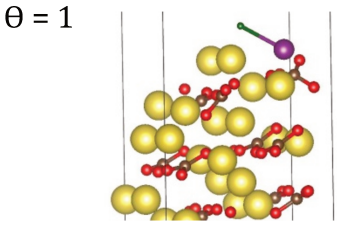

Figure 5-15 Front view of the adsorption of HI molecule on the bare Na_2CO_3 (001) surface. Yellow, Na; red, O; brown, C; purple, I; green, H.

Table 5-7 Adsorption energies of HI on Na_2CO_3 (001) in three structural configurations.

Configuration	Adsorption energy, eV
A	-1.9825
B	-1.7908
C	-1.6833

The partial pressure of HI inside the containment of an SFR during an SA will be significantly reduced in presence of the ideal Na_2CO_3 (001) surface. This strong affinity of HI for the ideal Na_2CO_3 (001) surface can be a result of polar HI molecule and the presence of cations on the Na_2CO_3 (001) surface, which attracts the electronegative iodine atoms toward it.

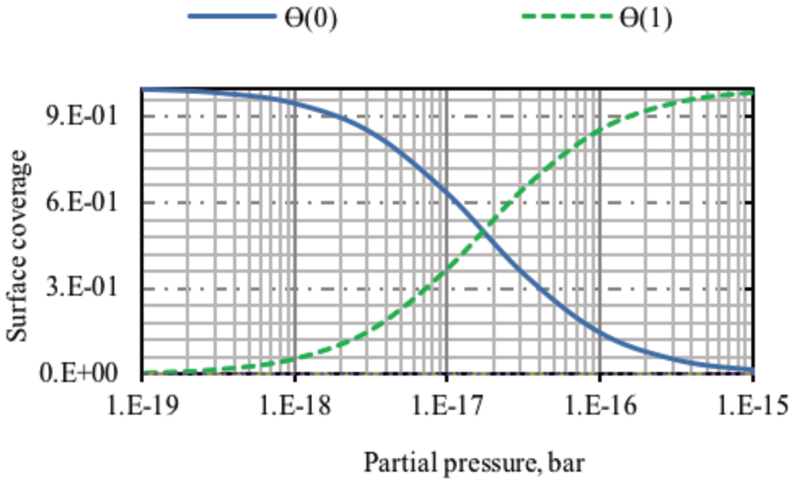

Figure 5-16 Evolution of partial pressure of HI as a function of surface coverage at constant temperature on bare Na_2CO_3 (001) at T = 323 K.

The relationship between evolution of bare surface and singly occupied surface at 323 K is presented in Figure 5-16. Adsorption of the first molecule of HI is highly favourable even at low partial pressures of HI. The transition of singly occupied surface to bare surafce occurs at a partial paresures of HI of 3.16×10^{-17} bar.

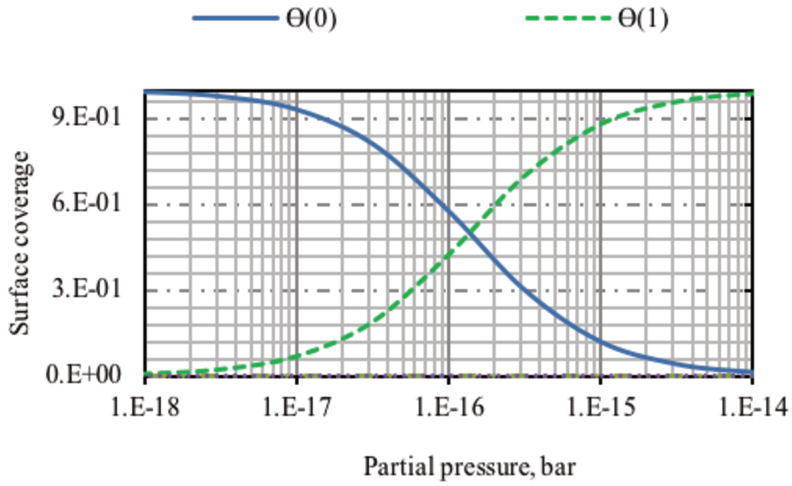

Figure 5-17 Evolution of partial pressure of HI as a function of surface coverage at constant temperature on bare Na_2CO_3 (001) at T = 373 K.

At 373 K (Figure 5-17), the transition from singly occupied surface to bare surface occurs at HI partial pressure of 3.16×10^{-16} bar while at 423 K (Figure 5-18), the transition occurs at 1.10×10^{-14} bar.

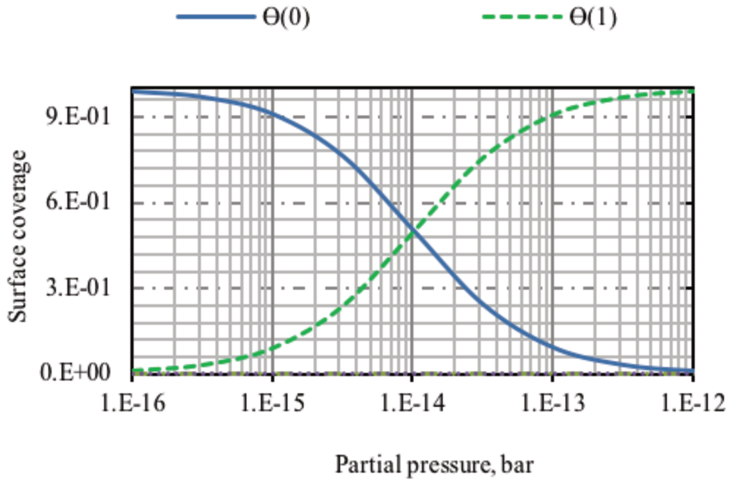

Figure 5-18 Evolution of partial pressure of HI as a function of surface coverage at constant temperature on bare Na_2CO_3 (001) at T = 423 K.

5.4.4.2 H_2O adsorption

Six configurations of H_2O adsorbed over Na_2CO_3 (001) surface were studied. The optimized adsorption structural parameters and adsorption energies (ΔEads, eV) for H_2O adsorbed on (001) surface of Na_2CO_3 are given in Table 5-8.

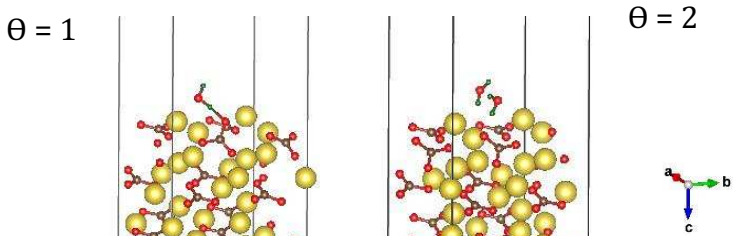

Figure 5-19 The optimized slab model of Na_2CO_3 (001) with H_2O molecule on the top of it. Yellow, Na; red, O; brown, C; purple, I; green, H.

The calculated H-O bond lengths in the adsorbed H_2O molecule for configurations A and B are 0.97 and 0.99 Å, respectively, which are slightly longer than the gas phase optimal value of 0.97 Å. The calculated ΔE_{ads} for the most stable configuration A is -0.7548 eV. The adsorption energy for the second adsorption was found to be -0.9115 eV. The adsorption structure is illustrated in Figure 5-19. The dissociation of water molecule on the ideal surface of Na_2CO_3 (001) remains unfavorable.

Table 5-8 Adsorption energies of H_2O on Na_2CO_3 (001) in six structural configurations.

Adsorbate	Energy of adsorption, eV
H_2O	-0.7547
H_2O- H_2O	-0.9124

Figure 5-20 shows the plot of θ against partial pressure of water vapor at T = 353 K. The ratio of singly occupied sites to total available sites is negligible. The transition from singly occupied sites to doubly occupied surface occurs at a partial pressure of water vapor of 5.2×10^{-5} bar. However, the surface turns from doubly occupied to bare surface at partial pressure of 3.16×10^{-3} bar.

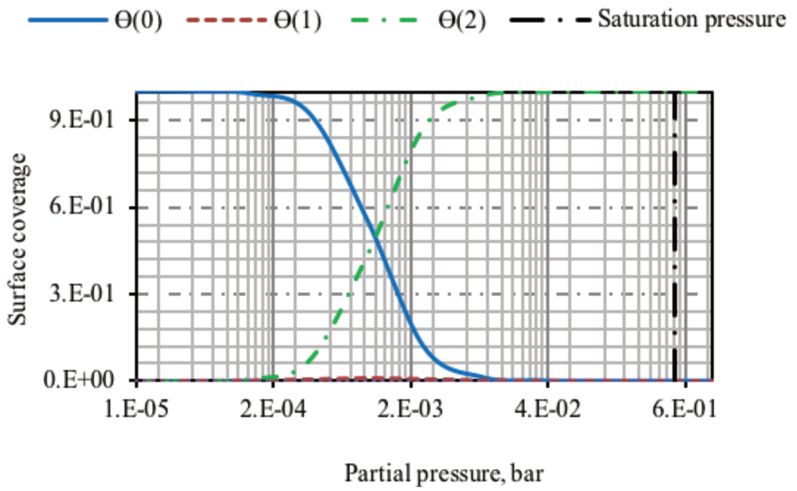

Figure 5-20 Evolution of partial pressure of water vapor as a function of surface coverage at constant temperature on bare Na_2CO_3 (001) at T = 353 K.

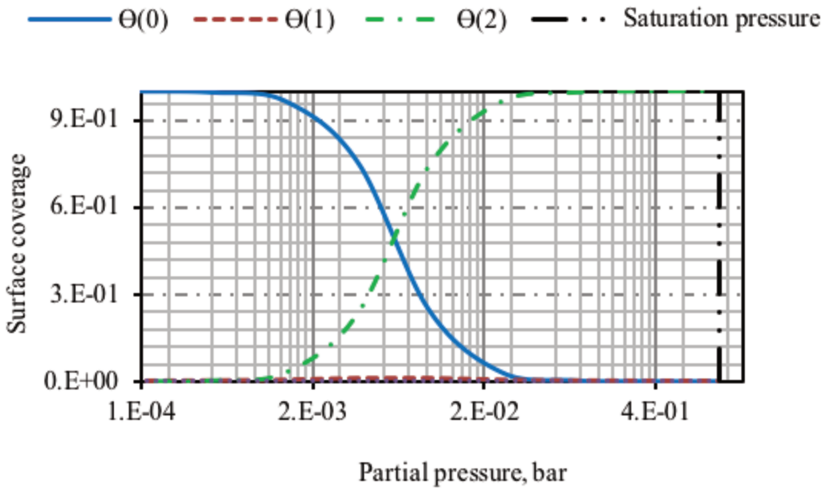

Figure 5-21 Evolution of partial pressure of water vapor as a function of surface coverage at constant temperature on bare Na_2CO_3 (001) at T = 373 K.

At 373 K, the transition from singly occupied to doubly occupied sites occurs at a partial pressure of water vapor of 2.75×10^{-4} bar, while the transition from doubly occupied sites to bare surface at 1.10×10^{-2} bar.
Similar behavior was observed at 423 K (see Figure 5-22) where the transition from doubly occupied surface to bare surface occurs at 1.7×10^{-1} bar.

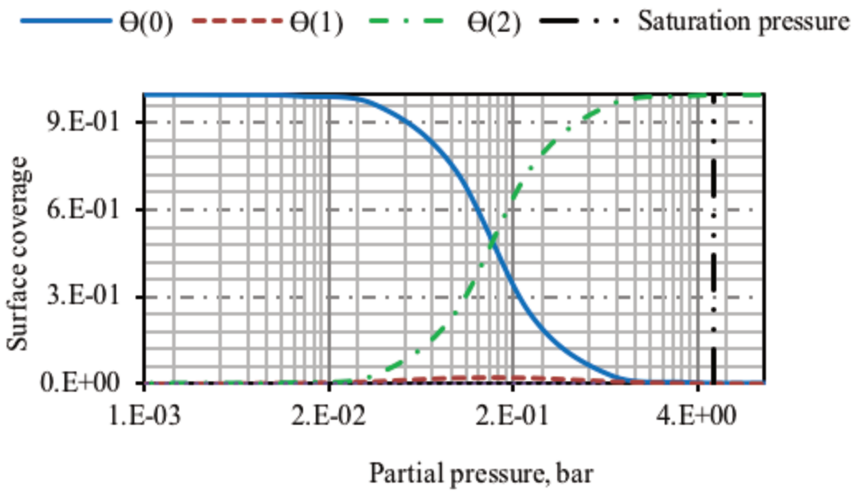

Figure 5-22 Evolution of partial pressure of water vapor as a function of surface coverage at constant temperature on bare Na_2CO_3 (001) at T = 353 K.

5.5 Discussions, conclusions, and perspectives

The relative stability of different γ-Na_2CO_3 surfaces has been investigated using the DFT-D3 method. The two most stable surfaces have been found to be γ-Na_2CO_3 (001) and (110) respectively. A preliminary investigation was carried out on surface defects, it was found that none of the studied surface defects are stable.

On both surfaces, the associative adsorption of I_2 (g) is thermodynamically favored (exothermic) while the dissociative one is endothermic, at 0 K.

A computational model has been developed to calculate the adsorption isotherm (uptake of I_2 (g) by the γ-Na_2CO_3 surfaces) at any temperature. It was established that the surface (110) adsorbs I_2 (g) more efficiently than (001) at partial pressures close to the saturation pressure of I_2 (g). It is worth recalling here that gas phase molecules were added on the surface in steps. The maximum iodine uptake efficiencies were reported to be one molecule per 47Å^2 for (001) and one molecule per 32Å^2 for (110). However, the γ-Na_2CO_3 (001) surface is more reactive at a lower partial pressure of I_2 (g).

From the nuclear safety point of view, this adsorption reaction will reduce the probability of release of I_2 (g) outside the containment building. Indeed, based on the assumption that Na_2CO_3/I_2 ratio is reasonably high, according to our calculations, the residual partial pressure of I_2 (g) can be expected to be strongly lower than 2×10^{-4} bar at equilibrium at 373.15 K.

However, according to the hypothesis of existence of strong kinetic limitation of the transformation of Na_2CO_3(001)-a to Na_2CO_3(001)-b, one can expect the former surface to play major role in conditions of our experimental investigations, see

Chapter 6. In this assumption, one can expect the uptake of iodine 100 times higher than the one due to the presence of Na_2CO_3(001)-b, as explained before.

Perspectives for theoretical chemistry studies

- As a first enhancement of the theoretical, analytical model presented, the increment of Gibb's energy of the condensed phase concerning temperature shall be considered. One possible way of including them is the phonon calculations.

- A better characterisation of sorbent surface shall be considered. High level ab-initio calculations such as single point coupled cluster calculations (CCSD(T)) for a reduced surface prototype is expected to give more accurate description of adsorption processes. Similar calculations have shown a considerable enhancement of the reactivity of CO_2 on MOFs [108].

Chapter 6 Experimental research of the interactions between Na_2CO_3 and I_2

6.1 Surface characterisation

6.1.1 SEM

For all Na_2CO_3 (s) sorbent preparation (powder, aerosol deposit, and pellet) the morphologies of their surfaces were investigated using SEM. Depending on the nature of the surface (powder, aerosol deposit, or pellet) and especially on their homogeneity, different magnification rates were investigated.
Figure 6-1 shows the corresponding images generated by SEM. Images (a-d) for powder and aerosol deposit, respectively shows some morphological features such as edges, pits, and empty spaces which helped to have a better three-dimension picture of the surfaces. However, no such information could be retrieved in case of the pellet; because of its high density leading to a quasi-homogeneous surface.
Figure 6-1 (a-b), relative to Na_2CO_3 powder, shows that the geometrical particle size ranges roughly from 50 µm to 500 µm, and the particles are irregularly shaped. The particles in the SEM image are rather homogeneously deposited but significant macro porosities between the particles are observed.
Figure 6-1 (c-d), relative to Na_2CO_3 aerosol deposit, shows tha, compared to the powder, the particle density is higher and the size of the macro porosities smaller. The average geometrical particle size was estimated to be about 8 µm.
In this sense, the particle size of aerosol deposits can be safely considered as more representative of sodium combustion particles generated in the containment of a SFR experiencing a SA than the powder.

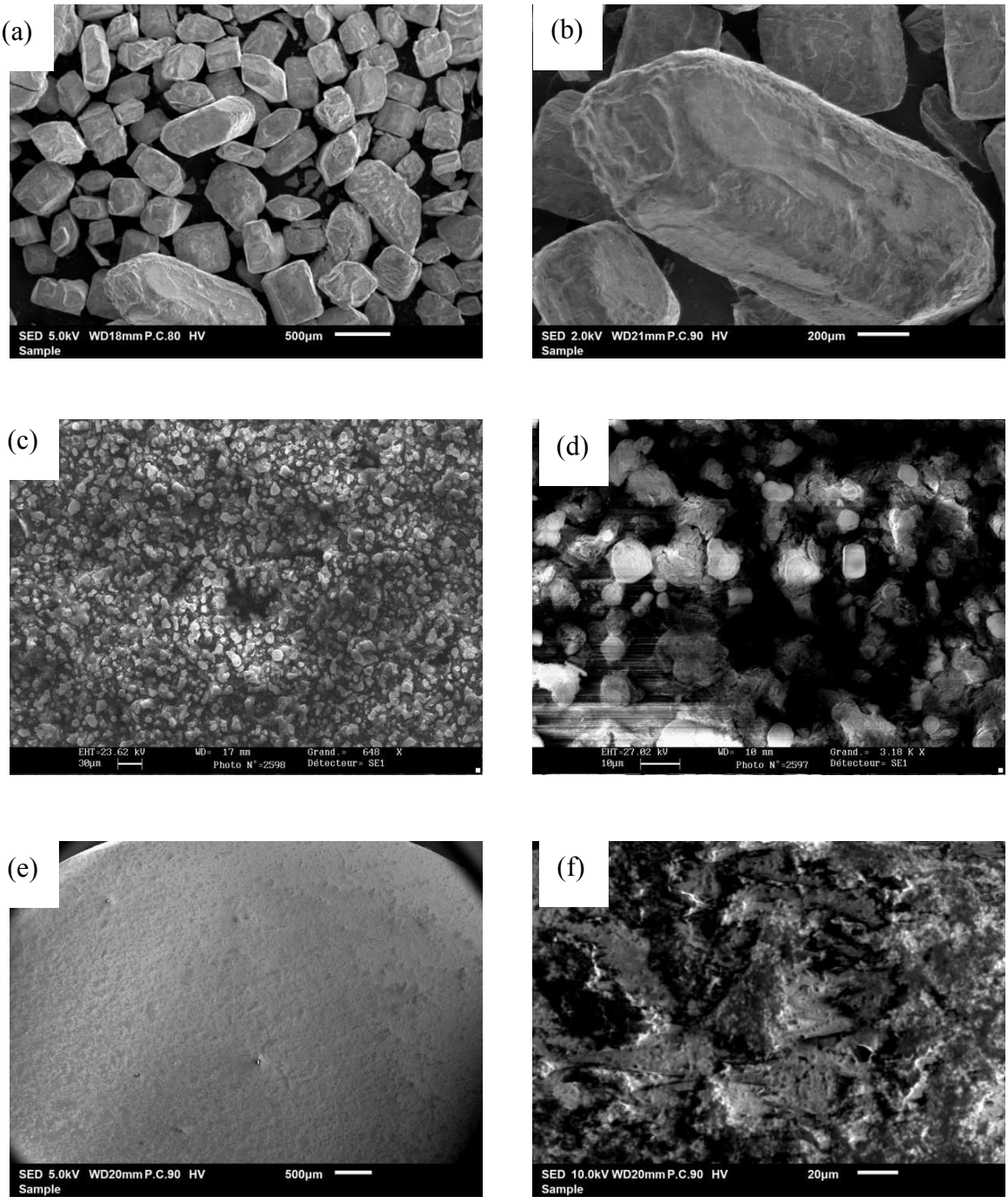

Figure 6-1 Scanning electron microscopy images of Na_2CO_3 sorbent samples of three distinct physical forms a-b) powdered c-d) aerosol deposits e-f) pellet.

6.1.2 BET

Several BET analyses were performed to measure the total specific surface area of Na_2CO_3 powder, aerosol deposit, and pellet samples. The measured surface area was found to be 0.60 m^2g^{-1} and 0.30 m^2g^{-1} respectively for the powdered and pellet sorbent

sample, respectively. For Na_2CO_3 aerosol deposit samples no data were obtained because of the too low amount of deposits obtained leading to a specific surface area under the detection limit of the instrument, i.e., lower than 0.1 m^2g^{-1} (provided by the manufacturer). In this case, the estimated surface area is within the error limits of the instrument provided by the manufacturer hence not very accurate. As only single measurements were performed for each kind of Na_2CO_3 samples, there remains a huge uncertainty in the surface area quantification. However, from the low values of surface areas measured, two conclusions can be drawn:

- The Na_2CO_3 powder and pellet particles are non-porous in nature
- The ultimate reaction rate limiting step at the grain surface shall be the diffusion of gas within the pores of the grain

This small surface area of the Na_2CO_3 sorbent measured by the BET technique is in agreement with the compact aggregates seen on the SEM images.

6.1.3 ToF - SIMS

The characterization of the interaction of I_2 (g) with sodium carbonate sorbent was performed by ToF-SIMS measurements in statics mode generating surface chemical mass spectra. Figure 6-2 shows the comparison of chemical characteristics of the positive ToF–SIMS spectra of pure Na_2CO_3 powdered samples specimens before any interaction with I_2 (g) (top). In the same figure, the bottom two images show the spectra of the sample which was exposed to I_2 (g) for about three hours at 373.15 K. The top image shows peaks of Na oxide, hydroxide and ethylene ions. In the two bottom images, in addition to pure Na_2CO_3 powdered samples, some fragments with Na and I are clearly visible. Thus, it can be concluded from the ToF-SIMS analyses that the Na_2CO_3 surface had interacted with I_2 (g). Unfortunately the ToF-SIMS measurements are only qualitative and doesn't allow to quantify the I_2 (g) uptake by Na_2CO_3 surfaces. This will be done by kinetics measurements in FTR and by IBBCEAS (see Section 6.2).

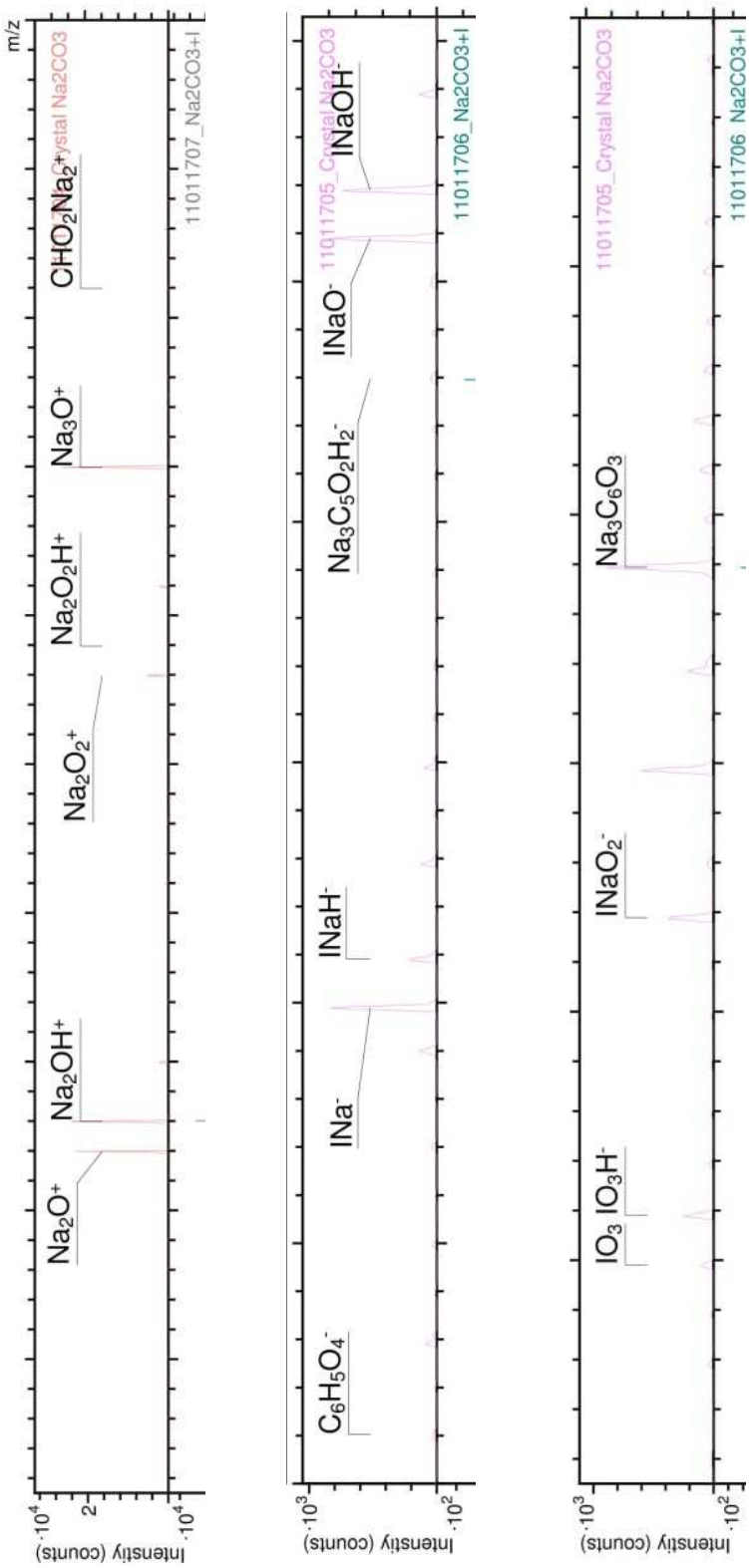

Figure 6-2 Comparison of the positive survey ToF-SIMS spectra of Na_2CO_3 samples (a) before, left image and (b) after, two images on the right reaction with I_2 for three hours at 373.15 K. The horizontal axis represents m/z.

6.2 I_2 (g) adsorption on Na_2CO_3 (s) surfaces

In this section the overall results related to I_2 (g) adsorption on sodium carbonates will be presented and discussed. It concerns analyses and modelling of the experimental data on I_2 (g) adsorption kinetics and uptake efficiency issued from FTR and IBBCEAS facilities.

6.2.1 I_2 capture by Na_2CO_3 powder: uptake run

Several parameters that might have impact on I_2 (g) adsorption kinetics and uptake on the non-porous Na_2CO_3 sorbent were investigated. There are, as already mentioned previously:

- Reaction temperature, i.e., FTR temperatures
- Iodine partial pressure, i.e., permeation tube temperatures and the carrier gas flow rate
- Sodium carbonate surface mass and specific area

The above mentioned parameters were varied in the range of expected in-containment conditions (representative Na/I molar ratios, I_2 (g) partial pressure and reaction temperatures)(see table 6.1).
A set of experiments, where each parameter was varied step by step, were performed. The corresponding results and analyses are presented in this section. Given that within the anticipated SA boundary conditions, the kinetics of the I_2 (g) adsorption reaction should not be too fast, the equilibrium concentration of gaseous iodine corresponding to the saturation of the sodium carbonate surface should take time and be recorded given the sensitivity limits of the instruments used. Thus the evolution of the number of I_2 (g) moles adsorbed on the sorbent could be indirectly calculated by measuring the evolution of the number of I_2 (g) moles flowing through the FTR as a function of time without and with sodium carbonates. A typical evolution of the accumulated number of I_2 (g) moles trapped in the bubbler in presence (red dots)or absence (blue dot) of Na_2CO_3 sorbent is shown in Figure 6-3. Without carbonates the evolution against time of the number of moles in the bubbler, representative of the generated flow rate if I_2, is linear. At the beginning of the kinetic experiment (FTR with sorbent), the molar iodine flow rate is lower than that measured during the calibration experiment (FTR without carbonates), ($Q_{I2} = 10^{-7}$ mole min^{-1}). We recall here that the flow rate of I_2 at the exit of the FTR is the derivative as a function of time of the amount of iodine accumulated in the bubbler (in moles of I_2) over time. As shown in Figure 6-3, the flow of iodine trapped in the

bubbler increases slowly until it reaches almost the same value as that is measured during calibration run. As it will be detailed here after, unfortunately, these measurements, though interesting, don't allow determining the I_2 adsorption kinetics rate on carbonates. A detailed interpretation of the uptake data is presented in the coming section.

In this section, the effect of changing the boundary conditions in the range of expected in-containment conditions was investigated. In the absence of pore diffusion (explained in Section 6.1.2), the principal variables that are expected to determine the rate of I_2 capture by a given sorbent are given below; and their range are shown in Table 6-1.

- Reaction temperature
- Mass of sorbent (or specific surface area); and
- I_2 partial pressure

Table 6-1 Range of boundary conditions studied in the FTR.

Reaction temperature	Mass of sorbent	I_2 generation temperature; (associated partial pressure)
100°C and 150°C	Between 36 mg and 8 g	Between 70°C and 130°C; (3.73×10^{-07} and 3.38×10^{-06} bar)

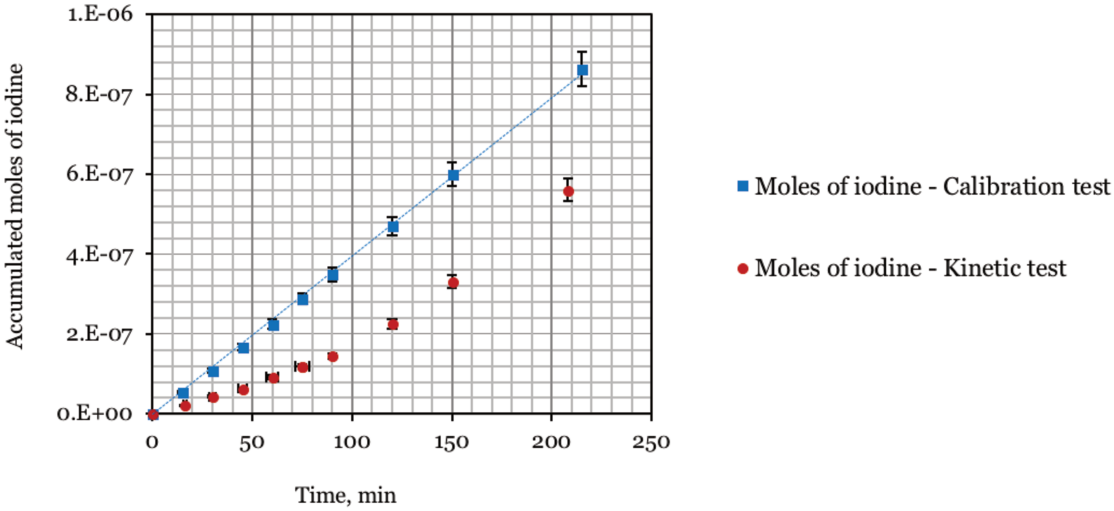

Figure 6-3 Moles of I_2 trapped in bubbler. Calibration experiment which is conducted with empty FTR (dataset in blue) compared with the kinetics experiment conducted with Na_2CO_3 sorbent placed inside the FTR (dataset in red). Error bars ($t = 0 \rightarrow 50$ min) are within the size of the marker.

The convention for experimental boundary conditions used in this work follows the following style: (iodine permeation tubes temperature; carrier gas flow; reaction

temperature; mass of sorbent). For example, (100°C; 0.4 NL min^{-1}; 100°C) would imply an experiment conducted when iodine generation temperature was set at 100°C with 0.4 NL min^{-1} of carrier gas flow, and, the reaction temperature set at 100°C.

6.2.1.1 Qualitative analysis of I_2 uptake data

As said earlier, at the beginning of the kinetic experiment, in principle, all the active sites on sorbent surface are capable of adsorbing iodine (depending on thermodynamic condition). As seen in Figure 6-3, from time zero the quantity of iodine trapped in the bubbler is lower compare to that measured for the experiment performed without carbonates. As the graph shows the accumulated iodine measured as a function of time, the derivative, calculated at a given time, is the flow rate (mole min^{-1}) of iodine at the exit of the FTR and trapped in the bubbler. For the experiment without carbonates, the derivative is almost constant, meaning that the flow rate of iodine is stable. The slope of the straight line gives the flow rate of iodine generated at the exit of the iodine generator and entering the FTR (assuming no iodine losses in the PFA tubes and the FTR). When the carbonates are introduced in the FTR, the derivative is nearly zero at the beginning of the experiment, then is increasing to finally reach the same value as for experiments performed without carbonates (see also Figure 6-4).
Several physical and chemical processes can be put forward in the interpretation of these experiments. In the beginning of the kinetic experiment, the uptake flow of iodine by carbonates may be limited by the diffusion of iodine towards the active surface. As soon as the iodine is introduced in the FTR, I_2 molecules will be capture by active sites and after a while the active sites on the sorbent surface are getting nearly exhausted resulting in the slope of the kinetics run being comparable to the calibration run. This regime corresponds to the equilibrium. In this explanation, all the sites are considered as equivalent from the point of view of their accessibility by iodine in the gas phase. From an experimental point of view it is clear that this is not true. Depending on the nature of the bulk (powder, pellet or deposits on a substrate) exposed to I2, the process will be limited by the diffusion of I2 towards all the active sites. All these described processes occur with different characteristic times and it is almost impossible to distinguish them from our measurements.

To summarize, the possible rate-limiting steps for I_2 adsorption on Na_2CO_3 could be:

- Diffusion in gas phase toward the surface and/or between the grains of sorbent; and
- Diffusion in solid phase within the grain of sorbent

The diffusion within the grain is a function of the grain porosity and grain pore size. The specific surface measured by BET analysis was found to be very low (~0,6 m^2/g) highlighting that there is an absence of porosity in the samples. Secondly, the diffusion between the grains depends on the packing of the grains. To study the effect of packing of the grains, three different physicals forms of the sorbent were studied, as explained in Section 4.2.

The main relevant experimental results are presented hereafter.

6.2.1.2 Reproducibility of the experiments

Several experiments were conducted at the same boundary conditions (iodine partial pressure; reaction temperature; mass and surface of sorbent) to check reproducibility of the measurements. For the kinetic runs, in addition to the sources of discrepancies already mentioned for calibration runs (I_2 vaporization flux, deposition on the walls of the reactor and associated gas lines, UV spectrometry measurement uncertainties), discrepancies between similar experiments might come from the sorbent active site accessibility. Site accessibility differs for the same mass of sorbent because of the factors like particle shape and packing (and the surface area). As the estimation of each of this source of uncertainty would have required a lot of tests, a statistical approach was chosen to get the global uncertainty range.

Figure 6-4 shows the result of the duplicated experiment. Figures (a) and (b) show the raw data obtained from the FTR facility; figure (c) shows a plot of capture efficiency, calculate using Equation 4-13 page 78) of the sorbent as a function of time. It should be noted that the fluctuations in the capture efficiency (especially in the beginning of the experiment) arise due to the fact that the capture efficiency is a time derivative. It can be seen from Figure 6-4 (c), given the limitation of the technique, the results are quite similar. A series of tests were performed in the same way but for different boundary conditions. Each time, the results were found to be quite similar implying that the measurement technique can be considered reliable enough for reproducibility. As a matter of fact, the experiments mentioned in this thesis afterwards were not duplicated any more.

Duplicated experiment:

Temperature of I_2 generation	FTR temperature	Mass of sorbent
115°C; PP = 3.06×10^{-06} bar	100°C	3.5 g

The following figure shows the raw experimental data and the calculated capture efficiencies by the sorbent as a function of time. In the beginning of the experiment (t = 0 to about 20 min), the capture efficiency is 100%, it is not shown in the figure. It is worthwhile to notice that the used iodine detection technique is not sensitive enough to detect very low concentrations of iodine, especially expected in the beginning of the experiment. Therefore it would not be just to say that the capture efficiency is 100% but rather close to 100%.

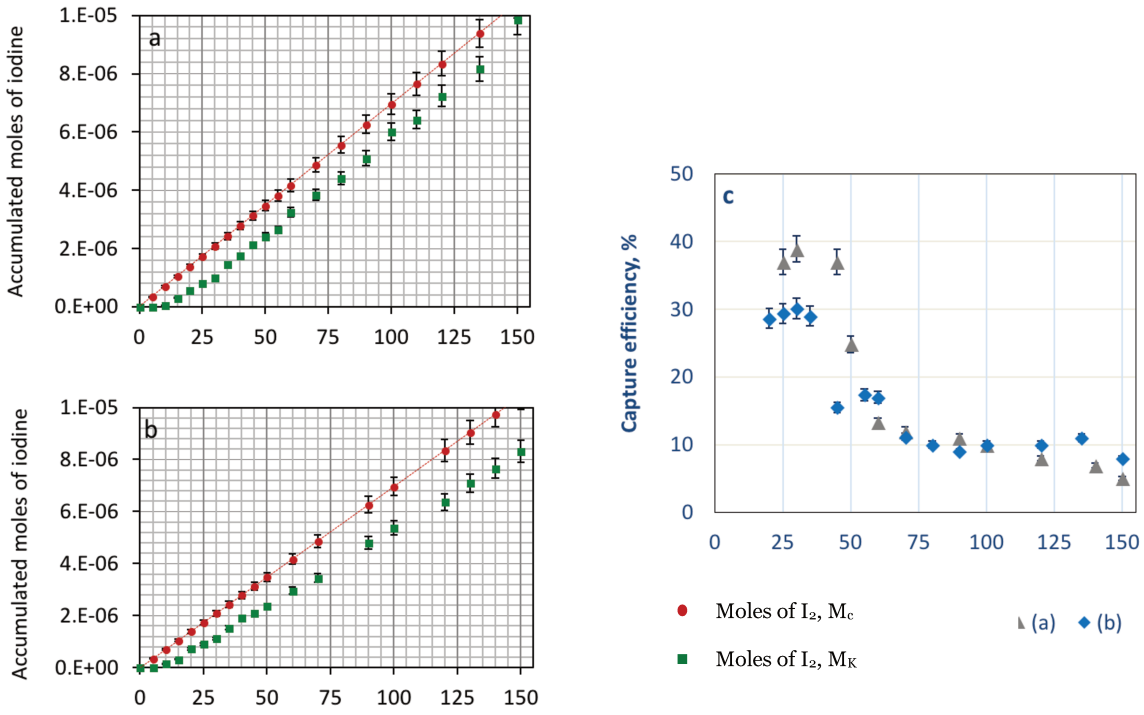

Figure 6-4 Figures (a) and (b) showing the raw data obtained by experiments conducted in FTR facility, performed at (115°C; 0.4 NL min^{-1}; 100°C). Figure (c) shows the comparison of calculated capture efficiency by 3.5 g of powdered Na_2CO_3 sorbent at 115°C (a) and 100°C (b). Time (minutes) is plotted on the x-axis.

All the duplicated tests were found to give quite reproducible results for initial iodine concentrations varying from 7.5 10^{-9} to 2 10^{-7} M. Largest discrepancies were observed at the very beginning of the uptake experiments, where for very efficient capture by Na_2CO_3 (close to 100%), the iodine amount flowing down to the bubbler is very low.

6.2.2 Key parameters impacting I_2 adsorption

6.2.2.1 Reaction temperature

Compared experiments

I_2 partial pressure	**FTR temperature**	Mass of sorbent
3.7×10^{-07} bar (70°C; 0.4NL min^{-1})	100°C	1 g
3.7×10^{-07}bar (70°C; 0.4NL min^{-1})	150°C	1 g

The effect of the FTR temperature (i.e., reaction temperature) on I_2 adsorption by sodium carbonates was studied by varying its temperature between 100°C and 150°C while keeping the iodine partial pressure and the mass of sorbent similar. The effect on the variation of I_2 capture efficiency by Na_2CO_3 powder as a function of time is shown in Figure 6-5 (c). At FTR temperature of 100°C, no I_2 was detected in the bubblers for the first 30 min, implying 100% uptake. After 30 min, the number of active sites starts getting exhausted and the uptake is reduced to about 60% and stalled almost for 40 minutes at this value.

For FTR temperature of 150°C, the surface showed a weaker (quantitatively) interaction with I_2 right from the beginning of the experiment. The uptake efficiency was 40% for the first 15 minutes, afterwards, it stalled to a value of around 30% for about 70 minutes.

A complete saturation of the surface could not be observed for the entire duration of the experiment for both the experiments.

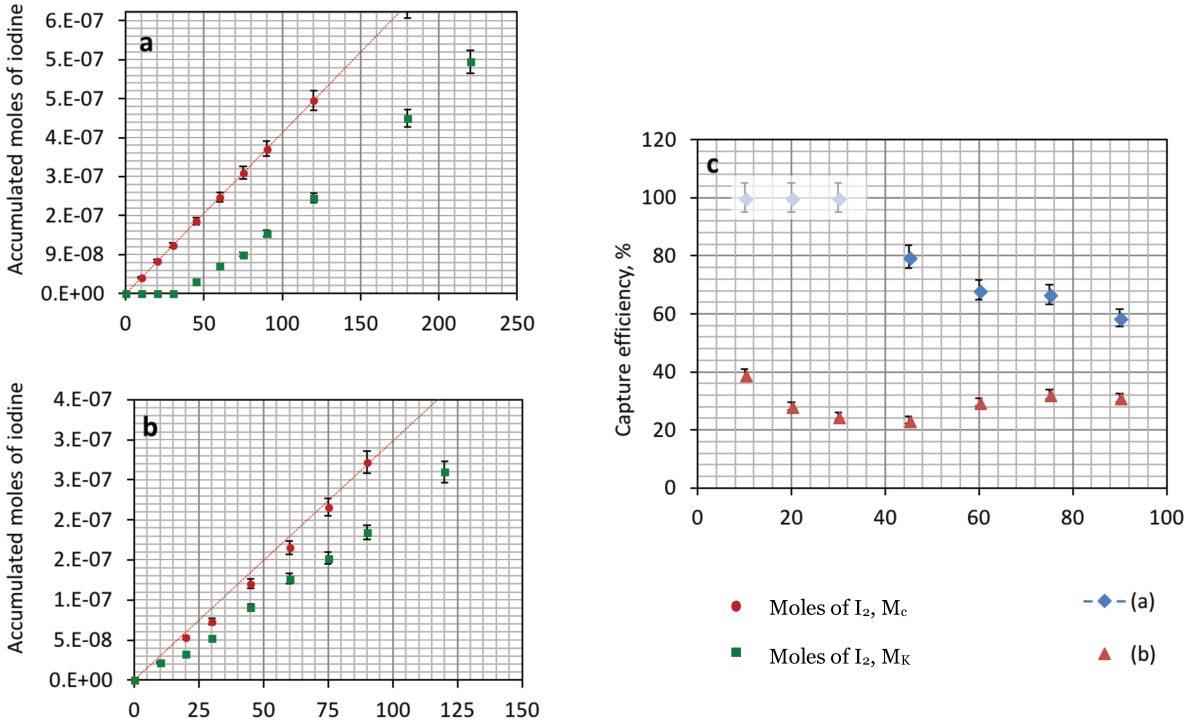

Figure 6-5 Figures (a) and (b) show the raw data obtained from the experiments conducted in the FTR facility at respectively 100 and 150°C. Figure (c) shows a comparison of capture efficiencies of Na_2CO_3 powdered sorbent for two distinct reaction temperatures (in blue at 100°C in red at 150°C) by 1 g of powdered Na_2CO_3 sorbent. Experiment performed at (70°C; 0.4 NL min^{-1}; 100°C).Time (minutes) is plotted on the x-axis.

Increasing the reaction temperature from 100 to 150°C thus led to significantly decrease the capture efficiency of I_2 by Na_2CO_3, especially during the first period of the experiment when the available adsorption sites are maximum.

6.2.2.2 Mass of sorbent

Two sets of experiments were performed with the aim of comparing the behaviour of sorbent for two different mass (keeping the rest of the boundary conditions same). One set of experiments was conducted using aerosol deposited sorbent (Figure 6-6) and the other with powdered sorbent (Figure 6-7). Details of the two sets of experiments are presented below.

Conclusions and perspectives

Set 1: Figure 6-6 (Aerosol deposit sorbent)

I_2 partial pressure	FTR temperature	**Mass of sorbent**
3.7×10^{-07}bar (70°C; 0.4NL min^{-1})	100°C	100mg
3.7×10^{-07}bar (70°C; 0.4NL min^{-1})	100°C	70mg

Set 2: Figure 6-7 (Powdered sorbent)

I_2partial pressure	FTR temperature	**Mass of sorbent**
3.7×10^{-07}bar (70°C; 0.4 NL min^{-1})	100°C	7.38 g
3.7×10^{-07}bar (70°C; 0.4NL min^{-1})	100°C	0.91 g

In both the cases, the data shows an intuitive trend based on a simple rationale for adsorption where the quantity of adsorbed species should be proportional to the accessible active sites i.e., mainly surface sites.

In Figure 6-6 the capture efficiency is plotted against time for two different mass of sorbents (aerosol deposit type). The result suggests that the available surface area is a critical factor to maximize the capture efficiency as was previously predicted. The capture efficiencies varied largely with time, as expected. At first, all the active sites are capable of adsorbing incoming I_2 gas molecules, resulting in high capture efficiencies (can be seen in the figure). With the passage of time, the sites on the top of the sorbent begin to saturate, making the capture efficiencies drop. This time period depends on the surface area of the sorbent. Figure 6-7 (a) shows the trend of capture efficiency by powdered sorbents. The two experiments were conducted at same conditions (70°C; 0.4 NL min^{-1}; 100°C), but mass of sorbent was varied. In case of higher mass (100 mg), the capture efficiency as a function of time is higher compared to 70 mg of sorbent till it falls down to zero leading to a higher amount of I2 adsorbed on carbonates. For lower mass, the capture efficiency approaches zero after about 150 minutes of the experiment; implying exhaustion of active sites. However, 100 mg of sorbent remains active even after 180 minutes.

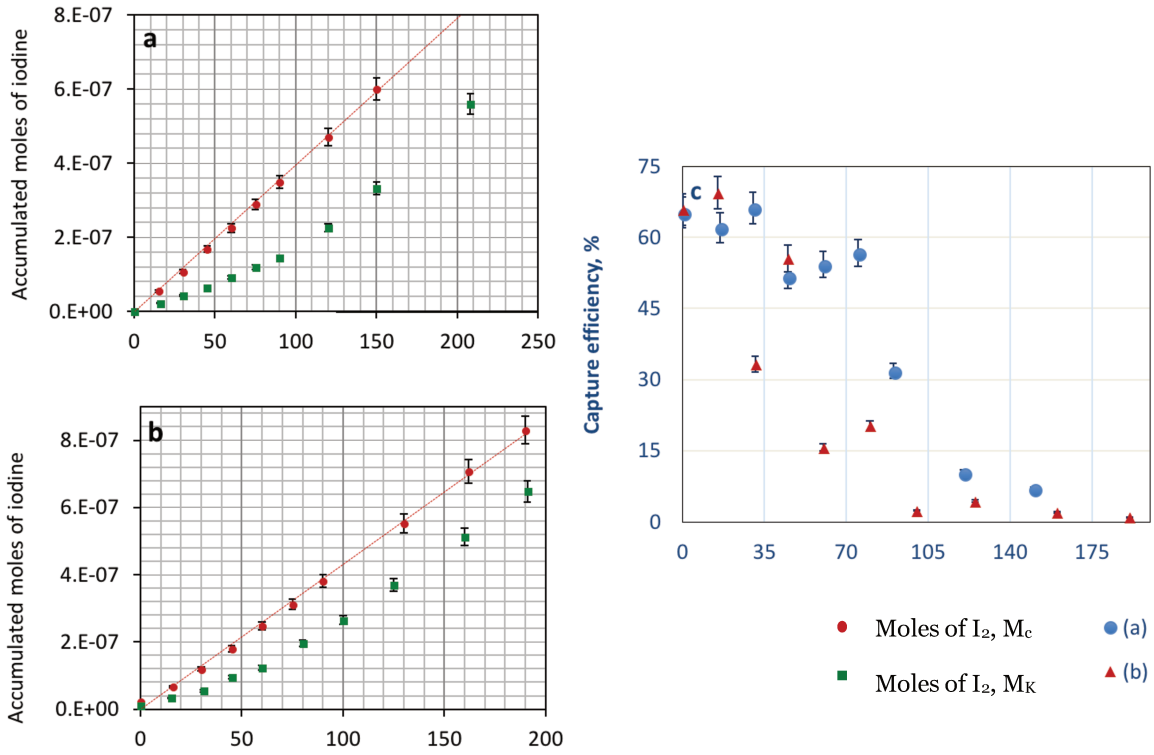

Figure 6-6 Figures (a and b) showing raw data of the experiment conducted at (70°C; 0.4 NL min^{-1}; 100°C); mass of aerosol deposited sorbent is 100 mg and 70 mg for experiment (a) and (b), respectively. Figure (c) shows the calculated capture efficiency by powdered Na_2CO_3 sorbent for two different masses (in blue 100 mg and in red 70 mg). Time (minutes) is plotted on the x-axis.

Furthermore, the role of sorbent packing densities was investigated by conducting the experiments with powdered sorbent, showed in Figure 6-7. The figure shows the comparison between capture efficiencies by 7.38 g of powdered sorbent and considerable lower mass, 0.91 g of the sorbent. As predicted, the sorbent with eight times larger surface area shows capture efficiencies of around 50% even after two hours of reaction, while the sorbent with lesser mass (0.91 g) proceed toward complete saturation after 75 minutes into the reaction.

Conclusions and perspectives

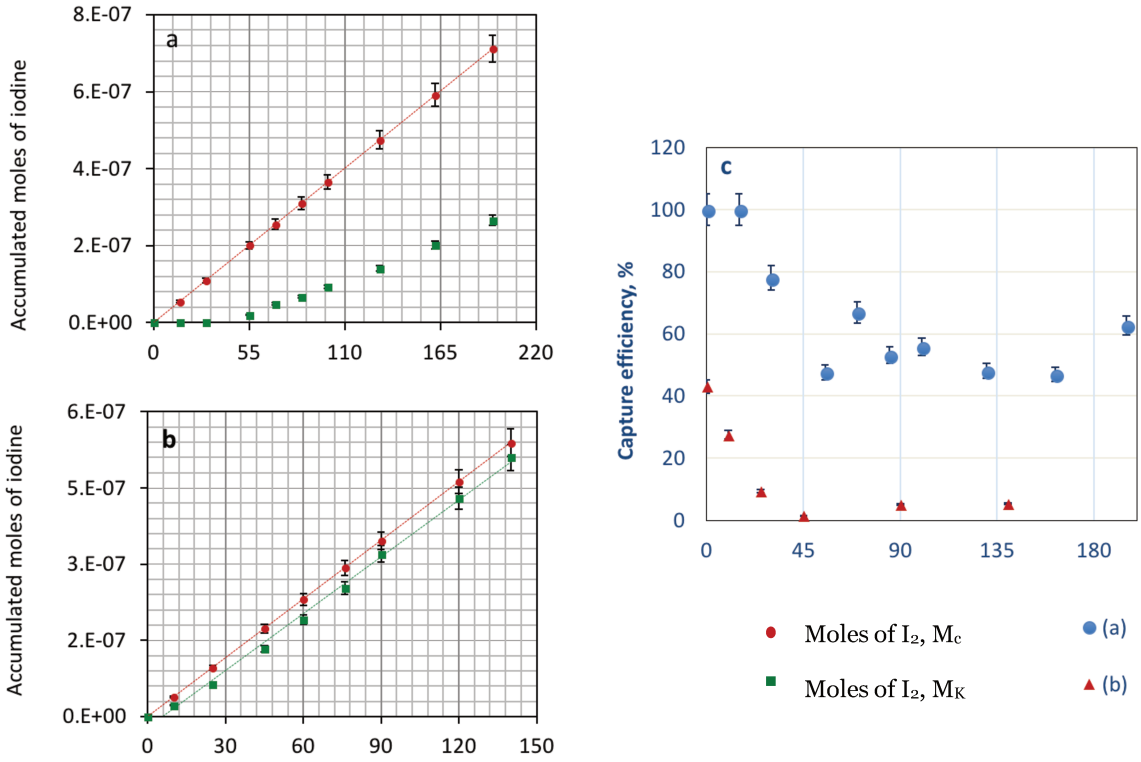

Figure 6-7 Figures (a and b) showing raw data of the experiment conducted at (70°C; 0.4 NL min^{-1}; 100°C); mass of sorbent is 7.38 g and 0.9 g for experiment (a) and (b), respectively. Figure (c) shows the calculated capture efficiency by powdered Na_2CO_3 sorbent for two different masses (in blue 7.38 g and in red 0.9 g). Time (minutes) is plotted on the x-axis.

As intuitively expected, by increasing the Na_2CO_3 powder mass while using similar range of initial iodine concentrations (thus increasing the Na/I ratio), a higher capture efficiency of I_2 was observed. For the higher sorbent mass, the sorbent saturation could not be reached within the 3 hour experiment. However, definitive conclusions could not be drawn as the different sorbent surfaces in these tests were not accurately determined.

Two experiments were conducted at prolonged duration of time (about 50 hours). The result is presented in Figure 6-8. It can be seen from the figure that at the beginning of the experiment, the calculated capture efficiency is maximum which decays with time. A plot of the raw experimental data is presented in Appendix A. In case of the experiment with 5 g of sorbent, a significant decrease in the capture efficiency cannot be seen from time 180 minutes to 1200 minutes. A similar behavior was observed for the experiment conducted with 3 g of sorbent where no significant decrease in capture efficiency was observed from time 350 minutes to 3100 minutes. With limited experimental information, a possible explanation of this trend can be the achievement of a chemical equilibrium between the sorbent surface and iodine flux. However, a complete saturation of the sorbent was not observed until the end

of the experiment. The primary reason could be high mass of sorbent combined with low partial pressure of iodine.

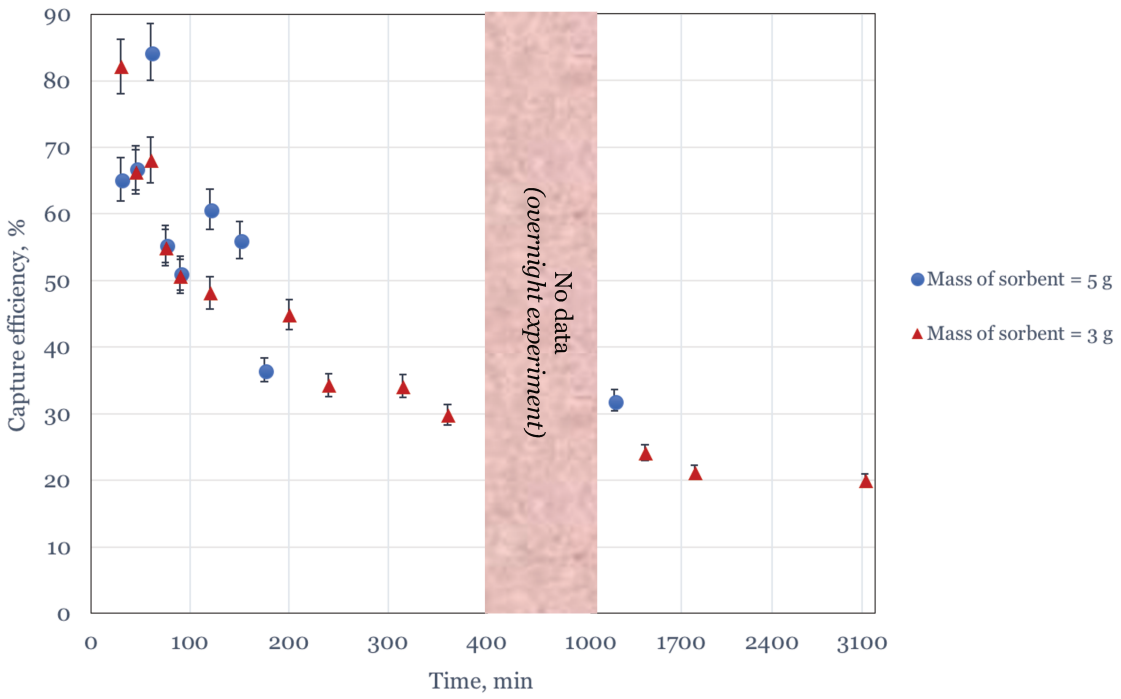

Figure 6-8 Figure showing capture efficiency by different mass of powdered Na_2CO_3 sorbent. The two experiments conducted at (70°C; 0.4 NL min^{-1}; 100°C).

A few experiments were performed using (a) compressed pellet, and (b) rupture tube inside the FTR. Within the detection limit of the instrument used, no uptake of I_2 was observed for compressed pellet of sorbent (200 µg). This might be due to the fact that the pellet has considerably less surface area (0.5 cm diameter), implying fewer active sites at the surface in addition to negligible porosity which resulted in limiting transfer of iodine within the pellet.

Experiments with rupture tube inside the FTR: The idea behind using a rupture tube[19] was to force iodine flux to pass through the sorbent. The rupture tube, with powdered sorbent of about 5 g, was placed inside the FTR, along its horizontal axis. Similar behavior was observed compared to the sorbent placed in Teflon/glass cell. This confirms the assumption that iodine reaches within the depth of the sorbent, if placed in a Teflon/glass cell.

[19]A hollow tube of slightly less diameter than the FTR, made of a glass mesh.

6.2.2.3 Partial pressure of iodine

It is worth recalling here that partial pressure of iodine was varied inside the FTR in two different fashions.

- Changing the temperature of iodine permeation tubes which impacts the generation of iodine vapors from solid iodine crystals

- Changing the flow of carrier gas, which has impact on iodine mole fraction in the gas mixture

One set of experiments, one under each category, were conducted to study the impact of partial pressure of iodine on capture efficiency. The experimental boundary conditions are listed below.

Set 1: Figure 6-9

I_2 partial pressure	Reactor temperature	Mass of sorbent
3.2×10^{-07}bar (80°C; 0.4 NL min^{-1})	100°C	6.0 g
3.0×10^{-06}bar (115°C; 0.4NL min^{-1})	100°C	6.0 g

Figure 6-9 shows the confirmed intuitive trend of availability of active sites and incoming iodine gas molecules. It can be seen from Figure 6-9 (b) that in case of higher partial pressure (achieved with a permeation tube temperature of 115°C), the gradient of capture efficiency is higher and it becomes 46% after 200 minutes of the experiment. However, when the same mass of sorbent is exposed to a lower partial pressure of iodine (1.0 NL min^{-1}), the capture efficiency effectively remains constant for the entire duration of the experiment. Figure (b) shows the same trend. In case of lower partial pressure of iodine, the surface seems to be active for longer duration of time.

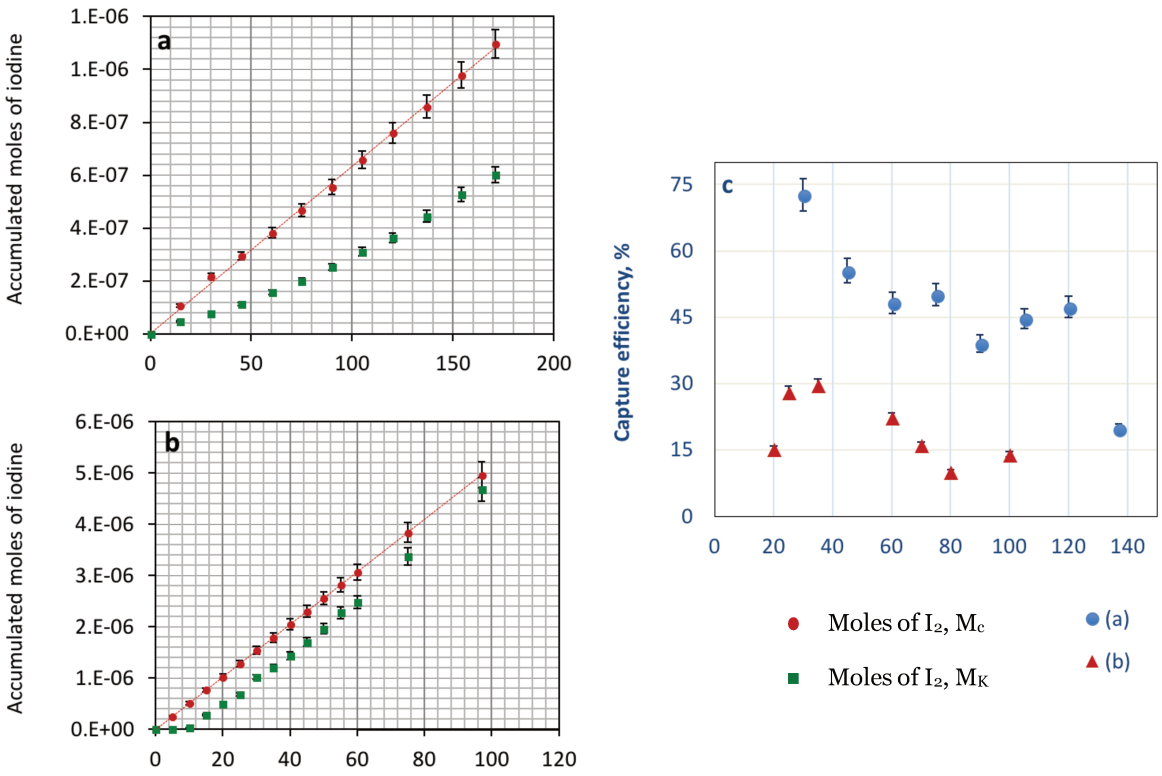

Figure 6-9 Figure (a) showing the capture efficiency by 6 g of powdered Na_2CO_3 sorbent, experiment performed at (80°C; 0.4 NL min^{-1}; 100°C) and experiment (b) performed at (115°C; 0.4 NL min^{-1}; 100°C). Figure (c) showing the capture efficiency by experiments (a) and (b).Time (minutes) is plotted on the x-axis.

6.3 Quantification of the kinetics of I_2 (g) uptake by Na_2CO_3 (s) by IBBCEAS

Five experiments were performed by using coupling an optic cell with IBBCEAS detection technique to measure the evolution of gaseous iodine in presence of sodium carbonates. As described in Section 4.8, the aim of these on-line measurements is to have more accurate results on the kinetics of the adsorption of gaseous iodine by the sodium carbonate. Capture efficiencies were calculated using Equation 4-14, and are plotted against time. The influence of the following parameters was studied (Ar flow was set at 1.0 NL min^{-1} for all the experiments):

- Reaction temperature
- Mass of Na_2CO_3 sorbent and physical nature of the sorbent (powdered sorbent and aerosol deposits)

Table 6-2 Boundary conditions of the different experiments performed with IBBCEAS facility.

Mass of sorbent, mg	T(I_2), °C	T(R), °C
20 [a]	100	100
38 [a]	100	100
46 [a]	100	150
40 [a]	70	100
7000 [p]	100	100

[a] Aerosol deposit sorbent; [p] Powdered sorbent.

To give details about the experiment conducted, in Section 6.3, (iodine generation temperature; reactor temperature; mass of sorbent in cell 1; mass of sorbent 2) is followed. So, (100°C; 100°C; 18 mg; 18 mg) would imply an experiment conducted with temperature of iodine generation and reactor temperature of 100°C and sorbent places in two glass cells (5 cm in length), 18 mg each.

6.3.1 Key parameters impacting I_2 adsorption

6.3.1.1 Reaction temperature

A set of two experiments were performed to investigate the effect of reaction temperature on capture efficiency of sodium carbonate sorbent. The experimental boundary conditions are listed below.

Compared experiments, Figure 6-10

I_2 generation temperature	**FTR temperature**	Mass of sorbent
100°C; 1.0 NL min^{-1}	100°C	38 mg
100°C; 1.0 NL min^{-1}	150°C	46 mg

The results are presented in Figure 6-10 which shows a comparison between calculated capture efficiencies. A significant difference between I_2 adsorption kinetics and evolution of its capture efficiency was observed as the temperature of the IBBCEAS cell was varied from 100 to 150°C. At comparatively higher reaction temperature the I_2 capture efficiency was found to be comparatively lower. A similar behaviour was observed in case of experiments with FTR facility. Likewise, this could be explained by the fact that, at higher temperature the thermal agitation

exceeds the weak van der Waals type of interaction between the sorbent and the substrate. During this experiment, the time to reach equilibrium is about 35 minutes compared with 150 minutes for the experiment at 100°C.

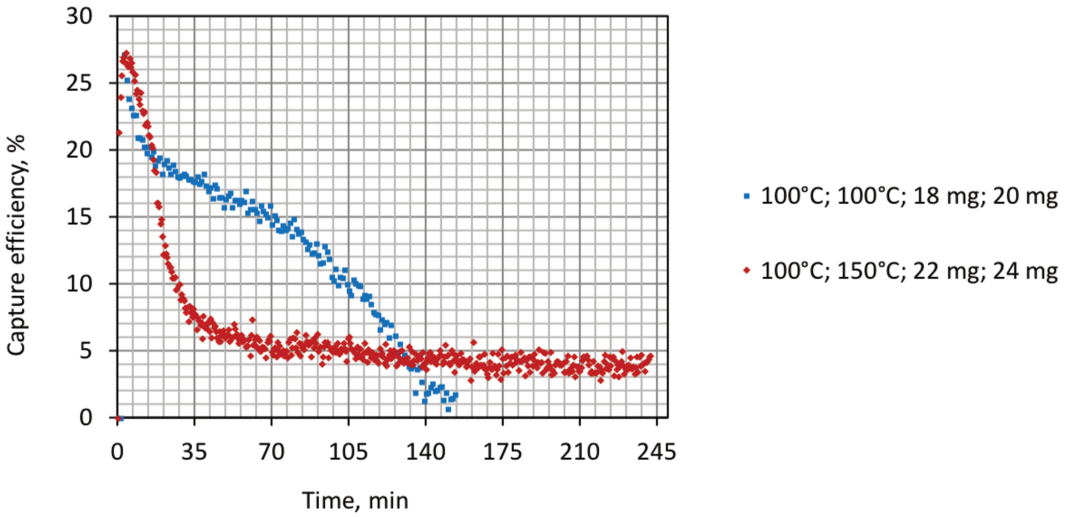

Figure 6-10 A plot showing the evolution of capture efficiency against time for two different reaction temperatures. The experiment was conducted at a reactor temperature of 100°C (dataset in blue) and 150°C (dataset in red). The mass of two experiments was comparable.

This experiment confirms thus the trend of the impact of reaction temperature on I_2 capture efficiency by Na_2CO_3 already observed in FTR in showing a decreased capture efficiency during most of the experience time at higher reaction temperature..

6.3.1.2 Mass of sorbent

Figure 6-11 shows the comparison between the capture efficiencies of two experiments performed at T(Reactor) = T(I_2 generator) = 100°C but for different mass of sorbent. The experimental boundary conditions are listed below.

Compared experiments, Figure 6-11

Experimental boundary conditions	**Mass of sorbent**
100°C; 100°C; 1.0 NL min^{-1}	20mg[a]
100°C; 100°C; 1.0 NL min^{-1}	7 g[p]

[a] Aerosol deposit sorbent; [p] Powdered sorbent

It is evident from the figure that for lower mass of sorbent (20 mg), dataset in green triangles, the capture efficiency becomes 0.15 % after 105 minutes of iodine exposure. It can safely be said that the equilibrium for this experiment was reached after about 90 minutes of the experiment.

The time for reaching the equilibrium between gas phase iodine and sorbent surface increased with the mass of sorbent.

One experiment was performed with 7 g of powdered sorbent. The calculated capture efficiency stalled to a value of about 8 % for almost two hours.

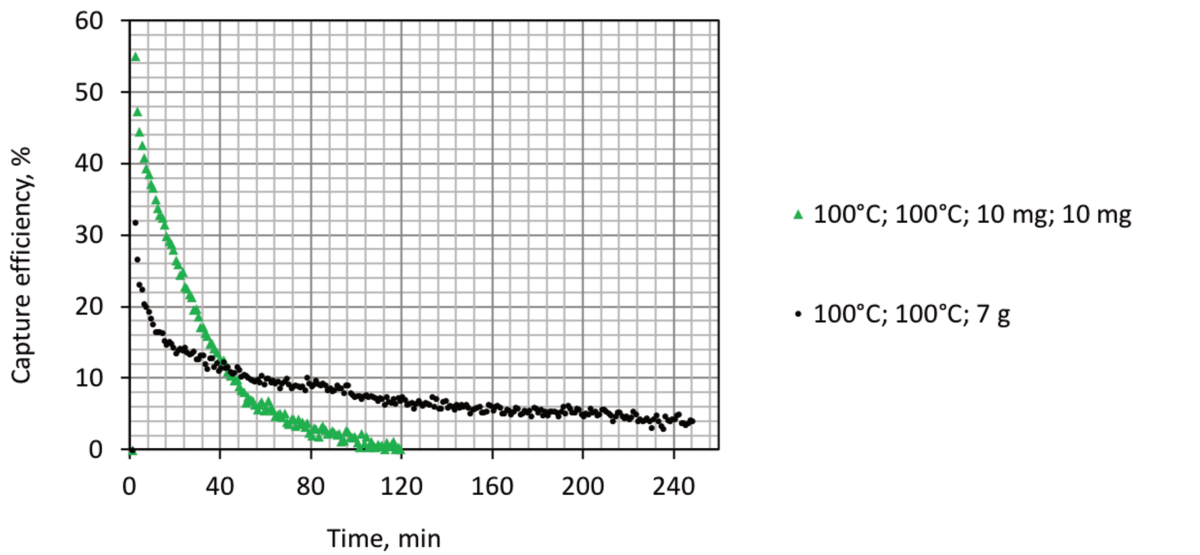

Figure 6-11 Evolution of capture efficiency against time for different mass and surface area of sorbent. All the experiments performed at T(I_2 generator) = T(Reactor) = 100°C and Q_{Ar}: 1Nl min^{-1}.

One experiment was performed for prolonged duration of time. The experiment was performed with iodine generation at 70°C and a mass of aerosol deposit sorbent of 40 mg. The result is shown in Figure 6-12. According to the figure, it appears that no equilibrium was achieved after about 12 hours. The calculated capture efficiency follows a decay curve continuously. The measured capture efficiency was found to be 23.2% after 703 minutes of the experiment.

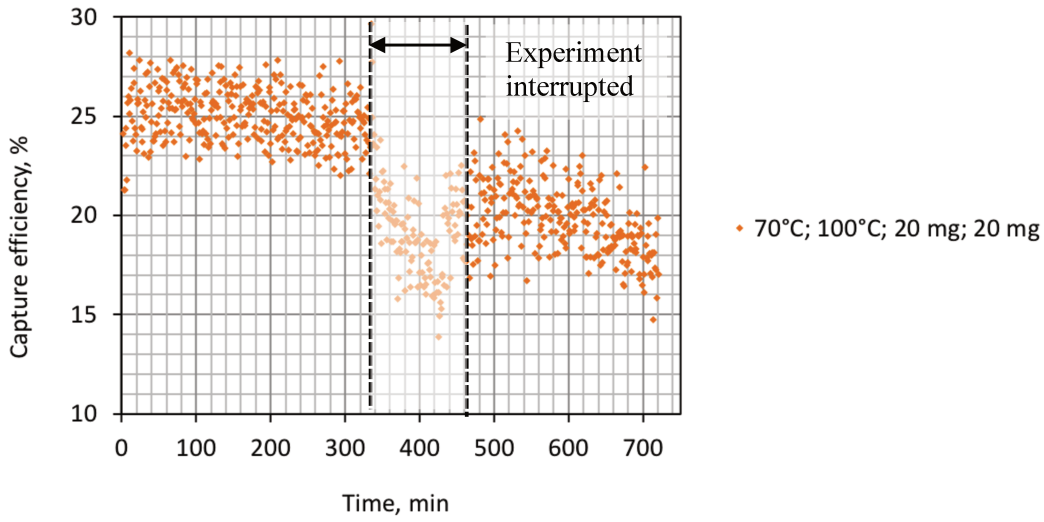

Figure 6-12 Kinetics of the reaction between Na_2CO_3 (s) aerosol deposit sorbent and I_2 (g). The sorbent was exposed in a constant flux of iodine for about twelve hours.

6.3.2 Comparison between FTR and IBBCEAS techniques

Figure 6-13 shows the comparison between both the experimental techniques using experiments with similar initial conditions (I2 partial pressure, reaction temperature and deposited sorbent masses). It can be seen from the figure that the discrete data obtained with FTR technique bare in a close agreement with the IBBCEAS results provided by on-line measurements. Unfortunately, with a limitation on time and resources combined with the complexity of the IBBCEAS experiments, only one such experiment was conducted to have insights about the similarityof the I_2 adsorption results obtained by the two detection techniques.

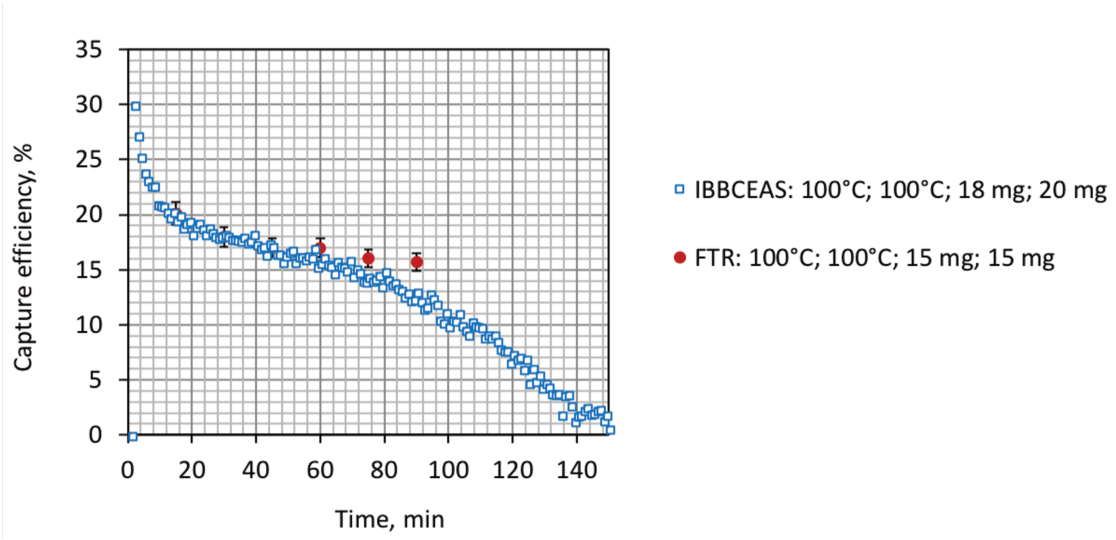

Figure 6-13 Figure showing the comparison between capture efficiency obtained by IBBCEAS and FTR technique. Both the experiments conducted at (100°C; 1.0 NL min^{-1}; 100°C) for equivalent mass of sorbent.

6.4 Preliminary kinetic modelling of the experimental results

Based on the experimental results obtained using the FTR, a simplified kinetic model has been developed to quantify the uptake of I_2 (g) on sodium carbonate sorbent. The uptake o iodine was modeled by a simplified pseudo first order kinetic presented below. A schematic diagram of the experiments can be presented as in Figure 6-1414, where :

$$q^0_{I_2}(t) = q^{uptake}_{I_2}(\mathrm{t}) + \mathrm{q}_{\mathrm{I}_2}(\mathrm{t}), \qquad 6\text{-}1$$

with $q^0_{I_2}(t) = q^0_{I_2} = constant$ is the flow rate (in mole min^{-1}) of I_2 entering the FTR and $q^{uptake}_{I_2}(\mathrm{t})$ and $q_{I_2}(t)$ are the flow rate (in mole min^{-1}) of I_2 uptake by the sorbent and of I_2 trapped by the bubbler respectively.

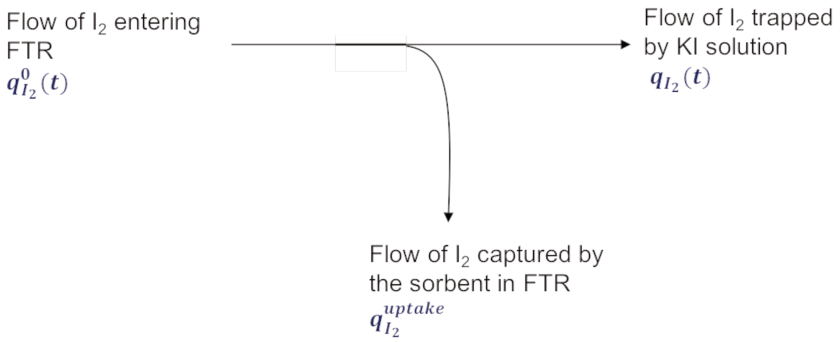

Figure 6-14 Schematic diagram showing the lifecycle of iodine in the experimental setup. A part of the flux of I_2 (g) entering the FTR interacts with the sorbent present inside it, the rest is trapped by the KI solution in the gas trap bubblers.

Experiments without carbonates (calibration runs)

Assuming a constant temperature of the oven during a few hours, a constant flow of iodine in gas phase is generated and mixed with the carrier gas and then is directed in the FTR. If no carbonates are introduced and assuming no losses of I_2 on the inner surfaces of the reactor and the lines, the iodine will be trapped in the bubbler and transformed in I_3^- ion. The accumulated quantity of I_3^- is then periodically measured after sampling the solution and measuring the absorbance of the solution by UV-vis spectrometry.

Let $N_{I_2}(t)$ be the quantity of I_2 trapped by the bubblers (analyzed by UV spectrometer).

So at a given time, the quantity of I_2 measured is:

$$N_{I_2}(t) = q^0_{I_2} . t, \qquad 6\text{-}2$$

Where $N_{I_2}(t)$ is in moles (of I_3^- or I_2) measured in the bubbler, $q^0_{I_2}$ is the initial I_2 flow rate (in moles min^{-1}) of I_2 at the exit of the oven and t is the time in min. In Equation 6-1, $q^0_{I_2}$ is assumed to be constant as the temperature of iodine permeation tubes is kept constant for the duration of the experiment (T_{oven} constant).

So the experimental measurements of data plot of $N_{I_2}(t)$ as a function of time can be fitted by a straight line where the slope is $q^0_{I_2}$. Hence, the quantity of iodine (in moles) in the reactor can be calculated from Equation 6-2, which reads:

- Calculation of concentration of iodine in the reactor

$$[I_2]_g = \frac{q^0_{I_2} \times N_A}{Q_{N_2}}, \qquad 6\text{-}3$$

where, N_A is Avogadro's constant, Q_{N_2} is the carrier gas flow rate.

Experiments with carbonates (kinetics runs)

When carbonates are introduced in the reactor, part of the flow or the whole may be trapped by the sorbent and the rest will be trapped in the bubbler (see Figure 6-15). Let's consider that the $q_{I_2}^{uptake}$ be the flow rate of moles of iodine trapped (adsorption minus desorption) by the sorbent. Then, assuming a pseudo-first order kinetic law:

$$q_{I_2}^{uptake}(t) = q_{I_2}^{max} e^{-k^I t}, \tag{6-4}$$

where k^I is the pseudo-first order rate constant. Both adsorption and desorption are included in this definition of k^I.

At t = 0, $q_{I2}^{uptake} \rightarrow q_{I_2}^{max}$ implying that the number of active sites is maximum
While, at $t >> t^{eq}$, $q_{I2}^{uptake} \rightarrow 0$ signifying the saturation of active sites. t^{eq} is the time at which equilibrium between species in gas phase and the surface is reached.

So, at the exit of the reactor (see Figure 6-14)

$$q_{I_2}(t) = q_{I_2}^0 - q_{I_2}^{uptake}(t) \tag{6-5}$$

In the bubbler, the total I_2 trapped by I^- is given by:

$$N_{I_2}(t) = \int_0^t q_{I_2}^0 - q_{I_2}^{uptake}(t).dt \tag{6-6}$$

$$N_{I_2}(t) = \int_0^t q_{I_2}^0.dt - \int_0^t q_{I_2}^{max} . e^{-k^I.t} . dt \tag{6-7}$$

$$N_{I_2}(t) = q_{I_2}^0.t + \frac{q_{I_2}^{max}}{k^I} . e^{-k^I.t} + constant \tag{6-8}$$

At t = 0, $N_{I_2}(t) = 0$, applying boundary condition in the equation above

$$0 = \frac{q_{I_2}^{max}}{k^I} + constant \tag{6-9}$$

$$N_{I_2}(t) = q_{I_2}^0 . t - \frac{q_{I_2}^{max}}{k^I} . (1 - e^{-k^I . t})$$

At t >> t^{eq},

$$N_{I_2}(t) = q_{I_2}^0 . t - \frac{q_{I_2}^{max}}{k^I} \quad 6\text{-}10$$

In the reactor, $q_{I_2}^{max} = q_{I_2}^0$,so

$$N_{I_2}(t) = q_{I_2}^0 . t - \frac{q_{I_2}^0}{k^I} . (1 - e^{-k^I . t}), \quad 6\text{-}11$$

where, $N_{I_2}(t)$are the total moles of I_2 trapped by the bubbler at time t.

At t>>t^{eq}, the total I_2 adsorbed by the carbonate sorbent, when equilibrium is reached, can be written as

$$N_{I_2}^{uptake} = \frac{q_{I_2}^0}{k^I} \quad 6\text{-}12$$

The main goal of the model is to calculate total uptake of iodine at equilibrium. Equation 6-12, gives a relationship between total iodine uptake, incoming iodine flux, and the pseudo-first-order rate constant. The only parameter fitted (based on experimental data) in the model is the rate constant. The applicability of the presented kinetic model is presented the next, on experiments involving sodium carbonate sorbents and iodine is presented the next, in Figure 6-155 and associated pseudo-first-order kinetic constant and total iodine uptake by the sorbent are listed in Table 6-3.

Extended interpretation from the model, namely, molecular density of the adsorbed iodine is also listed in the table. Calculation of the molecular density of the adsorbed iodine is based on the input from BET surface area measurement (~0.6 m^2g^{-1}). The total uptake of iodine is calculated from the model. Furthermore, the ratio of molar uptake of iodine and BET surface area gives the molecular density of the adsorbed iodine. It is worth mentioning here that the uncertainty in the BET measured surface area is huge (perhaps, as high as 100%). However, with limited information and difficulty in measuring the surface area of the sorbent, the calculation of molecular density of the adsorbed iodine might give some useful insight. The

molecular density of the adsorbed iodine, approximated, by the experiments can be compared with the DFT predications.
The experimentally approximated value of adsorbed iodine density is 2-3 molecules per nm^2 of sorbent area. Despite the possibility of very high uncertainties in the experimentally approximated value, there is a good agreement between the two approaches (under certain assumptions). A comparison between both the approaches is shown in Section 7.2.
The model gives a rough insight on the order and magnitude of the kinetic constant of the reactions involving I_2 and powdered sorbent placed in Teflon cells (Experiment a $\rightarrow$ d) and in a rupture cell (Experiment e). The model seems to fit the experimental data well. However, the presented model is very simple in nature and does not include all the complexities usually involved in the heterogeneous reactions such as surface area, pore size & distribution of the sorbent; it leaves a lot of room for further developments. Nevertheless, the presented, pseudo-first order kinetic model, can be considered as the first step in modeling the kinetic process of iodine adsorption.

Limitations of the pseudo-first-order kinetic model

As mentioned earlier, the proposed model is very preliminary in nature and can be considered as *groundwork* in the modeling process. It is important to clearly state the shortcomings of the proposed model:

- It does not distinguishes between adsorption and desorption constants. As a result of which we have very little about k^I and its constituents.

- The proposed model does not give any indication about the kind of adsorption and isotherm function (i.e., monolayer or multi-layer adsorption).

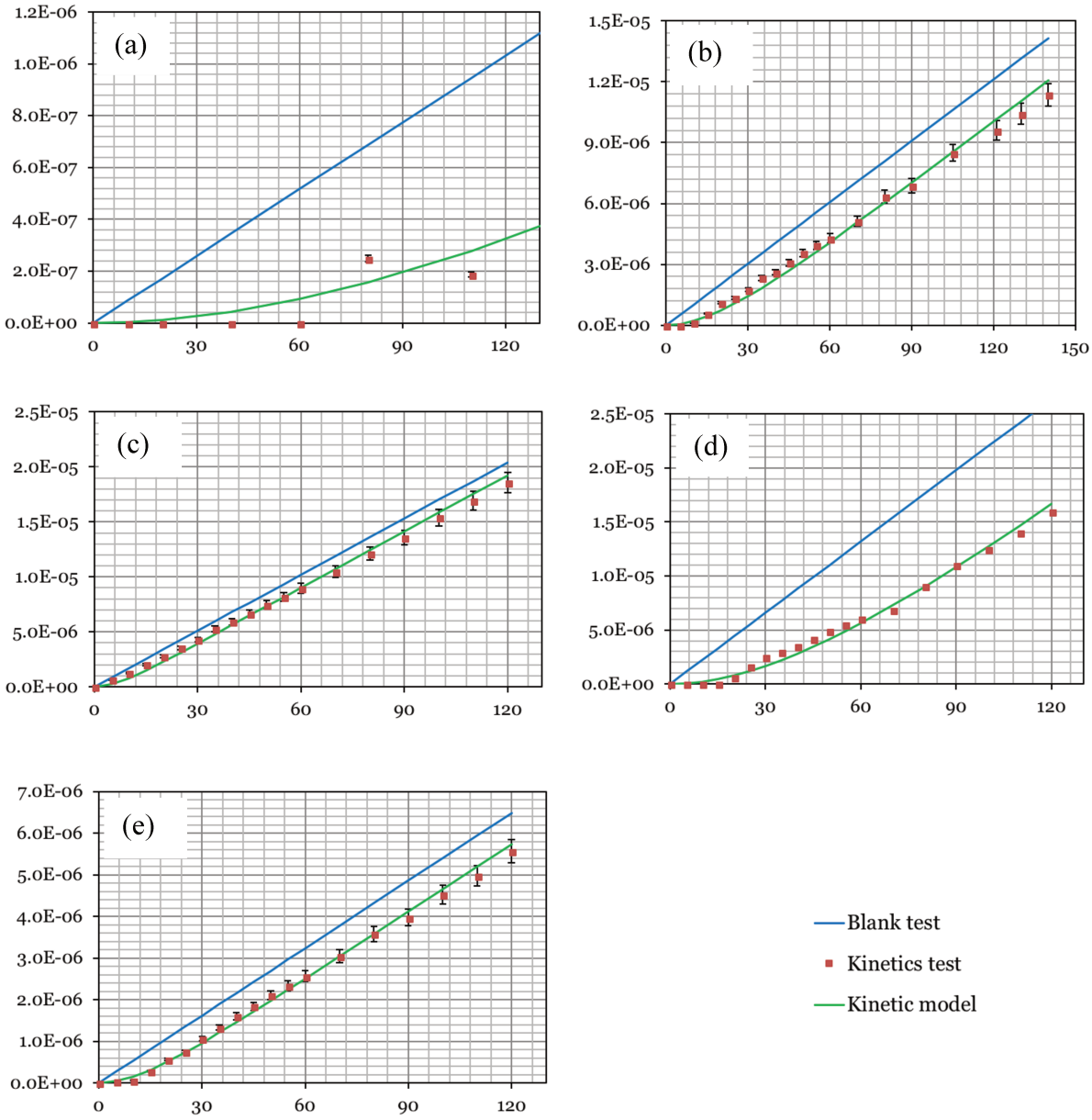

Figure 6-15 Figure showing the applicability of the pseudo-first-order kinetic model on the experimental results. X-axis: time in minutes; Y-axis: moles of iodine accumulated in the bubbler.

Conclusions and perspectives

Table 6-3 A table showing the calculated pseudo-first-order kinetic constant for different experiments and associated boundary conditions. All the experiments conducted at T(R) = 100°C, Q_{Ar} = 0.4 NL min^{-1}. Experiments(a→d) are conducted with powdered Na_2CO_3 sorbent placed in Teflon cell while Experiment (e) with sorbent placed inside a rupture cell.

Experiment	T(I_2)	Mass sorbent	k^I	I_2 uptake	I_2 molecule nm^{-2}(high uncertainty)
	°C	g	s^{-1}	mole	
a	80	6.0	1.1×10^{-4}	1.3×10^{-6}	2
b	115	6.0	8.1×10^{-4}	2.1×10^{-6}	3
c	130	6.0	2.4×10^{-3}	1.2×10^{-6}	2
d	130	3.5	3.8×10^{-3}	7.3×10^{-7}	2
e	115	3.5	1.2×10^{-3}	7.4×10^{-7}	2

Perspectives for experimental studies

Due to time constraint the experimental studies could not be properly finalized. Several additional tests would have been necessary both to confirm the obtained results and to explore others boundary conditions. More especially, as the experimental investigations conducted in the laboratory were not exactly representative of the SA conditions, experimental investigation of the following cases shall be addressed:

- Interactions between molecular iodine and aerosols in suspension.
- Investigation of effect of humidity on iodine adsorption.
- Better surface characterisation of the Na_2CO_3 sorbent.
- Coupling the FTR with more sensitive, iodine detection technique, such as ICP-MS.
- Conducting the experiments (specially the preparation of sorbent surfaces) in a controlled environment in order to avoid any chemical interferences.

Chapter 7 Conclusions and perspectives

From the nuclear safety point of view, the potential uptake of gaseous I_2 by sodium combustion products by lowering its residual equilibrium partial pressure would contribute to mitigate the consequences of a severe accident occurring in a SFR. That is why a thorough analysis of the interaction between gaseous iodine and sodium carbonates, combining both a theoretical and experimental approach, was performed.

7.1 Summary of the main results

The main objectives of the project were addressed. These include the specific questions:

- Does gaseous I_2 significantly and perennially interact with Na_2CO_3 (s)?
-
- What is the quantitative gaseous I_2 uptake on Na_2CO_3 (s) sorbent surfaces and the associated equilibrium iodine partial pressure in the gaseous phase?
-
- What is the kinetics of the interaction between gaseous iodine and Na_2CO_3 (s) sorbent surface?
-
- What are the main factors impacting the gaseous I_2 capture by Na_2CO_3 (s) and the kinetics of the reaction?

All these questions were answered and summarised in this chapter using both theoretical chemistry and experimental approaches. Finally, possible directions for future work are also proposed.

7.1.1 Theoretical approach

Structural properties of γ-Na_2CO_3 from first principles

A part of this thesis presented theoretical chemistry investigation into the determination of structural properties of γ-Na_2CO_3 such as the crystal lattice parameters, surface morphologies and defects, and so forth. The DFT-D3 calculated crystal lattice parameters were found to be in good agreement with the XRD produced experimental results found in the literature. The relative stability of different γ-Na_2CO_3 surfaces has been investigated using the DFT-D3 method. The two most stable surfaces have been found to be γ-Na_2CO_3 (001) and (110) respectively. None of the studied surface defects were found to be stable compared to the ideally cleaved surfaces. That is why only the reactivity of the ideally cleaved (001) and (110) surfaces was studied. However, a local minimum of surface (001), referred as Na_2CO_3(001)-a have been identified and showed a stronger affinity for iodine than the 'global minimum' of this surface, Na_2CO_3(001)-b.

Reactivity of γ-Na_2CO_3 surfaces vis-à-vis I_2, HI, and H_2O

The reactivity of I_2 (g), HI (g), and H_2O (g) on γ-Na_2CO_3 surface (001) was studied. It was found that the associative adsorption of I_2 (g), HI (g), and H_2O (g) is thermodynamically favored (exothermic) while the dissociative one is endothermic, at 0 K. γ-Na_2CO_3 surface (001) reacts more strongly with HI (g), and H_2O (g) compared to I_2 (g). The reactivity of hydrated γ-Na_2CO_3 surface (001) with I_2 (g) was also studied and found to be less favourable.

Finally, the surface reactivity of γ-Na_2CO_3 surface (110) against I_2 (g) was found to be higher compared to (001) near the saturation partial pressure of iodine at 100°C while the γ-Na_2CO_3 surface (001)is more reactive at lower iodine partial pressure.

Development of ab-initio based analytical model

An ab-initio based analytical model has been developed to calculate the adsorption isotherm able to predict the uptake of iodine based FP (such as I_2 (g) and HI) on the γ-Na_2CO_3 surfaces as well as bicarbonate formation at a finite temperature. The calculated uptake efficiencies were reported to be one molecule per 47Å^2 for (001) and one molecule per 32Å^2 for (110) at 373 K.

Based on the assumption that the Na_2CO_3/I_2 ratio is reasonably high in case of core disruptive accident occurring in a SFR, according to DFT calculation results, the equilibrium residual partial pressure of I_2 (g) can be expected to be strongly lower than 2×10^{-4} bar at 373.15 K.

7.1.2 Experimental approach

A flow tube reactor was especially designed to study the uptake of molecular iodine by sodium carbonates and the associated kinetics, where the capture efficiencies for different boundary conditions were deduced from UV spectrometry measurements of periodic samples. In addition, few more accurate on-line optical measurements of I_2 (g) density evolution in presence of carbonates, using an IBBCEAS technique were also performed. Experiments were performed either on Na_2CO_3 commercial powder or on deposited aerosols.

The interaction between I_2(g) and Na_2CO_3(s) was suggested by ToF-SIMS surface measurements. Though the nature of the interaction could not be characterized, none of the desorption tests that have been performed led to measurable amount of gaseous I_2.

The evolution of the I_2 (g) capture efficiency by sodium carbonates as a function of partial pressure of iodine, mass (and surface area) of sorbent, and the reaction temperature was characterized.

I_2 (g) capture efficiencies

The I_2 (g) capture efficiencies were found to increase with the iodine partial pressure and the accessibility of adsorption sites (i.e. the sorbent surface area). Meanwhile, the increase in temperature from 100 to 150°C led to a lower capture efficiency. The simplified kinetics model developed to analyse the experimental data allowed to estimate the equilibrium adsorbed iodine amount and the molecular iodine density. This latter was found to be in a reasonable agreement (within certain assumptions) with the DFT calculation results.

I_2 (g) capture kinetics

From the experimental data, a simplified pseudo-first order kinetics model was developed, where the only fitted parameter was the overall kinetics constant covering both adsorption and desorption phenomena. Despite many limitations and shortcomings, the model gave a rough insight of the order of magnitude of the pseudo kinetics constants (10^{-3}-10^{-4} s^{-1} depending on the boundary conditions). This simplified model represents a first step in modelling the FP vapour interaction with sodium combustion aerosols but much more modelling effort will still have to be done in order to derive more accurate kinetics constants.

7.2 Confrontation of theoretical and experimental methodologies

The comparison between the two approaches was challenging mainly due to great uncertainties in sodium carbonate surface determination and, to a less extent, to the difficulties in handling so low concentration of gaseous iodine. In addition, it was theoretically challenging to find a balance between computational resources and the limited timeframe of the project.
In the theoretical approach ideal surfaces were considered while in experiments, though it was made sure that the sorbent was of highest quality, in absence of a controlled environment, organic impurities and water might have partly covered the sorbent surface affecting then its reactivity towards $(I_2)_g$. In reality, the sorbent surface consists of several micro-surfaces. These micro-surfaces differ from one another by surface morphologies and structures. Theoretically speaking, it is quite impossible and expensive (both resources and time-wise) to model the realistic surface as it depends on a lot of factors such as temperature, presence of other gaseous phase species and so forth.

Despite all this, a reasonable agreement was found where, both experimental data and theoretical calculations put forward an effective capture of $(I_2)_g$ by the carbonates within SA boundary conditions.
There is a disagreement between the two approaches when iodine reactivity with the most stable, Na_2CO_3(001)-b, is considered. However, the formation of Na_2CO_3(001)-b requires a severe reconstruction of the surface Na_2CO_3(001)-a. This transition is highly likely to be associated with a kinetic limitation. Keeping in mind this fact, one cannot exclude the co-existence of Na_2CO_3(001)-a and Na_2CO_3(001)-b, where the former surface shows one hundred times higher affinity towards iodine. Such an affinity is in a very good agreement with the experimental measurements. The figure below shows a comparison between DFT obtained and experimental measurements of iodine reactivity for Na_2CO_3(001)-a.

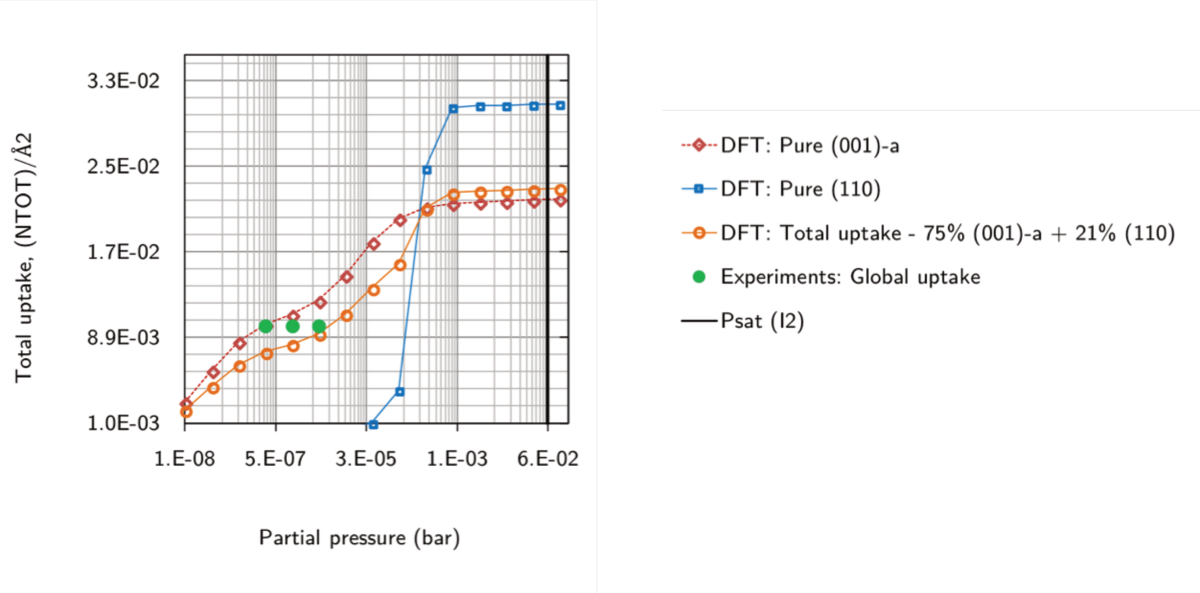

Figure 7-1 Comparison between DFT obtained reactivity of Na_2CO_3 (001)-a and I_2 (g) and experimental measurements.

7.3 Main conclusions

Thanks to the DFT calculations and experiments, one gains insights on thermodynamic and kinetics data on reaction of I_2(g) and Na_2CO_3 (s) surfaces.
According to the studies performed, the iodine partial pressure inside the reactor containment will be below 2×10^{-4} bar, at 373.15 K for high Na/I molar ratios. Though rather low, the remaining I_2(g) partial pressure can't be neglected concerning the radiological risk associated with volatile iodine.
The presented ab initio model developed for I_2(g) isotherm adsorption on sodium carbonates can be extended to study the adsorption of other gaseous phase FP based species (for example, ruthenium) on sodium combustion surfaces.

7.4 Perspectives

The theoretical methodology developed will be used to produce thermodynamical data that could be further implemented in the SA simulation code developed by the IRSN for studying the SA and quantifying the source term in SFRs (ASTEC-Na).

Meanwhile, as the simplified kinetics modelling of I_2(g) uptake by sodium carbonates was only based on a limited range of experimental conditions, much modelling effort will have to be done. Indeed, for a reliable extrapolation, the model will probably have to be deconvoluted into basic physicochemical parameters describing the multiple steps that are usually taking place in aerosol surface reactions and gas particle interactions.

Conclusions and perspectives

Finally if the work performed in this thesis fills some of the gaps of knowledge and allows answering some of the originally imposed questions and thus allowing to foreseen the next questions to answer to before evaluating SFR iodine source terms:

- What is the influence of the radiations on the surface and hence its reactivity for iodine?

- What is the impact of multiple layers of water on reactivity?

- How the interactions of iodine with other surfaces such as containment walls and organic materials (i.e., cables…) impact its interactions with sodium aerosols?

Summary

In addition to the large per capita energy consumption in developed nations, there is an increase in global demand of electricity. Keeping in mind the commitments made in the Paris agreement, it is then important to meet the world's energy demand with the current resources in a sustainable way. The present day nuclear reactors are predominantly thermal rectors which have poor efficiency regarding the use of low enriched uranium fuel. These reactors do not harness the energy from the fertile material U-238, and only U-235 is used as fuel. To address limitations posed by thermal reactors, Generation IV forum selected a few, next-generation technological designs to be developed for commercial use. The safety requirements for Generation IV nuclear reactor designs, especially for the new generation sodium-cooled fast reactors (SFR), require a risk-informed approach to model severe accidents (SA) and their chemical and radiological consequences in case of outside release of sodium aerosols and fission-products (FP). In SFRs, different chemical forms of sodium aerosols can be produced during a core disruptive accident when FP contaminated primary sodium is ejected into the containment and burn in contact with air, consisting of sodium peroxides, hydroxides, carbonates, and bicarbonates. In addition to being chemically toxic (in oxide/hydroxide forms), these aerosols are also radioactive both because of the sodium neutron activation in the reactor primary system and the FP species that have been dissolved in it during the fuel pin degradation and rupture. If such aerosols would leak into the environment, they may thus pose potential hazard to the surrounding ecosystem and population. On the other hand, some of the FPs initially transported by the primary sodium can, once the sodium burns, be released in the containment atmosphere. Amongst these FPs, iodine is of primary concern in radiological risk determination because of its numerous chemically active radioisotopes (i.e., I-131), its highly volatile species (i.e., I_2, HI) and its great affinity for human thyroid. Thus, the chemical and radiological consequences of a SA in a SFR, leading to a containment leak tightness loss, will depend on the sodium aerosol speciation and contamination on one hand but also on the specific becoming of volatile FPs that might be volatilized from the primary contaminated sodium combustion on the other hand. One of the key aspects in SFR

safety evaluation is then a correct prediction throughout the SA of the in-containment sodium aerosol and FP behavior.
The objective of this work is to study the interactions between sodium aerosols and FP species vapors and more especially between sodium carbonates and molecular iodine.
A multiscale approach was followed in this work. On an atomistic scale, a method to theoretically understand thermodynamics of the reaction between Na_2CO_3 and I_2 was used. Ab-initio, density functional theory (DFT) calculations using Vienna ab-initio simulation package were carried out to develop an understanding of the surfaces of Na_2CO_3 aerosols and hence provide insights on its affinity towards the iodine species of interest. A comprehensive study of I_2 and HI adsorption, as well as bicarbonate formation on the calculated lowest energy surface of Na_2CO_3, was performed which provided adsorption energies and description of the optimized configuration of adsorbates on the most stable surfaces. These calculated data have been used to predict the isotherms of adsorption of different gaseous species vis-à-vis the most stable surfaces, using a new analytical expression of adsorption isotherm developed in this work.
On a macroscopic scale, both surface characterization by BET and ToF-SIMS measurements and experimental investigation of the heterogeneous reaction between I_2 (g) and Na_2CO_3 (s) were performed. Two distinct and complementary measurement methods were used to study the kinetics of the reaction and determine the adsorption capacity of the sodium carbonates. For a better understanding of the reaction, the impact of molecular iodine concentration, carbonate surface and temperature were experimentally studied. Finally, in a first approach, a simplified pseudo-first order reaction model was built to analyze the experimental results. It only provides a rough insight on the order and magnitude of pseudo-first order kinetic constants and maximum I_2 uptakes for different boundary conditions. The average I_2 uptake efficiency thus calculated from the experiments, 2-3 molecules per nm^{-2}, was found to be in a good agreement with the uptake efficiencies predicted by ab-Initio DFT calculations, at least for one of the considered surfaces.

The experimental and theoretical results obtained in this study, though preliminary, have improved our understanding of the interaction between iodine vapors and sodium carbonates. The main outcomes of this Ph.D. research are multifold:

1) A generic, multi-scale methodology to study the interactions between sodium combustion products and FP vapor has been developed. It will be possible to use this methodology in the future to study aerosols and volatile FP vapors other than the one presented in this manuscript;

2) Both thermodynamic and kinetic data on interactions between sodium carbonate aerosols and gaseous iodine have been provided, thanks to the performance of ab-initio calculations and experiments;
3) An analytical ab-initio model for adsorption isotherm has been developed and allows predicting, at equilibrium adsorption, the surface coverage as a function the vapor partial pressure at finite temperature;
4) The ab-initio calculation results providing the I_2 uptake efficiency have been consolidated by experimental measurements validating the analytical methodology for exploring other interactions;
5) At the average gas temperatures expected in the containment in case of a SFR severe accident with primary sodium ejection outside the primary circuit, (i.e. between 373 and 423K), the most favorable carbonate surfaces were found to be predominantly bare or doubly occupied depending on the iodine partial pressure;
6) The surface adsorption of I_2 on sodium carbonates was found to be associative which is in favor of physisorption rather than chemisorption phenomena. However, surface characterization by ToF-SIMS after interaction indicates that the interaction between iodine and sodium is not so weak;
7) The adsorption of H_2O (g) on sodium carbonates was found to be not thermodynamically favored compared to I_2 which means that I_2 uptake efficiency will not be altered by high steam ratio in the containment atmosphere.
8) The kinetics of the I_2 uptake by sodium carbonates was not evidenced to be thermally activated and to be dependent both on I_2 concentration and the accessibility of the adsorption sites of sodium carbonates

All these findings being taken into account and considering firstly the low concentration of iodine expected in the containment with respect to the mass of carbonate aerosols potentially formed during the sodium combustion in case of a core disruptive accident and secondly the potential high surface area developed by sodium combustion aerosols would lead to an optimized and efficient uptake of I_2 in lower temperature areas not altered by steam.

Appendix

A.1. FTR experiments

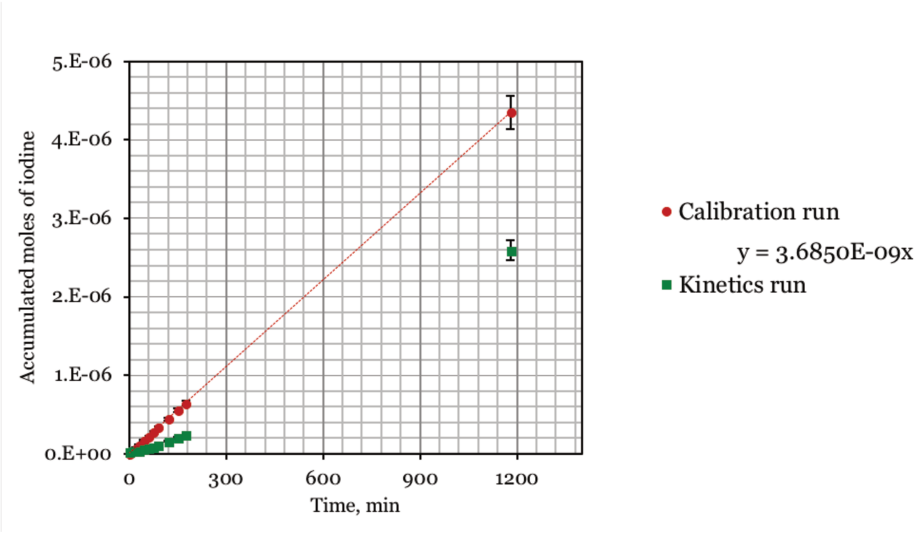

Figure A. 1 Comparison between calibration and kinetics run. Experiment conducted at (70°C; 0.4 NL min^{-1};100°C) and 5 g of powdered Na_2CO_3 sorbent.

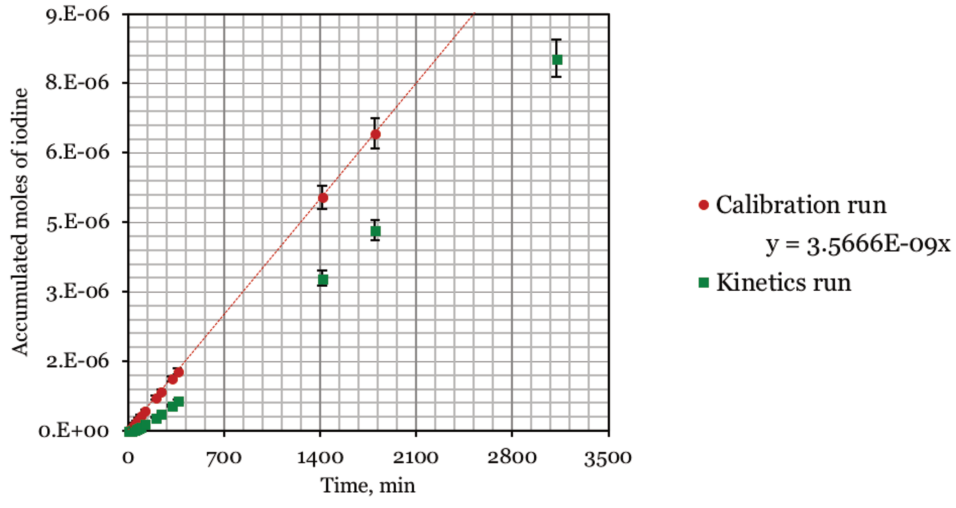

Figure A. 2 Comparison between calibration and kinetics run. Experiment conducted at (70°C; 0.4 NL min^{-1};100°C) and 3 g of powdered Na_2CO_3 sorbent.

A.2 Grid of the experiments conducted – FTR

Table A. 1 A table showing all the experiments conducted in the laboratory with the FTR coupled with the UV-spectrometer. The boundary conditions changed to study their effect on the kinetics of the reaction between Na_2CO_3 (s) and I_2 (g) are mentioned.

Iodine generation temp, °C	Q Ar (NL/min)	Reactor temp, °C	Mass of sorbent, g
70	0.4	100	3.00
70	1.0	100	3.00
70	0.4	100	5.00
70	0.4	100	0.80
70	0.4	150	0.92
70	0.4	100	0.93
70	0.4	100	0.91
70	0.4	100	0.91
70	0.4	100	0.55
70	0.4	100	0.87
70	0.4	100	6.84
70	0.4	100	2.10
70	0.4	100	7.38
70	0.4	100	0.81
70	0.4	100	0.07
70	0.4	100	0.11
70	0.4	60	0.08
70	0.4	150	0.61
70	0.4	150	0.05
70	0.4	100	0.04
70	0.4	100	0.03
70	1.0	100	0.02
70	1.0	100	0.03
70	0.4	60	0.06
70	0.4	150	0.05
80	0.4	100	0.09

80	0.4	100	0.09
80	0.4	100	0.12
100	1.0	100	0.04
100	1.0	100	0.04
100	1.0	100	0.06
100	1.0	100	0.10
100	1.0	100	8.00
100	0.4	100	0.65
100	0.4	100	3.50
100	0.4	100	3.50
100	0.4	100	6.00
100	0.4	100	3.50
100	0.4	100	3.50
115	0.4	100	3.50
115	0.4	100	3.50
115	0.4	100	6.00
130	0.4	100	3.50
130	0.4	100	3.50
130	0.4	100	6.00

A.3 Grid of the experiments conducted – IBBCEAS

Table A. 2 A table showing all the experiments conducted in the laboratory with the optical cell coupled with the IBBCEAS detection technique. The boundary conditions changed to study their effect on the kinetics of the reaction between Na_2CO_3 (s) and I_2 (g) are mentioned.

Mass of sorbent, mg	T(I_2), °C	T(R), °C
20.5 [a]	100	100
38 [a]	100	100
46.5 [a]	100	150
40.0 [a]	70	100
7000 [p]	100	100

References

[1] Western European Nuclear Regulator's association, "WENRA Statement on safety objectives for new nuclear power plants" November 2010.

[2] Y. Amano, "The Fukushima Daiichi Accident Report by the Director General", IAEA report, ISBN 978-92-0-107015-9, 2015.

[3] J. Chirac, Loi de programmation énergétique n°2006-739 relative à la gestion durable des matières fissiles et aux déchets radioactifs, 28 June 2006,Paris.

[4] L. Volpe, G. Rodriguez, and D. Protas, "ASTRID - An original and efficient project organization", CEA internal report, January, pp. 1–11, 2016.

[5] "The fourth generation sodium-cooled fast reactors - The ASTRID technological demonstrator", CEA internal report, Nuclear Energy Division, December, 2012.

[6] A. Plantamp, "Etude et modélisation du comportement chimique des aérosols issus d'un feu de sodium lors de leur dispersion atmosphérique", University of Lorraine, 2016.

[7] E. Mathe, "Comportement des Radiocontaminants dans les confinement d'un réacteur a neutron rapides refroidi au sodium en situation accidentelle", University of Lille 1, 2014.

[8] D. A. Powers, B. Clément, R. Denning, S. Ohno, and R. Zeyen, "Advanced Sodium Fast Reactor Accident Source Terms: Research Needs", SANDIA National Laboratory internal report SAND2010-5506, 2010.

[9] "Liquid Metal Cooled Reactors: Experience in Design and Operation", 2007.

[10] M. Garcia, L.E. Herranz and M. Kissance, "Release & transfer of dangerous products", Internal Deliverableof the Euratom FP7 CP-ESFR Project fu" 2012.

[11] F. Gelbard, "MAEROS User Manual", 1982.

[12] K. K. Murata, D. E. Caroll, D. Bergeron and G. Valdez, "CONTAIN LMR/1B-Mod.1, A computer code for containment analysis of accidents in liquid-metal-cooled nuclear reactors", *Report from SANDIA National Laboratories, SAND91-149*.

[13] A. Kumar, V. Subramanian, and R. Baskaran and B. Venkatraman "Size Evolution of Sodium Combustion Aerosol with Various RH %", Aerosol and Air Quality Research, vol. 15, Issue 6, pp. 2270–2276, 2015.

[14] R. Baskaran, V. Subramanian, B. Venkatraman, and P. Chellapandi, "Sodium Aerosol Studies for Fast Reactor Safety", *Energy Procedia*, vol. 7, pp. 660–665, 2011.

[15] K. Mikitiuyk, E. Girardi, J. Krepel, E. Bubelis, E. Fridman, A. Rineiski, N. Girault and al. "ESFR-SMART: new horizon-2020 project on SFR safety", Proc. FR17 Conference on Fast Reactors, IAEA-CN-245-450, Yekaterinburg, Russia, June 2017.

[16] J. Minges, H. Sauter and W. Schütz, “Retention factors for fission products from sodium tests to simulate a severe LMFBR accident”, *Nucl. Eng. Des. 137, Issue 1, pp. 133-138*, 1992.

[17] H. Sauter and W. Schütz, “Aerosol release from a hot sodium pool and behavior in sodium vapour atmosphere”, *Proc. CSNI Spec. Meet. Nucl. Aerosols React. Safety. NUREG/CR-1724, ORNL/NUREG/TM-404, CSNI-45*, 1980.

[18] M. Denman, L. Walters, J. Lambert, K. Natesan, K. Wright,and A. Yacout, “Sodium-fast reactor fuels and materials: research needs” Sandia National Laboratories, SAND2012-5162, 2012.

[19] A. W. Castleman and I. N. T. Tang, “Fission product vaporization from sodium systems”, in *Proceedings on the International Conference on Sodium Technology and Large Fast Reactor Design, Argonne, Illinous*, 1968.

[20] L. S. Lebel and N. Girault, “Radionuclides emission from sodium pool fires: Learning from the 1970s-era FANAL experiments”, Nucl. Eng. Des. 327, pp. 127-138, 2018.

[21] K. Haga, Y. Nishizawa, T. Watanabe, S. Miyahara, and Y. Himeno, “Equilibrium and non equilibrium partition coefficients of volatile fission products between liquid sodium and the gas phase,” *Nucl. Technol. vol 97, 177-185, 1992.*

[22] A. Dayan and S. Zalmanovich, “Decontamination factors and releases rates of UO_2 particles from boiling pools of sodium”, *Nucl. Eng. Des. 74, pp. 127-132*, 1982.

[23] G. Fiorini, “The colloborative project on European Sodium fast reactor (CP ESFR),” FP7 EUratom Project, 2009-2014.

[24] J.-P. Van Dorsselaere, N. Girault, " The European collaborative project JASMIN (Joint Advanced Severe accidents Modelling and Integration for Na-cooled fast neutron reactors)", FP7 Euratom Project, 2011-2016.

[25] J. Papin and N. Girault, “Results of the PIRT process relative to core evolution and in-vessel structures behaviour in Design Basis transients and to core phenomenology”, Internal Deliverable of the Euratom FP7 CP-ESFR Project, 2011.

[26] Y.E. Bagdasarov and al., “Evaluation of Radioactive Materials Release and Sodium Fires in Fast Reactors”, Technical Report IWGFR-92, Oorai, Japan, 1996.

[27] J. LaChance and al., "Sodium Fast Reactor Safety and Licensing Research Plan – Volume II”, Sandia National Laboratories SAND2012-4259, 2012.

[28] S. C. Chetal, V. Balasubramaniyan, P. Chellapandi, P. Mohanakrishnan, P. Puthiyavinayagam, C. P. Pillai, S. Raghupathy, T. K. Shanmugham, and C. S. Pillai, “The design of the Prototype Fast Breeder Reactor”, Nucl. Eng. Des. 236,

References

pp. 852–860, 2006.

[29] P. Chellapandi, P. Puthiyavinayagam, V. Balasubramaniyan, S. Ragupathy, V. Rajanbabu, S. C. Chetal, and B. Raj, "Design concepts for reactor assembly components of 500 MWe future SFRs" *Nucl. Eng. Des.* 240, pp. 2948–2956, 2010.

[30] N. Girault and al., "The European JASMIN Project for the Development of a New Safety Simulation Code, ASTEC-Na, for the Na-cooled Fast Neutron Reactors", Proc. ICAPP13, Jeju ISland, Korea, April 2013.

[31] R. N. Newman, "The ignition and burning behaviour of sodium metal in air", Progress in Nuclear Energy 12, pp. 119-147, 1983.

[32] S. Ramsdale, "The chemical conversion and dispersion of toxic sodium fire aerosols in the atmosphere", *J. Aerosol Sci.* 20, pp. 1401–1404, 1989.

[33] R.A. Narayanan, V. Subramanian, P. Sahoo, J. Misra, A. Kumar, R. Baskaran and B. Saha, "Experimental investigations on carbonation of sodium aerosol generated from sodium fire in the context of fast reactor safety", Annals of Nuclear Energy, 80, pp. 188-194, 2015.

[34] V. Subramanian, P. Sahoo, N. Malathi, R. Ananthanarayanan, R. Baskaran and B. Saha, "Studies on chemical speciation of sodium aerosols produced in sodium fire", *Nucl. Technol. 165, pp. 257–269*, 2009.

[35] W. S. Clough and J. A. Garland, "The behaviour in the atmospheree of the aerosol from a sodium fire", J. Nuclear Energy 25, pp. 425-435, 1971.

[36] W. D. Cooper, "Prediction of the rates of chemical trasnformation of sodium fire aerosols", Proc. *CSNI Specialist Meeting on Nuclear Aerosols in Reactor Safety*, Gatlinburg, Tenessee, USA, pp. 181-195, 1980.

[37] A. Plantamp, T. Gilardi, C. Perrais and H. Muhr, "Studies on the chemical behaviour of sodium fire aerosols during atmospheric dispersion", in Proceedings of the European Nuclear Conference, ENS, May 2014, Marseille.

[38] T. S. Kress, Proc. CSNI Specialists Meeting on Nuclear Aerosols in Reactor Safety, Gatlinburg, Tennesse, US, 1980.

[39] W. Cherdron, H. Bunz, and S. Jordan, "Properties of sodium fire aerosols and recalculation of their behaviour in closed containments", i*Proc. CSNI Specialists Meeting on Nuclear Aerosols in Reactor Safety, C Karlsruhe, Germany, pp. 395-405*, 1985.

[40] W. L. C. Hofmann, W. Jordan and S. Lindner "Chemical reactions of sodium fire aerosols in the free atmosphere," *J. Aerosol Sci.* 10, p. 191-192, 1979.

[41] L. E. Herranz, M. García, and M. P. Kissane, "In-containment source term in accident conditions in sodium-cooled fast reactors: Data needs and model capabilities", *Prog. Nucl. Energy 54, pp.138-149*, 2012.

[42] H. Sauter, "Investigations of methyl iodide decomposition in a sodium aerosol atmosphere", Science and Technology of Fast Reactor Safety, BNES, London, 1986.

References

[43] L. Lebel and N. Girault, "Learning from 1970 and 1980-Era Sodium Fire Experiments" Proc. FR17 conference, Yekateringburg, Russia,June 2017.

[44] W. Kohn, "Nobel Lecture: Electronic structure of matter—wave functions and density functionals," *Rev. Mod. Phys.*, vol. 71, no. 5, pp. 1253–1266, 1999.

[45] J. N. Harvey, "On the accuracy of density functional theory in transition metal chemistry," *Annu. Reports Sect. "C" (Physical Chem.*, vol. 102, p. 203, 2006.

[46] Capelle K., "A Bird's-Eye View of Density-Functional Theory," *Cond-Mat-Mtrl-Sci*, vol. 1–59. 2006.

[47] R. M. Martin, *Electronic Structure: Basic Theory and Practical Methods*. Cambridge University Press, 2004.

[48] W. Koch and M. C. Holthausen, *No Chemist's Guide to Density Functional Theory, 2nd ed*. Wiley-VCH Verlag GmbH, 2001.

[49] M Born and J R Oppenheimer, "On the quantum theory of molecules," 1927.

[50] R. P. Feynman, "Forces in molecules," *Phys. Rev.*, vol. 56, no. 4, pp. 340–343, 1939.

[51] R. K. D. G. N. K, *Computational chemistry and molecular modeling*. 2008.

[52] T. LH, "The calculation of atomic fields," 1927.

[53] P. H. and W. Kohn, "Inhomogeneous electron gas," vol. 155, no. 1962, 1964.

[54] W. Kohn and L. J. Sham, "Self-consistent equations including exchange and correlation effects," *Phys. Rev.*, vol. 140, no. 4A, 1965.

[55] J. P. Perdew, K. Burke, and Y. Wang, "Generalized gradient approximation for the exchange-correlation hole of a many-electron system," vol. 54, no. 23, pp. 533–539, 1996.

[56] J. P. Perdew, K. Burke, and M. Ernzerhof, "Generalized gradient approximation made simple," *Phys. Rev. Lett.*, vol. 77, no. 18, pp. 3865–3868, 1996.

[57] K. Burke, "Perspective on density functional theory," *J. Chem. Phys.*, vol. 136, no. December 2011, p. 150901, 2012.

[58] J. Klimeš and A. Michaelides, "Perspective: Advances and challenges in treating van der Waals dispersion forces in density functional theory," *J. Chem. Phys.*, vol. 137, no. 12, 2012.

[59] and T. R. W. Z. E. Hughes, L. B. Wright, *Biomolecular Adsorption at Aqueous Silver Interfaces: First-Principles Calculations, Polarizable Force-Field Simulations, and Comparisons with Gold*. 2013.

[60] H. Thirumalai and J. R. Kitchin, "The role of vdW interactions in coverage dependent adsorption energies of atomic adsorbates on Pt(111) and Pd(111)," *Surf. Sci.*, vol. 650, pp. 196–202, 2016.

[61] K. Johnston, "A van der Waals density functional study of the adsorption of ethanol on the ??-alumina (0001) surface," *Surf. Sci.*, vol. 621, pp. 16–22, 2014.

[62] S. Grimme, J. Antony, S. Ehrlich, H. Krieg, S. Grimme, J. Antony, S. Ehrlich, and H. Krieg, "A consistent and accurate ab initio parametrization of density

References

functional dispersion correction (DFT-D) for the 94 elements H-Pu A consistent and accurate ab initio parametrization of density functional dispersion correction „ DFT-D … for the 94 elements H-Pu," vol. 154104, no. 2010, 2011.

[63] J. Hafner, "*Ab-initio* simulations of materials using VASP: Density-functional theory and beyond," *J. Comput. Chem.*, vol. 29, no. 13, pp. 2044–2078, Oct. 2008.

[64] G. Kresse and J. Hafner, "Ab Initio Molecular Dynamics of Liquid Metals," *Physical Review B: Condensed Matter and Materials Physics*, vol. 47, no. 1. pp. 558–561, 1993.

[65] M. C. Payne, M. P. Teter, D. Allan, and Arias TA, "Iterative minimisation techniques for ab initio total-energy calculations: molecular dynamics and conjugate gradients," *Rev. Mod. Phys.*, 1992.

[66] D. Joubert, "From ultrasoft pseudopotentials to the projector augmented-wave method," *Phys. Rev. B - Condens. Matter Mater. Phys.*, vol. 59, no. 3, pp. 1758–1775, 1999.

[67] G. Kresse and D. Joubert, "From ultrasoft pseudopotentials to the projector augmented-wave method," *Phys. Rev. B*, vol. 59, no. 3, pp. 1758–1775, Jan. 1999.

[68] J. HAFNER, "Ab-Initio Simulations of Materials Using VASP: Density-Functional Theory and Beyond," *J. Comput. Chem.*, vol. 28, no. 1, pp. 73–86, 2009.

[69] G. Kresse, "Ab initio molecular dynamics for liquid metals," *J. Non. Cryst. Solids*, vol. 192–193, pp. 222–229, 1995.

[70] P. T. Czekala, C. Panosetti, H. Lin, and W. A. Hofer, "Van der Waals corrected DFT study of high coverage benzene adsorptions on Si(100) surface and STM simulations," *Surf. Sci.*, vol. 621, pp. 152–161, 2014.

[71] M. Methfessel and A. T. Paxton, "High-precision sampling for Brillouin-zone integration in metals," *Phys. Rev. B*, vol. 40, no. 6, pp. 3616–3621, 1989.

[72] I. Union, O. F. Pure, and A. Chemistry, "REPORTING PHYSISORPTION DATA FOR GAS/SOLID SYSTEMS with Special Reference to the Determination of Surface Area and Porosity," vol. 57, no. 4, pp. 603–619, 1985.

[73] W. Wang, W. Wang, P. Liu, M. Zhang, J. Hu, and F. Xing, "The Pore Structure of Phosphoaluminate Cement The Pore Structure of Phosphoaluminate Cement," no. November 2014, 2012.

[74] J. A. Arokiaswamy, "Source term estimation for radioactivity release under severe accident scenarios in sodium-cooled fast reactors," in *Fast reactor conference*, 2017.

[75] M. Manual, "Laskin Nozzle Generator."

[76] I. Olefjord and A. Nylund, "Surface analysis of oxidized aluminium. 2. Oxidation of aluminium in dry and humid atmosphere studied by ESCA, SEM, SAM and EDX," *Surf. Interface Anal.*, vol. 21, no. 5, pp. 290–297, 1994.

[77] A. . Fallis, *Scaning Electron Microscopy*, vol. 53, no. 9. 2013.

[78] K. Sing, "The use of nitrogen adsorption for the characterisation of porous materials," vol. 188, pp. 3–9, 2001.

[79] A. K. Ladavos, A. P. Katsoulidis, A. Iosifidis, K. S. Triantafyllidis, T. J. Pinnavaia, and P. J. Pomonis, "The BET equation, the inflection points of N2adsorption isotherms and the estimation of specific surface area of porous solids," *Microporous Mesoporous Mater.*, vol. 151, pp. 126–133, 2012.

[80] E. P. H. & T. E. Brunauer S, "Adsorption of gases in multimolecular layers," *J. biol. Chem*, no. 52, p. 1978, 1938.

[81] Agency for Toxic Substances and Disease Registry, "Toxicological Profile for Iodine," no. April, p. 253, 2004.

[82] R. J. Lemire, J. Paquette, D. F. Torgerson, D. J. Wren, and J. W. Flechter, "Assessment of iodine behaviour in reactor containment buildings from a chemical perspective," Pinawa, 1981.

[83] N. Li and L. Shi, "Experimental study of closed system in the chlorine dioxide-iodide-sulphuric acod reaction by UV-vis spectrophotometric method," *Int J Anal Chem*, 2011.

[84] O. Johansson, H. Mutelle, A. E. Parker, S. Batut, P. Demaux, C. Schoemaecker, and C. Fittschen, "Quantitative IBBCEAS measurements of I2 in the presence of aerosols," *Appl. Phys. B Lasers Opt.*, vol. 114, no. 3, pp. 421–432, 2014.

[85] S. Vaughan, T. Gherman, and A. Ruth, "Incoherent broad-band cavity-enhanced absorption spectroscopy of the marine boundary layer species I2, IO and OIO," *Phys. Chem. Chem. Phys.*, 2008.

[86] M. A. E. Parker and C. Fittschen, "Quantitative IBBCEAS measurements of I 2 in the presence of aerosols," pp. 421–432, 2014.

[87] J. Hrabina, O. Acef, F. Burck, N. Chiodo, Y. Candela, M. Sarbort, M. Hola, and J. Lazar, "Comparison of Molecular Iodine Spectral Properties at 514.7 and 532 nm Wavelengths," vol. 14, no. 4, pp. 213–218, 2014.

[88] R. W. Saunders, D. M. Joseph, S. H. Ashworth, and J. M. C. P. Absolute, "Absolute absorption cross-section and photolysis rate of To cite this version : HAL Id : hal-00295493 and Physics," 2004.

[89] G. C. Dubbledam and P. M. de Wolff, "The average crystal structure of γ-Na2CO3," *Acta Crystallogr. Sect. B Struct. Crystallogr. Cryst. Chem.*, vol. 25, no. 12, pp. 2665–2667, 1969.

[90] Y. Duan, B. Zhang, D. C. Sorescu, J. Karl Johnson, E. H. Majzoub, and D. R. Luebke, "Density functional theory studies on the electronic, structural, phonon dynamical and thermo-stability properties of bicarbonates MHCO $_3$, M = Li, Na, K," *J. Phys. Condens. Matter*, vol. 24, no. 32, p. 325501, 2012.

[91] H. Gao, S. Pishney, and M. J. Janik, "First principles study on the adsorption of CO2 and H2O on the K2CO3 (001) surface," *Surf. Sci.*, vol. 609, pp. 140–146, 2013.

References

[92] K. Reuter and M. Scheffler, "Composition, structure and stability of RuO_2(110) as a function of oxygen pressure," vol. 65, no. July, pp. 1–11, 2001.

[93] N. V. Zubkova, D. Y. Pushcharovsky, G. Ivaldi, G. Ferraris, I. V. Pekov, and N. V. Chukanov, "Crystal structure of natrite, gamma-Na2CO3," *Neues Jahrb. Miner. Mh.*, vol. 2003, no. May 2014, pp. 85–96, 2002.

[94] A. Arakcheeva, L. Bindi, P. Pattison, N. Meisser, G. Chapuis, and I. Pekov, "The incommensurately modulated structures of natural natrite at 120 and 293 K from synchrotron X-ray data," *Am. Mineral.*, vol. 95, no. 4, pp. 574–581, 2010.

[95] M. J. Harris and E. K. H. Salje, "The incommensurate phase of sodium carbonate: an infrared absorption study," *J. Phys. Condens. Matter*, vol. 4, no. 18, pp. 4399–4408, 1992.

[96] M. J. Harris, M. T. Dove, and K. W. Godfrey, "A single-crystal neutron scattering study of lattice melting in ferroelastic Na_{2} CO_{3}," vol. 8, pp. 7073–7084, 1996.

[97] Y. Duan, "A first-principles density functional theory study of the electronic structural and thermodynamic properties of M2ZrO3 and M2CO3 (M = Na, K) and their capabilities for CO2 capture," *J. Renew. Sustain. Energy*, vol. 4, no. 1, p. 013109, 2012.

[98] G. D. Barmparis, Z. Lodziana, N. Lopez, and I. N. Remediakis, "Nanoparticle shapes by using Wulff constructions and first-principles calculations," *Beilstein J. Nanotechnol.*, vol. 6, no. 1, pp. 361–368, 2015.

[99] I. Langmuir, "The adsorption of gases on plane surfaces of glass, mica and platinum," *J. Am. Chem. Soc.*, vol. 40, no. 9, pp. 1361–1403, 1918.

[100] D. Dollimore, P. Spooner, and A. Turner, "The BET method of analysis of gas adsoprtion and its relevance to the calculation of surface area," *Surf. Technol.*, vol. 4, pp. 121–160, 1976.

[101] J. D. P. PETER WILLIAM ATKINS, *Chimie physique*, vol. 4th. 2013.

[102] P. G. Robert J. Kee, Michael E. Coltrin, *Chemically Reacting Flow: Theory and Practice*. 2003.

[103] A. . S. Sillar, K.; Kundu, "Ab-initio prediction of adsorption isotherm for small molecules in MOF: the effect of lateral interactions for methane /CPO-27 Mg," *J. Phys. Chem. C*.

[104] A. . S. Sillar, K.; Kundu, "Prediction of Adsorption Isotherms for Gas Mixtures by Grand Canonical Monte Carlo on a lattice of sites."

[105] R. Dietzel, P. D. C.; Besikiotis, V.; Blom, "Application of Metal- Organic Frameworks With Coordinatively Unsaturated Metal Sites in Storage and Separation of Methane and Carbon Dioxide," *J. Mater. Res.*

[106] U. Buontempo, A. Di Cicco, A. Filipponi, M. Nardone, and P. Postorino, "Determination of the I2 bond-length distribution in liquid, solid and solution, by extended x-ray absorption fine structure spectroscopy," *J. Chem. Phys.*, vol. 107,

no. 15, pp. 5720–5726, 1997.

[107] L. E. Herranz, M. P. Kissane, and M. Garc??a, "Comparison of LWR and SFR in-containment source term: Similarities and differences," *Prog. Nucl. Energy*, vol. 66, pp. 52–60, 2013.